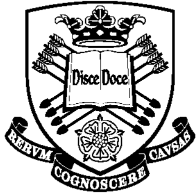

The University Of Sheffield.

Access to Electronic Thesis

Author:	Shiyu Xie
Thesis title:	Design and characterisation of InGaAs high speed photodiodes, InGaAs/InAlAs avalanche photodiodes and novel AlAsSb based avalanche photodiodes
Qualification:	PhD

This electronic thesis is protected by the Copyright, Designs and Patents Act 1988. No reproduction is permitted without consent of the author. It is also protected by the Creative Commons Licence allowing Attributions-Non-commercial-No derivatives.

If this electronic thesis has been edited by the author it will be indicated as such on the title page and in the text.

Design and characterisation of InGaAs high speed photodiodes, InGaAs/InAlAs avalanche photodiodes and novel AlAsSb based avalanche photodiodes

Shiyu Xie

The University Of Sheffield.

A thesis submitted for the degree of Doctor of Philosophy

Department of Electronic and Electrical Engineering
The University of Sheffield

March 2012

Acknowledgement

First, I would sincerely thank my supervisor, Dr. Chee Hing Tan, for giving me the opportunity to pursue a Ph.D in Sheffield and for providing me the patient and invaluable guidance during my postgraduate study. His assiduous and creative work attitude helps me to take on board a good research methodology and initial joy into my research. I am also indebted to Dr. Andrew Marshall, for spending a significant amount of time, guiding and discussing various aspects of high speed device design, fabrication and results analysis. I am also grateful to Prof. John David and Dr. Jo Shien for sharing their research experience and mentoring support during my stay in UK.

I have benefited much from Dr. Lionel Tan and Dr. Yu Ling Goh who offered me their expertise and valuable suggestions on material characterisations and understanding of physics of semiconductor devices. I appreciated help from Dr. Rob Airey at the University of Sheffield National III-V Center for his helpful advice in mask set design.

Thanks to all my co-workers in the impact ionisation group, Choo, Wai Mun, Daniel, Siew Lee, James, Syahrin, Peter, Jennifer, Rajiv, Rahman, Pin Jern, Jingjing, Matthew, Xinxin and Xiao, for their useful and enlightening conversations and friendship.

I would like to thank the University of Sheffield and Chinese Scholarship Council for sponsorship.

Finally, I am truly thankful to my family members and my friends in China for all their years of love and support that has spurred me towards the completion of this dissertation.

Abstract

Avalanche photodiodes (APDs) can provide higher sensitivity, when the noise is dominated by electronic noise, than conventional p-i-n photodiodes due to its internal gain achieved via the impact ionisation process. High speed and high sensitivity photodetectors operating at the wavelength of 1.55 μm for optical communication have been intensely research due to the ever increasing internet traffic, particularly in the long-haul communication systems. In this dissertation high speed InGaAs p-i-n photodiodes, InGaAs/InAlAs separate absorption and multiplication (SAM) APDs are designed and characterised. The waveguide InGaAs photodiode exhibits a maximum -3 dB bandwidth of 26.5 GHz and external quantum efficiency of 38.4% giving a bandwidth-efficiency product of 10.2 GHz, which is higher than 7.14 GHz obtained from conventional vertically illuminated diodes fabricated from the same wafer. Building on the high speed InGaAs waveguide diodes, the InGaAs/InAlAs APDs were fabricated. We demonstrated low dark currents of ~50 nA at $0.9V_{bd}$ (V_{bd} is the breakdown voltage), low excess noise factor $k \approx 0.2$ (k is the effective ratio of ionisation coefficients ratio in excess noise model) and wide bandwidth up to 40 GHz at low gains. Our APDs also achieve higher signal amplification than the best 40 Gb/s APD reported, confirming the suitability of our APDs for use in the 40 Gb/s optical communication systems. The signal enhancement of up to 24 dB was achieved at 35 GHz.

While the InGaAs/InAlAs APDs may be suitable for 40 Gb/s operation, the avalanche gain is limited due to their limited gain bandwidth products. Hence novel wide bandgap AlAsSb avalanche regions were characterised for next generation high speed SAM APDs. The temperature dependence of dark current and avalanche gain were investigated using AlAsSb p-i-n diodes with avalanche region widths of 80 and 230 nm. Extremely low temperature coefficients of breakdown voltage of 0.95 and 1.47 mV/K were obtained in these AlAsSb diodes, which are significantly lower than all semiconductor materials, with similar avalanche region widths, in the literature. Band to band tunelling current was shown to be significantly lower than those in InP and InAlAs diodes with the same avalanche region widths. By utilising an extremely thin 40 nm AlAsSb as multiplication layer, low excess noise factor corresponding to effective k values of 0.1 to 0.15 in InGaAs/AlAsSb SAM APDs was demonstrated. This is lower than that from an InAlAs pin diode with a 100 nm avalanche region. Therefore the potential of using thin AlAsSb avalanche region for next generation high speed and high sensitivity photodetectors has been demonstrated.

Publications

Journal papers

1. **S. Xie**, A. R. J. Marshall and C. H. Tan, ”Impedance matched 50 ohms InGaAs/InAlAs APDs”, in preparation for submission to IEEE J. Lightwave Tech..
2. **S. Xie** and C. H Tan, “AlAsSb avalanche photodiodes with a sub-mV/K temperature coefficient of breakdown voltage”, IEEE J. of Quantum Electron., vol. 47, no. 1, pp.1391-1395, 2011.
3. I. C. Sandall, **S. Xie**, J. Xie and C. H. Tan, “High temperature and wavelength dependence of avalanche gain of AlAsSb”, Optics Letters, vol. 36, Issue 21, pp. 4287-4289, 2011.
4. C. H. Tan, **S. Xie** and J. Xie, “Low noise avalanche photodiodes incorporating a 40nm AlAsSb avalanche region”, IEEE J. of Quantum Electron., vol. 48, no. 1, pp.36 – 41, 2012.
5. J. Xie, **S. Xie** , R. Tozer and C. H. Tan, “Excess Noise Characteristics of Thin AlAsSb APDs”, IEEE Trans. Electron Devices, Issue 99, pp. 3-5, March, 2012.

Conference papers

1. **S. Xie**, A. S. Idris, X. Zhou and C. H. Tan, “$AlAs_{0.56}Sb_{0.44}$ avalanche photodiode with an extremely small temperature coefficient of breakdown voltage”, *38th International Symposium on Compound Semiconductors (ICSC)*, 2011.
2. **S. Xie**, J. Xie, X. Zhou, P. J. Ker and C. H. Tan, “$AlAs_{0.56}Sb_{0.44}$ avalanche photodiode with weak temperature dependence”, *25th Meeting of the Semiconductor and Integrated Optoelectronics (SIOE)*, 2011.
3. **S. Xie**, A. R .J. Marshall, S. Ong, J. P. R. David, and C. H. Tan, “$In_{0.53}Ga_{0.47}As$/ $In_{0.52}Al_{0.48}As$ Avalanche Photodiodes with a Gain-Bandwidth Product of 160GHz”, *UK compound semiconductors conference*, July 2010.

4. C. H. Tan, **S. Xie** and J. Xie, "Thin AlAsSb avalanche regions with sub-mV/K temperature coefficients of breakdown voltage and very low excess noise factors", *IEEE Photonics conference(PHO)*, 2011.
5. I. C. Sandal, P. J. Kerr, **S. Xie**, J. Xie and C. H. Tan, "Avalanche gain characteristics in AlAsSb", *25th Meeting of the Semiconductor and Integrated Optoelectronics (SIOE)*, 2011.
6. X. Zhou, **S. Xie** and C. H. Tan, "APD designs for gain-bandwidth product above 200GHz", *UK compound semiconductors conference*, July 2011.
7. I. C. Sandal, P. J. Kerr, **S. Xie**, J. Xie, A. S. Idris and C.H. Tan, "Temperature dependent multiplication in AlAsSb", *UK semiconductors conference*, 2011.
8. C. H. Tan, L. J. J. Tan and **S. Xie**, "Extremely thin AlAsSb avalanche regions for a new generation of high speed avalanche photodiodes", *38th International Symposium on Compound Semiconductors (ICSC)*, Berlin, 2011.
9. A. R. J. Marshall, P. Vines, **S. Xie**, J. P. R. David and C. H. Tan, "High gain InAs electron avalanche photodiodes for optical communication ", *22nd International Conference on Indium Phosphide and Related Materials (IPRM),* 2010.
10. A.R.J. Marshall, A. Krysa, A.S. Idris, **S. Xie**, J.P.R. David and C.H. Tan, "High gain InAs avalanche photodiodes", *EMRS DTC 6th Annual Conf. Proc*., B9, July 2009.
11. C. H. Tan, J. S. Ng, **S. Xie** and J. P. R. David, "Potential materials for avalanche photodiodes operating above 10Gb/s*", International conference on computers and devices for communication (CODEC)*, 2009.

Glossary of Terms

a Lattice constant

A Device area

APD Avalanche photodiode

α Electron ionisation coefficient

  α^* Enabled electron ionisation coefficient

SAM APD Separate Absorption Multiplication Avalanche Photodiode

β Hole ionisation coefficient

  β^* Enabled hole ionisation coefficient

B Bandwidth

C Capacitance

  C_{si} Capacitance of Si photodiode

c Adjustable parameters for determination of the shape of the multiplication curve

C_{bd} Temperature coefficient of breakdown voltage

  ΔV_{bd} Breakdown voltage differences

  ΔT Temperature differences

CPW Coplanar waveguide

D Device diameter

DUT Device under test

d Depletion width

  $d_{e(h)}$ Dead space for electrons (holes)

E Carrier energy

  E_g Direct energy bandgap

  E_{the} Ionisation threshold energy for electrons

  E_{thh} Ionisation threshold energy for holes

  E_p Phonon energy

ε_0 Permittivity of free space

ε_r Relative permittivity

EAM Electro-absorption modulator

F Excess noise factor

F_e Electron initiated excess noise factor

F_h Hole initiated excess noise factor

$f_{transit}$ Transit time limited -3 dB bandwidth

G Gain of one single multiplication process

GBP Gain-bandwidth product

GSG Ground signal ground

h Planck's constant

$h(x)$ Probability density function of ionisation path length

$h_e(x)$ Probability density function of ionisation path length for electrons

$h_h(x)$ Probability density function of ionisation path length for holes

$\hbar\omega$ Phonon energy

I Current

I_0 Saturation current

I_{gr} Generation-recombination current

I_{tu} Tunelling current

I_{ph} Photocurrent

I_{pr} Primary photocurrent

k_B Boltzmann's constant

k Ratio of ionisation coefficients

L Waveguide length

L_i Inductance

LIA Lock-in Amplifier

M Avalanche gain

M_e Electron initiated avalanche gain

M_h Hole initiated avalanche gain

σ_M Standard deviation of the multiplication value

MBE Molecular Beam Epitaxy

MC Monte Carlo

μ Mobility of free space

m^* Effective electron mass

η ideality factor

η_{ext} External quantum efficiency

η_m Wave impedance in metal

δ_{sm} Skin depth

γ Optical absorption coefficient

τ Transit time

σ Conductivity

σ_T Constant that depends on the detailed shape of the tunelling barrier

λ Wavelength

ω Angular frequency

ζ Optical field envelope

ξ Electric Field

q Electron charge

ρ Resistivity

φ_m Metal work function

n Phonon occupation number

N Noise power

- N_{Amp} Amplifier noise
- N_m Measured noise power
- N_s Unity gain shot noise power

NFA Noise Figure Analyser

N' Doping concentration

P Optical signal power

pdf Probability density function

r Device radius

R Resistance

- R_S Series resistance
- R_L Load resistance

RPL Random path length model

RF Radio frequency

SEM Scanning electron microscopy

SIMS Secondary Ion Mass Spectroscopy

SMU Source Measurement Unit

SNR Signal-to-noise ratio

SPAD Single Photon Avalanche Diode

T Absolute temperature

TIA Trans-impedance amplifier

TEM Transverse electromagnetic

TXLINE Transmission line calculator

TWPD Travelling wave photodiode

TWAPD Travelling wave avalanche photodiode

V Voltage

V_t Applied reverse voltage

V_{bd} Breakdown voltage

VPD Vertically illuminated photodiodes

WG-PD Side illuminated waveguide photodiodes

WG-APD Side illuminated waveguide avalanche photodiodes

v_s Average of saturation electron and hole velocity

w Avalanche region width or thickness

Z_0 Characteristic impedance

List of tables and figures

Table 1.1 Excess noise factor comparison for different materials with different w.

Table 2.1 Hybrid-coplanar active diodes equations for the equivalent circuit model in figure 2.1.4. ρ is resistivity and $\sigma = 1/\rho$ is conductivity; ε and μ are permittivity and permeability. η_{ym0} is the metal-air transverse wave impedance, η_m is the wave impedance in metal, and δ_{sm} is the skin depth in metal. The coplanar waveguide inductance, L_{CPW} is calculated from numerical model. The dimensions and material characteristics are indicated in figure 2.1.4.

Table 4.1 Epitaxial layer structure of InGaAs p-i-n photodiodes.

Table 4.2 Calculated capacitances, series resistances, -3 dB RC-limited bandwidth and measured -3 dB bandwidth for VPDs and WG-PDs.

Table 5.1 Structural details of the SAM APD (M3698) showing nominal values compared to those deduced from C-V fitting.

Table 5.2 Structural details of the SAM APD (M3587)

Table 5.3 Enhanced response with reverse bias voltage at selected frequencies

Table 5.4 Calculated capacitance, series resistance, RC limited bandwidth for M3698 with different waveguide lengths

Table 5.5 Calculated capacitance, series resistance, RC limited bandwidth for M3587 with different waveguide lengths

Table 6.1 Epitaxial layer structure of AlAsSb based p-i-n APDs.

Table 6.2 A comparison of C_{bd} in diodes with $w < 300$ nm

Table 7.1 Structural details of the SAM-APD

Table 7.2 Current density comparison between our diode and Ge based diodes.

Figure 1.1.1 (a) structure of lumped (top-illuminated p-i-n photodiodes) and (b) equivalent circuit model.

Figure 1.1.2 -3 dB transit time limited and RC time limited bandwidth for InGaAs VPDs.

Figure 1.1.3 (a) structure of TWPD and (b) equivalent circuit model.

Figure 1.2.1 Schematic of (a) an electron and (b) an hole initiated impact ionisation event.

Figure 1.2.2 Schematic of multiplication process initiated by an electron injected at the edge of the avalanche region.

Figure 1.2.3 Excess noise factor prediction using McIntyre's local analysis for k=0, 0.2, 0.4, 0.6, 0.8, 1, 5 and 10 for electron injection and 1/k for hole injection.
Figure 1.2.4 Electron pdf of ionisation path lengths in local (black line) and non-local hard dead space model (blue line).
Figure 1.2.5 Frequency response predictions for various ratios of β/α.
Figure 1.2.6 Schematic diagram and electric field profile in a typical SAM APD.
Figure 1.2.7 Gain-bandwidth products reported for InP, InAlAs and Ge/Si APDs.
Figure 1.3.1 Typical temperature dependence of multiplication in wide bandgap materials.
Figure 1.3.2 Excess noise measured at the M ~ 8 with $Al_{0.8}Ga_{0.2}As$, $Al_{0.6}Ga_{0.4}As$, $Al_{0.3}Ga_{0.7}As$, $Al_{0.15}Ga_{0.85}As$, GaAs, GaInP and InAlAs for pure electron injection and InP for pure hole injection.
Figure 2.1.1 Schematic planar microwave transmission line.
Figure 2.1.2 (a) Schematic of CPW (b) typical calculated gap width versus signal pad width for different characteristic impedances for CPWs on InP substrate at the frequency of 40 GHz, assuming substrate thickness = 100 μm and Au metallisation thickness = 0.5 μm.
Figure 2.1.3 (a) Top view (b) cross section of hybrid CPW structure.
Figure 2.1.4 (a) Hybrid-coplanar active diode structure dimensions and material parameters; (b) equivalent circuit of semiconductor cladding layer; (c) the corresponding equivalent circuit of the transmission line.
Figure 2.1.5 General transmission equivalent circuit model
Figure 2.2.1 Schematic photomultiplication setup by phase-sensitive technique.
Figure 2.2.2 Schematic calibration process using noise source.
Figure 2.2.3 Schematic diagram of noise measurement system using NFA.
Figure 2.2.4 Schematic diagram of excess noise circuit set up.
Figure 2.2.5 Schematic diagram of optical heterodyne setup.
Figure 2.2.6 (a) an example of the frequency response of a diode at the beat frequency of 4.2 GHz and (b) full frequency response of InGaAs/InAlAs vertically illuminated APDs with different diameters measured by heterodyne setup.
Figure 2.2.7 Schematic diagram of externally modulated laser setup.

Figure 2.2.8 Total system loss from all the RF components.

Figure 2.2.9 Probe station for the microwave measurement.

Figure 2.2.10 Side illumination measurements for the waveguide devices under test.

Figure 3.1.1 Schematic of MBE chamber

Figure 3.2.1 Microscope view of sample surface after different recipes: (a) 1:1:1:10 HBr: CH_3COOH: $K_2Cr_2O_3$: DIW; (b) 1:8:80 H_2SO_4: H_2O_2: DIW; (c) 1:8:80 H_2SO_4: H_2O_2: DIW + 1: 1: 9 – HCL: H_2O_2: DIW and (d) 1:8:80 H_2SO_4: H_2O_2: DIW +1:1:5 - HCL: H_2O_2: DIW.

Figure 3.2.2 I-V characteristics for unpassivated and passivated InGaAs/AlAsSb SAM APDs with different dielectric films.

Figure 3.2.3 (a) Top and (b) cross-section view of fabricated simple mesa diode.

Figure 3.3.1 SEM of (a) square pixel and (b) etch profiles of 4 x 4 square pixels on InGaAs/InAlAs APD. The pixel edges were oriented in parallel to the $[011]$ and to the $[01\bar{1}]$ directions of the grown wafer.

Figure 3.3.2 SEM of InGaAs/InAlAs APD etch profiles in directions of (a) $[011]$ and (b) $[01\bar{1}]$ directions of the grown wafer with the etch depth of 1.7 μm. An undercut was observed in (a).

Figure 3.3.3 SEM of the metal track transition from the top p^+ of the mesa to the n^+ bottom layer in directions of (a) $[011]$ and (b) $[01\bar{1}]$ of the grown InGaAs/InAlAs wafer.

Figure 3.3.4 (a) Schematic illustration the surface leakage current flowing through the bond pads; (b) measured surface leakage current with different etching depth for different acid and etching time.

Figure 3.3.5 SEM of the bond pad links the bottom n^+ InGaAs contact layer to the InP semi-insulating substrate.

Figure 3.3.6 Scribe and cleave along the center of the ridge device, the dashed line is facet cleaving.

Figure 3.3.7 SEM of top view of (a) top illuminated and (b) side illuminated devices.

Fig 4.2.1 Measured and modeled capacitance for InGaAs p-i-n diode with a diameter of 100 μm.

Figure 4.2.2 Dark current measurements for all the devices. The mesa diode with 100 μm diameter was shown for comparison.

Fig 4.2.3 Relative frequency response measurement by using heterodyne for different type of diodes: (a) VPDs with different diameters (b) WG-PDs with different waveguide lengths.

Figure 5.2.1 Simulated absolute characteristic impedance for InGaAs/InAlAs SAM APD: (a) M3698 and (b) M3587 using a hybrid coplanar transmission line model.

Figure 5.2.2 Schematic of waveguide bond pads in the diodes.

Figure 5.3.1: Comparisons between measured, fitted and targeted C-V for a diode with diameter of 50 μm for (a) M3698 and (b) M3587.

Figure 5.3.2 Dark current measurements for the devices (a) M3698 and (b) M3587 with waveguide lengths of 15, 30 and 55 μm. The leakage current originating from the bond pad, BP, with length of 125 μm, deposited on the semi-insulating substrate was measured (○) for comparison.

Figure 5.3.3 Measured avalanche gain and excess noise factor for M3698: (a) and (b) and for M3587: (c) and (d). The lines corresponding to k = 0 to 0.20 (with an increment of 0.1), in the local noise theory [8]. Excess noise measured on InAlAs p-i-n diodes with avalanche regions of 200 and 100 nm are included for comparison.

Figure 5.3.4 Photocurrent measurement at the wavelength of 1.3 μm for (a) M3698 and (b) M3587.

Figure 5.3.5 Frequency response measurements on (a) M3698 and (b) M3587 under different reverse bias voltages.

Figure 5.3.6 Relative frequency responses of the devices with different waveguide lengths for (a) M3698 at 18 V and (b) M3587 at 17 ~ 17.5 V. Commercial 50 GHz XPDV diode is included for bandwidth comparison.

Figure 5.3.7 Power sweep at fixed frequency in (a) M3698 and (b) M3587. Commercial 50 GHz XPDV diode is included for linearity comparison.

Figure 5.4.1 Dark current comparisons for M3698 with the diode area of 5×55 μm^2, M3587 with the diode area of 4×55 μm^{2}and the 40 Gb/s InGaAs/InAlAs waveguide by Makita et al. [10] with the diode area of 6×20 μm^2.

Figure 6.2.1 Measured (symbols) and fitted (lines) C-V characteristics and deduced electric field profile for AlAsSb diodes with D = 400 µm and w = 80 nm (a) and 230 nm (b).

Figure 6.2.2 Measured I-V characteristics for AlAsSb diodes with D = 200 µm and w = 80 nm (solid lines) and 230 nm (dash lines) at temperatures, T of 77, 140, 200, 250 and 295 K.

Figure 6.2.4 Extrapolation of 1/M to 0 for the diodes with (a) w = 80 nm and (b) w = 230 nm at temperatures of 77, 140, 200, 250 and 295 K.

Figure 6.3.1 Calculated tunelling current density for InP and InAlAs diode with w = 80 nm at 290 and 14 K and comparing with the current density in PIN1 at 77 K.

Figure 6.3.2 Comparison of C_{bd} for AlAsSb (●), Si (○) [15], GaAs (▽) [16], $Al_{0.6}Ga_{0.4}As$ (□) [17], GaInP (×) [18] InP (◇) [19] and InAlAs (△) [20] diodes with submicron avalanche regions.

Figure 7.2.1 (a) Measured capacitance for diodes with diameter of 50, 100, 200 and 400 µm. (b) Comparisons between measured, modeled and intended C-V.

Figure 7.2.2 (a) Dark current density obtained from diodes with diameter of 50 to 400µm and (b) Comparison between dark current, photocurrent and calculated tunelling current from the InGaAs absorption layer.

Figure 7.2.3 Measured avalanche gain (left) and excess noise factor (right). The lines corresponding to k = 0 to 0.20 (with an increment of 0.05), in the local noise theory [8] and excess noise measured on an InAlAs pin diode with an avalanche region of 100 nm [10] are included for comparison.

Figure 7.3.1 Deduced and intended electric field profiles at punch-through voltages (left) and at a higher bias of 22.0 V (right).

Figure 7.3.2 SIMS results of the InGaAs/AlAsSb SAM APD.

Figure A.1 Schematic of a CPW without bottom ground metal.

Figure B.1 Electric filed profile in the $p^+p^-n^+$ diode

Figure C.1 Calibration process using the VNA and EAM.

Figure C.2 Frequency response measurement using VNA and EAM

Figure C. 3 Frequency response measurement using heterodyne setup

Table of contents

Acknowledgement ii

Abstract iii

Publications iv

Glossary of Terms vi

List of tables and figures x

Chapter 1 Introduction 1

1.1 High speed photodiodes 1

1.1.1 Review of high speed InGaAs photodiode 3

1.2 High speed avalanche photodiodes 5

1.2.1 Impact ionisation theory 5

1.2.2 Avalanche photodiodes 11

1.2.3 Review of high speed APDs 13

1.3 Temperature dependence of breakdown and wide bandgap based APDs 15

1.4 Organisation of thesis 19

1.5 Reference 19

Chapter 2 Theory and Design of travelling wave photodetectors and characterisation techniques 25

2.1 Theory of travelling wave diode 25

2.1.1 Transmission line 25

2.1.2 Equivalent circuit model 28

2.2 Experimental characterisation techniques 32

2.2.1 Current-voltage (*I-V*) measurement 32

2.2.2 Capacitance-voltage (*C-V*) measurement 33

2.2.3 Photomultiplication measurement 34

2.2.4 Excess noise measurement 37

2.2.5 Frequency response measurement 41

2.3 Reference 46

Chapter 3 Fabrication techniques ____ 49
3. 1 Molecular beam epitaxy (MBE) ____ **49**
3.2 Simple mesa diode ____ **50**
3.3 High speed InGaAs/InAlAs APDs ____ **54**
3.4 Reference ____ **62**

Chapter 4 High speed InGaAs p-i-n photodiode operating at 1.55 µm ____ 63
4.1 Device structure ____ **63**
4.2 Experimental details ____ **64**
4.2.1 *C-V* measurement ____ **64**
4.2.2 Dark *I-V* measurement ____ **64**
4.2.3 Responsivity measurement ____ **65**
4.2.4 Frequency response measurement ____ **65**
4.3 Discussions ____ **66**
4.4 Conclusions ____ **69**

Chapter 5 High speed InGaAs/InAlAs SAM APD ____ 70
5.1 Device structure ____ **70**
5.2 Theoretical characteristic impedance ____ **71**
5.3 Experimental details ____ **73**
5.3.1 *C-V* measurement ____ **73**
5.3.2 Dark *I-V* measurement ____ **74**
5.3.3 Excess noise measurement ____ **75**
5.3.4 Frequency response measurement ____ **76**
5.3.5 Power dependence measurement ____ **79**
5.4 Discussions ____ **81**
5.5 Conclusion ____ **86**
5.6 Reference ____ **86**

Chapter 6 Temperature dependence in AlAsSb ____ 88
6.1 Device structure ____ **88**
6.2 Experimental details ____ **89**

6.2.1 *C-V* measurement __ **89**
6.2.2 Temperature dependence of dark current __ **90**
6.2.3 Temperature dependence of avalanche gain __ **91**
6.3 Discussions __ **93**
6.4 Conclusion __ **97**
6.5 Reference __ **97**

Chapter 7 Low excess noise InGaAs/AlAsSb SAM APDs __ 100
7.1 Device structure __ **100**
7.2 Experimental details __ **100**
7.2.1 *C-V* measurement __ **100**
7.2.2 Dark *I-V* measurement __ **102**
7.2.3 Excess noise measurement __ **103**
7.3 Discussions __ **104**
7.4 Conclusion __ **108**
7.5 Reference __ **109**

Chapter 8 Conclusion __ 111
8.1 Conclusion __ **111**
8.2 Suggestions for future work __ **112**
8.3 Reference __ **114**

Appendix A Analytical calculations of circuit elements in CPW __ **115**
Appendix B Calculation of electric field profile __ **117**
Appendix C Operation instructions for high speed measurement setup __ **120**
Appendix D Fabrication Process __ **124**

Chapter 1 Introduction

Photodiodes, which convert the optical signal into the electrical signal, can be used for various optical applications; the optical communication being one of the most important examples that have influence our daily life [1]. Since the internet was launched for public use in 1993 [2], the internet data transmission has expanded into a great volume, and hence high data transmission medium and optical receiver are required. Standard single-mode fiber offers more than 25 THz bandwidth [2] and its low cost leads to its use as the most natural transmission medium [3], [4]. High speed optical receiver is also a critical component in the optical transmission systems. The speed and sensitivity are the two key performance parameters for the telecommunication photodetector design [5].

1.1 High speed photodiodes

In the long-haul telecommunication systems, the fiber has two "low-loss" windows at the wavelengths of 1.31 and 1.55 μm respectively, so that photodiodes used for optical communications are always designed for these two wavelengths. Among the naturally occurring semiconductor materials, only Germanium (Ge) with a bandgap energy of 0.6 eV can readily provide detections up to ~ 1.7 μm [5]. However it is an indirect bandgap material and its narrow bandgap leads to high dark current level that limits its optoelectronic application. Fortunately, some compound semiconductor materials could provide high sensitivity at long wavelengths. $In_{0.53}Ga_{0.47}As$ (here after referred to as InGaAs) is a direct bandgap material with a bandgap energy of 0.75 eV can provide detection up to a wavelength 1.7 μm. InGaAs p-i-n photodiodes are currently the most common photodetector for telecommunication applications. However in the conventional vertically illuminated p-i-n diodes (VPD), there is an inherent trade-off between the quantum efficiency and bandwidth.

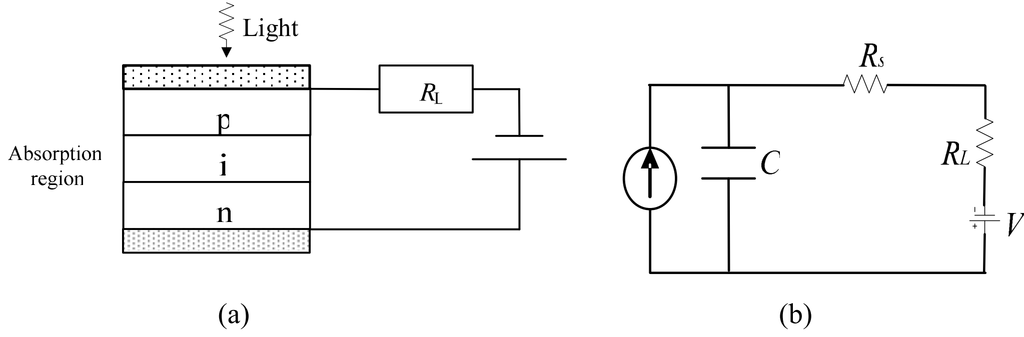

Figure 1.1.1 (a) structure of lumped (top-illuminated p-i-n photodiodes) and (b) equivalent circuit model.

Figure 1.1.1 shows a schematic device structure and the corresponding equivalent circuit of a lumped VPD. The optical power is perpendicular to the detector in the lumped VPD. The transit time limited -3 dB bandwidth can be expressed as [6]

$$f_{transit} \approx 0.5 \times \frac{v_s}{d} \tag{1.1.1}$$

where v_s is the average of saturation electron and hole velocity. The shorter depletion width, d, can provide a smaller transit time and hence higher $f_{transit}$.

However the external quantum efficiency η_{ext} of the VPD structure is given by [6]

$$\eta_{ext} \propto (1 - \exp(-\gamma d)) \tag{1.1.2}$$

where γ is optical absorption coefficient. Therefore thicker absorption region (i-region) width is required for high quantum efficiency, but this increases the carrier transit time resulting in lower bandwidth.

In addition, the corresponding RC-limited bandwidth is given by

$$C = \frac{\varepsilon A}{d} \tag{1.1.3}$$

$$R = R_s + R_L \tag{1.1.4}$$

$$f_{RC} = \frac{1}{2\pi RC} = \frac{d}{2\pi R \varepsilon A} \propto \frac{d}{(R_s + R_L)A} \tag{1.1.5}$$

where ε is the dielectric constant of intrinsic region and C is the intrinsic capacitance of the p-i-n structure. R_s is the series resistance including the semiconductor and the metal resistivity. R_L is the load resistance matching with the external circuit, which generally equals to 50 Ω. R is the sum of external load resistance and the series resistance.

There is also a trade-off between the transit time and RC- limited bandwidth in the VPD, as illustrated the transit time limited and RC limited -3 dB bandwidth for InGaAs VPDs in figure 1.1.2, assuming R = 60 Ω and R_s = 10 Ω , device radius (r) ranging from 10 to 80 μm and depletion width ranging from 0.1 to 3.5 μm.

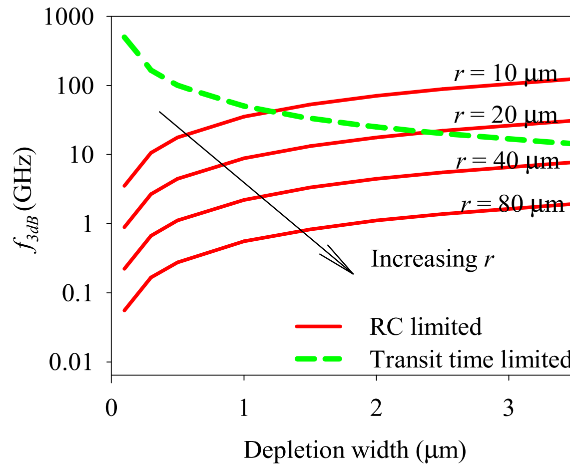

Figure 1.1.2 -3 dB transit time and RC time limited bandwidth for InGaAs VPDs with radius (r).

1.1.1 Review of high speed InGaAs photodiode

Increasing the bandwidth-quantum efficiency product is crucial for InGaAs photodiodes. Great efforts have been made in the past to increase speed and quantum efficiency for the InGaAs photodiodes. I. Kimikin *et al.* [7] reported InGaAs photodiode utilizing a resonant cavity enhanced structure showing a bandwidth of 31 GHz and a peak quantum efficiency above 50% between the wavelengths of 1550 and 1620 nm, corresponding to a bandwidth efficiency product of 20 GHz. Ishibashi *et al.* [8-10] reported InP/InGaAs uni-travelling carrier photodiodes, in which the absorption and collection layer are designed separately so that only electron is injected into the collection layer. The diode is biased such that the electrons travel with the maximum overshoot velocity to obtain a faster response achieving bandwidths of 78-152 GHz under different bias conditions and a

quantum efficiency of 22%. K. Kato *et al.* [11] employed a multimode mushroom mesa structure designed to maximise the coupling efficiency by matching the optical field of the fibre and the photodiode. They obtained a bandwidth of 110 GHz and an external quantum efficiency of 55%. A. Beling *et al.* [12] utilised an optical matching layer integrated into InGaAs p-i-n photodiodes. By controlling the optical intensity distribution by matching the refractive indices of the waveguide and absorber, and also employing a low resistance contact layer, they maintained high quantum efficiency of 40.8% and achieved a bandwidth of 120 GHz. Giboney *et al.* [13, 14] first proposed and demonstrated a travelling wave photodiode (TWPD) with GaAs p-i-n structure to improve both the bandwidth and quantum efficiency of the photodiodes. This TWPD is an optimised waveguide photodetector which distributes the RC elements on the transmission line and matching the characteristic impedance to the external circuit. Therefore the reflected wave feeding back to the output load circuit that slows down the output signal can be minimised, thus eliminating the RC-lump effect [15]. The GaAs p-i-n TWPD was reported with a bandwidth of 174 GHz and a 76 GHz bandwidth efficiency product, significantly overcoming the limitation of 40 GHz for GaAs photodiode [15]. Figure 1.1.3 shows a schematic device structure and the corresponding equivalent circuit of distributed TWPD. Follow on this, Chiu *et al.* reported a low temperature grown GaAs p-i-n TWPD with a bandwidth of 370 GHz [16] and quantum efficiency of 8% and a metal-semiconductor-metal GaAs TWPDs [16-18] with bandwidth of 570 GHz and the quantum efficiency of 5% for operating at the wavelength of 800 nm. Stohr *et al.* [19] demonstrated a travelling wave multiple-quantum-well (MQW) InGaAs photodetector for 1.55 µm network application with the bandwidth of 110 GHz and quantum efficiency of 6.4%.

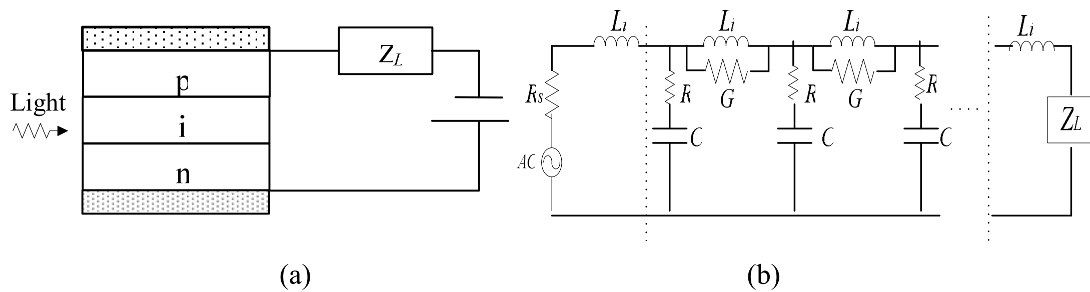

(a) (b)

Figure 1.1.3 (a) structure of TWPD and (b) equivalent circuit model.

1.2 High speed avalanche photodiodes

Avalanche photodiodes (APDs) are another type of photodetectors widely used in telecommunication systems. By utilising the impact ionisation process to provide an internal gain, APDs have the advantage of the higher sensitivity over conventional p-i-n photodiodes when the overall noise in the receiver module is dominated by the electronic noise.

1.2.1 Impact ionisation theory

Impact ionisation is a process that a carrier (electron or hole) has gained sufficient energy from the electric field to promote an electron from the valance band into the conduction band, leaving behind a hole in the valence band. This creates both a free electron in the conduction band and a free hole in the valence band. Both primary and the secondary electron-hole pair can subsequently gain energy from the electric field and undergo further impact ionisation events. The impact ionisation event is conceptually depicted in figure 1.2.1 for both electron and hole initiated process in a direct band gap semiconductor. In many semiconductors the energetic carriers occupy higher energy bands.

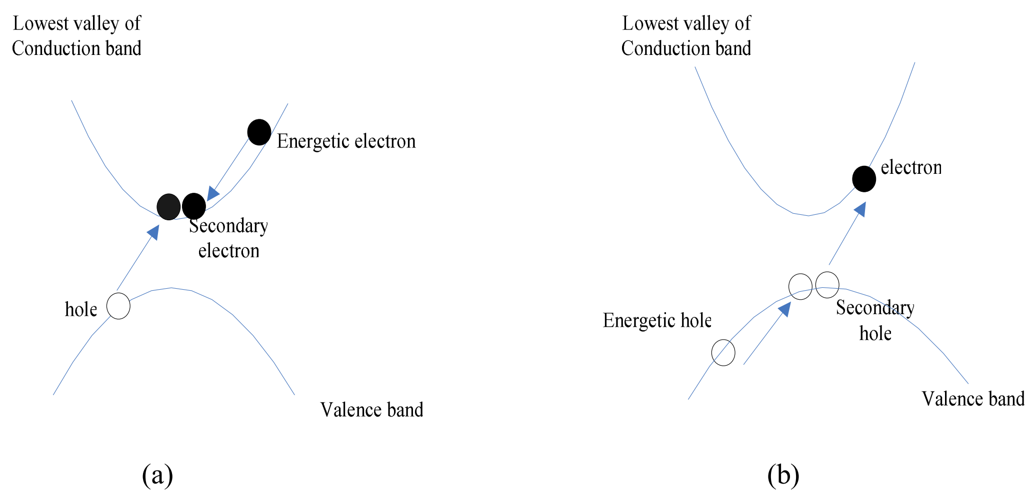

Figure 1.2.1 Schematic of (a) an electron and (b) an hole initiated impact ionisation event.

During the carrier acceleration process under the electric field, in addition to the impact ionisation process, the free carrier also encounters non-ionisation collision with phonons [20]. Phonon scattering may involve carriers gaining energy (phonon absorption), losing

energy (phonon emission) and exchanging momentum (elastic). Phonon emission process is proportional to n+1 and phonon absorption is proportional to n, and carriers on average will lose energy during the phonon scattering process, which impedes the impact ionisation occurs [21]. n is the phonon occupation number that depends on the phonon energy, $\hbar\omega$, and it can be expressed as

$$n = \frac{1}{\exp(\frac{\hbar\omega}{k_B T}) - 1}, \qquad (1.2.1)$$

where k_B is the Boltzmann's constant and T is the absolute temperature.

The impact ionisation characteristics of electrons and holes in a semiconductor are generally characterised by the impact ionisation coefficients, α and β respectively. These electric field dependent coefficients describe the average number of electron-hole pairs created per unit distance travelled by an electron or hole in a uniform electronic field and thus can be defined as the inverse of the mean distance between successive ionisation events.

Avalanche multiplication is the result of impact ionisation process that produces an internal current gain, as illustrated in Fig 1.2.2. A single carrier (electron) was injected at the edge of avalanche region under high electric field and a chain of impact ionisation events is triggered. At the end of avalanche process, five electrons are collected resulting in an avalanche gain of five.

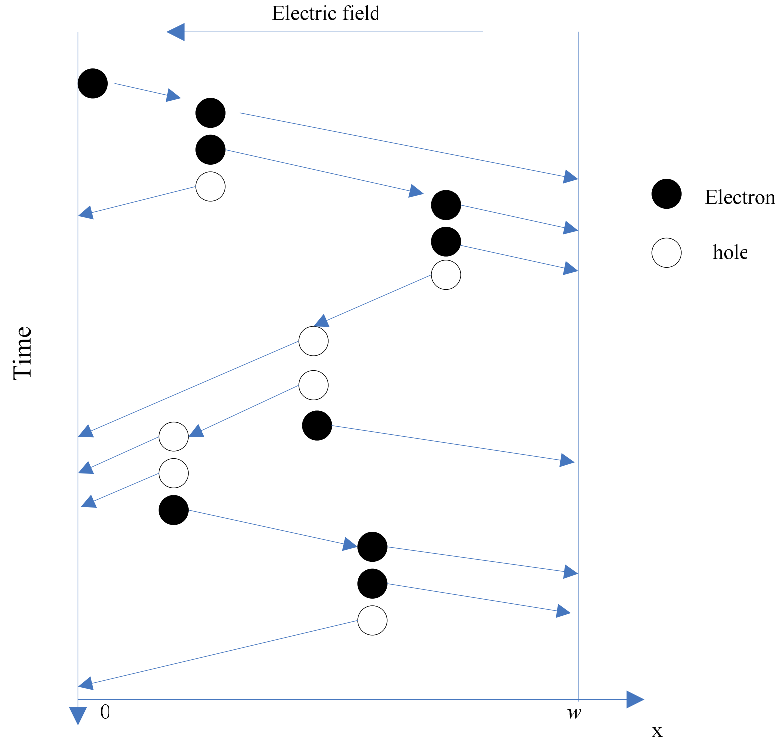

Figure 1.2.2 Schematic of multiplication process initiated by an electron injected at the edge of the avalanche region.

Assuming that a carrier's ionisation probability at a given position depends only on the local electric field and the electric field is uniform in the avalanche region, the mean avalanche gain arising from an electron-hole pair injected at a position x is given by [22]

$$M(x) = \frac{(\beta-\alpha)\exp([\beta-\alpha]x)}{\beta-\alpha\exp([\beta-\alpha]w)} \tag{1.2.2}$$

where w is the avalanche region width.

Therefore pure electron injection gain, M_e, and pure hole injection gain, M_h can be obtained by setting x=0 and x=w, and respectively as

$$M_e = \frac{1}{1-\frac{\alpha}{\beta-\alpha}(\exp((\beta-\alpha)w)-1)} \tag{1.2.3}$$

$$M_h = \frac{1}{1 - \frac{\beta}{\alpha - \beta}(\exp((\alpha - \beta)w) - 1)} \quad (1.2.4)$$

When the gain becomes infinite, avalanche breakdown occurs. The breakdown voltage is the voltage that produces α and β such that the denominator of equation (1.2.3) and (1.2.4) equals to zero when

$$\exp([\beta - \alpha]w) = \frac{\beta}{\alpha} \quad (1.2.5)$$

Therefore the breakdown voltage is not influenced by the carrier injection conditions [20]. In general the above model used for impact ionisation is called local model. Local model is usually valid for the diodes with long avalanche region width, in which carriers are in equilibrium with the electric field and the dead space, the distance a carrier has to travel to acquire sufficient energy to create an impact ionisation event, is negligible compared to the mean ionisation path length [20].

The stochastic nature of the impact ionisation process leads to a notable spread of the total number of carriers generated by an injected electron-hole pair under a specific electric field, giving rise to excess noise which is characterised by the excess noise factor, F. By assuming a standard deviation of the multiplication value, σ_M, and for gain in a single multiplication process, G, F is given by

$$F = 1 + \frac{\sigma_M^2}{< G >^2} \quad (1.2.6)$$

where $\sigma_M^2 = < G^2 > - < G >^2$. Therefore F can be equivalently expressed as

$$F = \frac{< G^2 >}{< G >^2} \quad (1.2.7)$$

McIntyre [23] introduced an elegant local model to calculate the excess noise factor versus multiplication for uniform electric field. For pure electron injection, the excess noise factor can be written as

$$F = kM + (2 - \frac{1}{M})(1 - k) \quad (1.2.8)$$

where k is the ratio of electron and hole ionisation coefficient, $k = \beta/\alpha$. For hole injection alone, the foregoing expression still valid if k is replaced by $k' = \alpha/\beta$ and $M = \langle G \rangle$.

Figure 1.2.3 shows a plot of *F(M)* as a function of *k* where *F(M)* increases with *k*. Therefore to achieve low excess noise, a material with dissimilar ionisation coefficients ratio and the more strongly ionising carrier should be injected into the avalanche region.

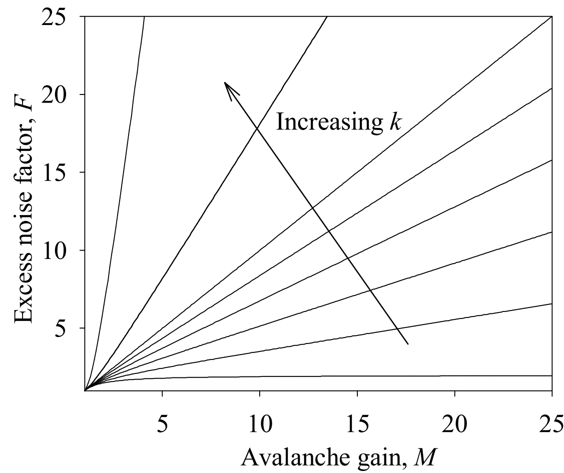

Figure 1.2.3 Excess noise factor prediction using McIntyre's local analysis for k=0, 0.2, 0.4, 0.6, 0.8, 1, 5 and 10 for electron injection and $1/k$ for hole injection.

However in devices with sub-micron avalanche widths, the dead space that the distance a carrier has to travel for its ionization to reach equilibrium with electric field becomes a significant fraction of the avalanche width and the carriers' ionisation probabilities at a given position are dependent on the local electric field and the history of the carriers. Since the local ionisation model neglects the dead space effect, it increasingly overestimates M and underestimates the breakdown voltage as the avalanche region width reduces to sub-micron. It is well known that the excess noise factor will fall below that expected from equations 1.2.8 when device avalanche region width reduced below 0.8 μm [20], which is due to the carriers' ionisation probabilities narrowing and thus reduce the spread in gain distribution and the length of multiplication chains. A non-local model is required to take into account dead space effect. The ballistic dead space for electrons, d_e, and holes, d_h, can be estimated by using:

$$d_{e(h)} = \frac{E_{the(thh)}}{q\xi} \ , \qquad (1.2.9)$$

where q is the electron charge and ξ is the electric field. $E_{the(thh)}$ is the threshold energy for electrons (holes). In general E_{th} must exceed the band gap of the material. The carriers can gradually heat up while drifting across the high electric field region and cools down via phonon emissions. Therefore a finite travelled distance is required before achieving E_{th}.

In general Monte Carlo (MC) models can provide the most realistic description but it requires a long computation time and comprehensive material parameters, which are not attractive for device simulation and experimental analysis. Hayat *et al.* [24] developed a recurrence technique which requires the carriers' ionisation probability distribution functions (pdfs) as input to formulate a closed form expression of integral equations to predict M and F. Ong *et al.* [25] developed a random path length (RPL) model which is based on the Monte Carlo method. As before, the carriers' ionisation pdfs are required as the model input. The multiplication chains for many trials are recorded and the average gain over these trials will be calculated to give the mean avalanche gain. In the non-local model, local ionisation coefficient will be replaced by the enabled ionisation coefficients, α^* for electrons and β^* for holes. The enable ionisation coefficients are different from the local ionisation coefficients in the local model, which describe the carriers have already travelled the dead space. Figure 1.2.4 illustrates the electrons ionisation path length probability density function (pdf) in the local model and a hard dead space non local model. The electron ionisation path length is expressed as its pdf, $h_e(x)$

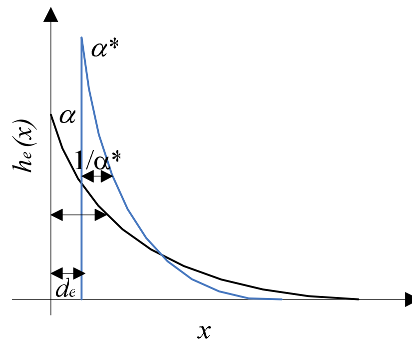

Figure 1.2.4 Electron pdf of ionisation path lengths in local (black line) and non-local hard dead space model (blue line).

1.2.2 Avalanche photodiodes

Although APDs have the advantage of the higher sensitivity over conventional p-i-n photodiodes due to the impact ionisation process, the inherent stochastic nature of the impact ionisation process will result in excess noise in the APDs [20]. Together with the "shot noise" in the APDs, which arises from the random fluctuations in the motion of carriers and includes the shot noise from the surface leakage current (unmultiplied), bulk dark current and photocurrent, the signal to noise ratio (*SNR*) in APDs can be written as [26]

$$SNR = \frac{P}{FN_s + (N_{amp} / M^2)} \tag{1.2.10}$$

where P is the received optical signal power, N_s is the unity gain short noise power and N_{amp} is the amplifier noise power. In general at high frequency the trans-impedance amplifier (TIA) used in telecommunication applications has $N_{amp}>>N_s$ such that operating APDs with high gains will produce a significant improvement in the *SNR* as the term of N_{amp}/M^2 decreases if F increases slowly with M.

Together with the *SNR*, the frequency response of APDs needs to be considered as well. The transit time limited bandwidth, given by equation (1.1.1), is no longer valid for APD since the avalanche gain is built up over several transit times. Consequently the gain decreases at high frequency leading to a gain trade-off and the frequency dependence of gain can be expressed as [27]

$$M(\omega) = M_0[1 + (\omega\tau M_0)^2]^{-1/2} \ , \tag{1.2.11}$$

where $M_0 = M$ is the low-frequency gain and τ is an "effective" transit time through the avalanche region which depends on the ratio of the hole and electron ionisation coefficients. Therefore there is a trade off between the APD gain M and the bandwidth, leading to a gain-bandwidth product (GBP), which it is now a well accepted figure of merit to evaluate the APD response speed [5, 28, 29].

The dependence of APD bandwidth on the ionisation coefficient ratio has been investigated using a local model [27], as shown in figure 1.2.5. Semiconductors which have a more disparate ionisation coefficient ratio will be preferable to have a higher GBP. Besides ionisation coefficient ratio, the influence of dead space effect in APD's bandwidth also has been studied by using the RPL model [30]. At a fixed gain the bandwidth is reduced as the dead space effect becomes more significant since the dead space can be considered as a delay of impact ionisation process and increases the duration of the avalanche process. Hence the dead space effect needs to be accounted for high speed APD design and bandwidth will be overestimated if it is ignored.

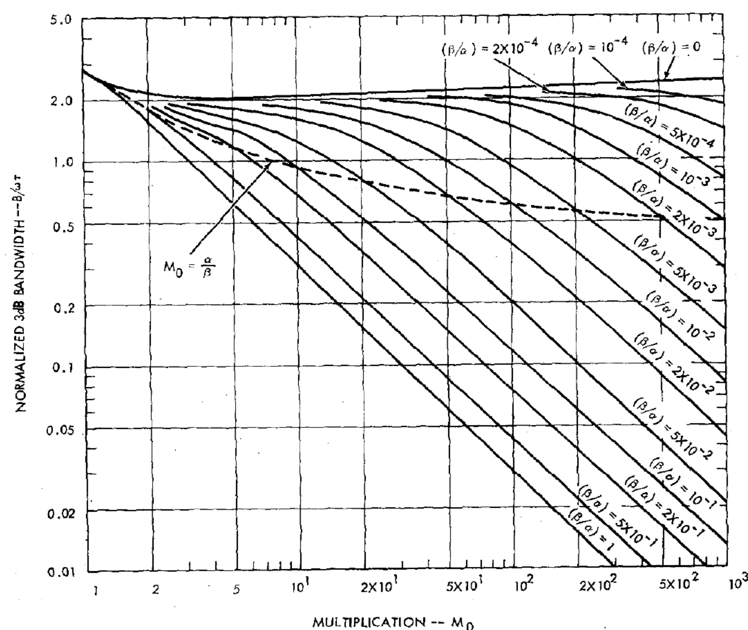

Figure 1.2.5 Frequency response predictions for various ratios of β/α [31].

Therefore an ideal APD should be capable of operating at large M, with low F and high GBP. In separate absorption and multiplication APDs (SAM APDs) the light is only absorbed in the absorption region and one carrier type is injected into the multiplication region. This improves the APD speed and noise for multiplication materials generally are utilised with high ionisation coefficient ratios. When the electron and hole ionisation coefficient is comparable and approaches unity, the ionisation noise increases and the process takes longer. In addition the hetero-junction in SAM APDs can cause carrier trapping at the interface of valence or conduction band discontinuity. The carriers escape

by tunelling or thermionic emission, the latter will reduce the APD response speed. The alloy compositional grading layer can be introduced to the hetero-interface to reduce the offset of the band-discontinuity, which greatly reduce the carrier trapping effect. In addition electric field profile optimisation should be considered for the SAM APDs design. The electric field should be low enough to avoid the band to band tunelling current in the narrow bandgap material [32], but high enough to achieve significant impact ionisation in the wide-bandgap materials. Based on calculations using the Poisson equation [28], the difference in electric field between the absorption and multiplication region requires a highly controlled doping concentration in a control layer referred to as the charge sheet layer and sandwiched between the absorption and multiplication region. The typical SAM APD and its electric field profile is shown schematically in figure 1.2.6.

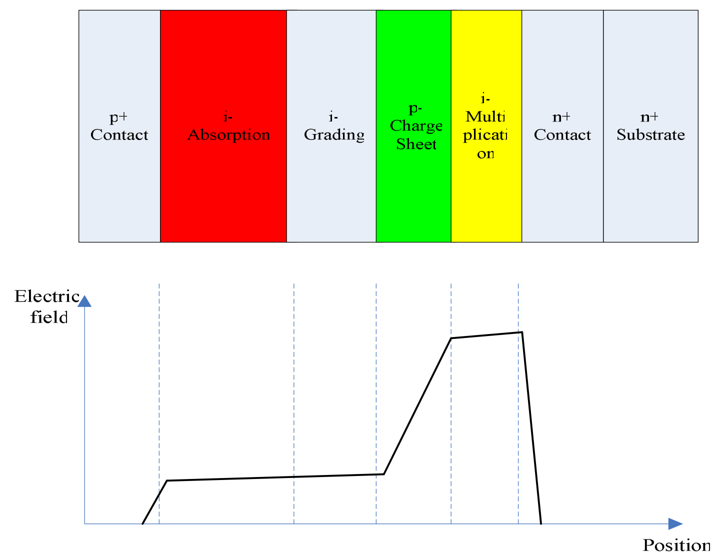

Figure 1.2.6 Schematic diagram and electric field profile in a typical SAM APD.

1.2.3 Review of high speed APDs

Currently commercial APDs utilising $In_{0.53}Ga_{0.47}As$ absorption and an InP multiplication layer have been widely employed for 10 Gb/s optical fibre communication systems. However, their typical GBPs of 80-120 GHz [30] with low bandwidths of 3-10 GHz [33] at M below 10 are insufficient to provide sufficient advantages over p-i-n photodiodes when operating at bit rates > 10 Gb/s. In addition the similar electron and hole ionisation coefficients in InP resulted in excess noise factor, F, corresponding to k of 0.25 ~ 0.4 [34]. Reducing the thickness of InP in these diodes can improve GBP and reduce F but at the

expense of a rapid increase in the tunnelling current. Hence the shot noise limits the multiplication layer width, *w*, to ~ 0.18 μm [35]. $In_{0.52}Al_{0.48}As$ (hereafter InAlAs), with a larger bandgap and lower *k* [36] compared to InP, was considered to be a promising material for improving frequency response and noise performance over InGaAs/ InP SAM APDs. The typical GBP values reported for InGaAs/InAlAs SAM APDs are 130-180 GHz [37] and *F* corresponding to *k* of 0.15 ~ 0.25 [38] for *w* ranges from 0.15 to 0.4 μm. M. Lahrichi *et al.* [39] recently reported an InGaAs/InAlAs SAM APD with a GBP of 240 GHz using *w* = 100 nm. However high dark current, mostly probably due to significant tunnelling current will reduce system sensitivity requirements [40]. Ge/Si APDs, utilizing Ge absorption region and Si multiplication layer, were reported to achieve a high GBP of 340 GHz and a low *k* value of ~ 0.08 [41]. However this promising technology currently has limited RC-limited bandwidth at $M < 10$ as well as high dark current and lower responsivity compared to commercial InP APDs. To date, to the best of our knowledge, the best APD performance at 40 Gb/s was reported by Makita *et al.* [42] who have demonstrated a high bandwidth APD up to 35 GHz (at $M = 2 \sim 3$) by using an InGaAs/InAlAs APD. The thickness of the InAlAs multiplication layer is 100 nm and the APD showed a GBP of 140 GHz. The bandwidth at low *M* is sufficient for 40 Gb/s system applications. However the diode showed a rapidly increasing dark current under the reverse bias between 10 to 15.5 V due to the unavoidable tunnelling current in such thin multiplication layer [42]. In addition the relatively low GBP of 140 GHz is most likely due to RC effects. The general trend in the experimental GBP of APDs is shown in figure 1.2.7.

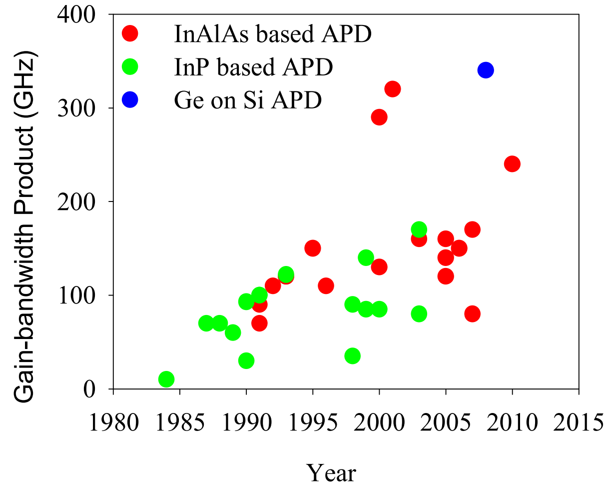

Figure 1.2.7: Gain-bandwidth products reported for InP, InAlAs and Ge/Si APDs.

In order to improve the GBP in APDs by removal the RC effect, Shi *et al.* [43] simulated and analysed APD structure utilising a travelling wave electrode design and predicted it could have high saturate power bandwidth and superior microwave-guiding structure.

1.3 Temperature dependence of breakdown and wide bandgap based APDs

It is well known that the impact ionisation process in APDs is strongly dependent on temperature and therefore an external biasing circuit to maintain a constant gain is necessary to achieve reproducible performance. Breakdown voltage of devices were estimated by using Miller's empirical expression $M = 1/(1-(V/V_{bd})^c)$ [44] where V is the reverse bias voltage, V_{bd} is the breakdown voltage and c is an adjustable parameters and determines the shape of the multiplication curve but independent of V_{bd}. By assuming c = 1, V_{bd} can be rewritten as $V_{bd} = V/(1-1/M)$ and determined from the V intercept of the plot of V versus $1/M$. The values can be compared with the reverse dark current-voltage measurements for consistency. The temperature coefficient of breakdown voltage, C_{bd} = $\Delta V_{bd}/\Delta T$, where ΔV_{bd} and ΔT are the breakdown voltage and temperature differences, provides a measure of the temperature dependence of the avalanche multiplication. In most wide bandgap semiconductors such as Si, GaAs, $Al_xGa_{1-X}As$, $Ga_{0.52}In_{0.48}P$ (here

after GaInP), InP and InAlAs, the avalanche multiplication reduces with increasing temperature. Figure 1.3.1 shows a typical temperature dependence of multiplication performance in wide bandgap materials.

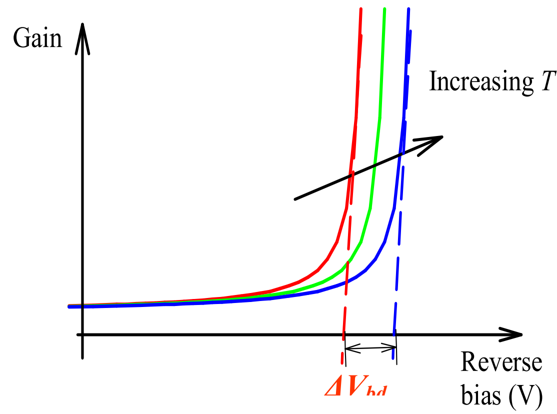

Figure 1.3.1: Typical temperature dependence of multiplication in wide bandgap materials.

Small C_{bd} can be obtained in materials with large bandgaps and in diodes with thin w. Massey *et al.* [45] reported C_{bd} varying from 20 to 1.53 mV/K in Si diodes when w reduces from 0.8 to 0.1 µm while Groves *et al.* [46] observed that C_{bd} drops from 28 to 0.56 mV/K in GaAs diodes as w reduces from 1 to 0.025 µm. Ma [47] and Groves [48] *et al*. both reported C_{bd} in $Al_xGa_{1-x}As$ falls with decreasing w for all alloy compositions. The smallest rate of change is reported for $x = 0.6$, in which C_{bd} reduces from 20 to 3 mV/K when w reduces from 1 to 0.1 µm. A small value of C_{bd} in thin w was also observed in GaInP [49] (3.68 mV/K for $w = 0.2$ µm), InP [50] (6 mV/K for $w = 0.1$ µm) and InAlAs [49, 51] (2.5 mV/K for $w = 0.13$ µm).The dependence of C_{bd} on w can be attributed to the reduced phonon scattering effects at high electric field in thin w leading to a weaker temperature dependence of avalanche gain.

Thin w is also known to improve APD performance by lowering the excess avalanche noise via the dead space effects [35] and increasing the GBPs, due to reduce the carrier transit time [35]. The excess noise factor at $M = 8$ for GaAs [48], $Al_{0.15}Ga_{0.85}As$ [52], $Al_{0.3}Ga_{0.7}As$ [52], $Al_{0.6}Ga_{0.4}As$ [53], $Al_{0.8}Ga_{0.2}As$ [52], GaInP [49], InP [34] and InAlAs

[38] with a range of w is shown in figure 1.3.2. The excess noise factor for different materials with different w is shown in table 1.1. The lower noise in thinner w is due to stronger dead space charge effect. Under pure electron injection the excess noise factor in $Al_{0.8}Ga_{0.2}As$ increases from 2.4 to 4.0 as w increases from 0.08 to 0.31 μm, before decreasing to 3.0 as w increases to 1.0 μm. InAlAs shows a similar trend in which the excess noise factor under pure electron injection increases from 2.8 to 3.2 as w increases from 0.1 to 1.0 μm before decreasing gradually to 2.6 as w increases to 2.5 μm. A maximum excess noise factor is observed for $Al_{0.8}Ga_{0.2}As$ with w = 0.31 μm and InAlAs with w = 1.0 μm. At low fields in devices with thick w, large ionisation coefficient ratios lead to low noise. In general the ionisation coefficient is known to decrease with w. The noise therefore increases with decreasing w before the dead space effects reduces the excess noise again at high fields in very thin w.

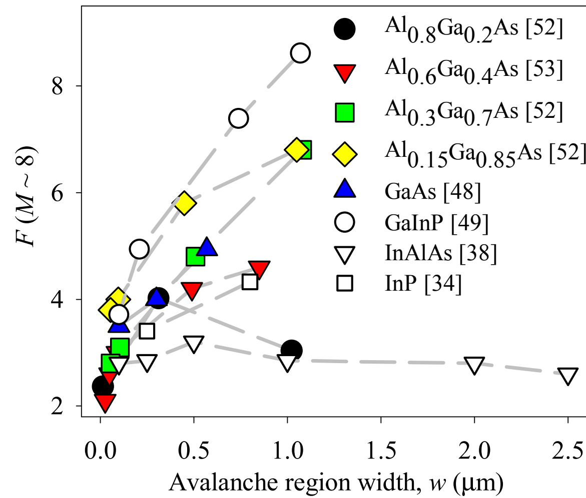

Figure 1.3.2 Excess noise measured at the $M \sim 8$ with $Al_{0.8}Ga_{0.2}As$ (●) [52], $Al_{0.6}Ga_{0.4}As$ (▼) [53], $Al_{0.3}Ga_{0.7}As$ (■) [52], $Al_{0.15}Ga_{0.85}As$ (◆) [52], GaAs (▲) [48], GaInP (○) [49] and InAlAs (▽) [38] for pure electron injection and InP (□) [34] for pure hole injection.

Table 1.1 Excess noise factor comparison for different materials with different w.

Type of carrier initiating the multiplication	Materials	w (μm)	F	w (μm)	F
	$Al_{0.6}Ga_{0.4}As$	0.85	4.6	0.026	2.1
	$Al_{0.3}Ga_{0.7}As$	1.08	6.8	0.055	2.8

Electron	$Al_{0.15}Ga_{0.85}As$	1.05	6.8	0.055	3.8
	GaAs	0.57	4.94	0.1	3.5
	GaInP	0.57	8.6	0.1	3.1
Electron	$Al_{0.8}Ga_{0.2}As$	0.31	4.0	0.08	2.4
		0.31	4.0	1.0	3.1
	InAlAs	1.0	3.2	0.1	2.8
		1.0	2.85	2.5	2.6
Hole	InP	0.8	4.3	0.25	3.4

Although small values of C_{bd}, low excess noise factor and high GBPs can be obtained by using thin avalanche regions, the onset of the exponentially rising band to band tunelling current with electric field in thin w imposes a lower limit to practical avalanche region width. For instance Ong *et al*. [40] recently reported that to achieve the optimum sensitivity at a bit rate of 10 Gb/s with a bit error rate of 10^{-12} the minimum values of w for telecom APDs are 180 and 150 nm for InP and InAlAs avalanche regions respectively, before noise increases rapidly due to tunelling current. But the band to band tunelling is well known that reduced in wide bandgap and in indirect bandgap materials. For instance, if the onset of tunelling current in the diode is defined as the field corresponding to a current density of 10^{-4} A/cm^2, the tunelling onset can be observed in InAlAs and InP at fields of ~ 650 kV/cm [51] and ~ 600 kV/cm [22] respectively. On the other hand the dark current density in GaInP [49], $Al_{0.52}In_{0.48}P$ [54] and $Al_{0.6}Ga_{0.4}As$ [55] can be below 10^{-7} A/cm^2 under the higher field of 1 MV/cm, due to their wider bandgaps compared than InAlAs and InP.

In summary, new materials either with significantly superior ionisation coefficient ratios or much lower tunelling currents to achieve much thinner avalanche regions will be necessary to obtain low excess noise factor, and high GBPs significantly above 300 GHz to provide major improvement over conventional InGaAs p-i-n photodiode at 40 Gb/s. Thin avalanche region will also provide low temperature coefficients of breakdown voltage.

1.4 Organisation of thesis

The primary motivation of this thesis is to fabricate high speed and high efficiency photodetectors for fiber optical communication systems based on InGaAs and InGaAs/InAlAs material systems. AlAsSb, lattice matched to InP, as an alternative material for InAlAs, was also investigated for next generation high performance APD applications.

Chapter 1 introduces the high speed photodiodes and APDs for optical communication system and temperature dependence of avalanche multiplication in APDs.
Chapter 2 provides the background theory of the travelling wave photodiode design. The experimental techniques used to characterise the devices in this thesis are also described.
Chapter 3 describes the fabrication optimisation process for high speed photodiodes.
Chapter 4 presents the characterisation of waveguide InGaAs p-i-n photodiodes with improved bandwidth-efficiency product compared to the vertically illuminated diodes fabricated from the same wafer.
Chapter 5 presents the characterisation of InGaAs/InAlAs APDs with travelling wave electrode design. Low dark current, low excess noise, wide bandwidth and high GBP were demonstrated for our APDs.
Chapter 6 presents the photomultiplication and temperature dependence of AlAsSb based p-i-n APDs. A study of tunelling current in AlAsSb is also described.
Chapter 7 presents characterisation of photomultiplication and excess noise of a novel InGaAs/AlAsSb SAM APD.
Chapter 8 concludes the thesis with a summary and suggestions for future work.

1.5 Reference

[1] K. Kato, "Ultrawide-Band/High-Frequency Photodetectors," *IEEE Trans. Microw. Theory Tech.*, vol. 47, pp. 1265–1281, Jul. 1999.
[2] N. Dagli, "High Speed Photonic devices," R. G. W. Brown and E. R. Pike, Eds. Santa Barbara, USA: Taylor & Francis Group, LCC, 2007.

[3] H.Ogawa and D. Polifko, "Fiber optic millimeter-wave subcarrier transmission links for personal radio communication systems," *IEEE MTT-S Symp. Dig.,* pp 555–558, 1992.

[4] H. Schmuck, R. Hofstetter, and R. Heidemann, "Advanced fiber-optic distribution of 140 Mbit/s mm-wave signals at 36 GHz," in *ECOC'94*, pp. 41–44, 1994.

[5] X. Zheng, "Long wavelength high speed Photodiodes and APD Arrays," in *EEE. Doctor of Philosophy*: The University of Texas at Austin, 2004.

[6] J. Bowers and Jr. C. A. Burrus, "Ultrawide-band long wavelength p-i-n photodectors", *J. Lightwave Tech.*, vol 5, Oct. 1987.

[7] I. Kimukin, N. Biyikli, B. Butun, O. Aytur, S. M. Unlu and E. Ozbay, "InGaAs-based high performance p-i-n photodiodes," *IEEE Photon. Technol. Lett.*, vol. 14, pp. 366–368, 2002.

[8] N. Shimizu, N. Watanabe, T. Furuta and T. Ishibashi, "Improved response of uni-travelling-carrier photodiodes by carrier injection," *J. Appl. Phys.,* vol. 37, pp. 1424-1426, 1998.

[9] T. Ishibashi, S. Kodama, N. Shimizu and T. Furuta, "High-speed response of uni-travelling-carrier photodiodes," *J. Appl. Phys.,* vol. 36, pp. 6263-6268, 1997.

[10] T. Ishibashi, T. Furuta, H. Fushimi, S. Kodama, H. Ito, T. Nagatsuma, N. Shimizu and Y. Miyamoto "InP/InGaAs uni-travelling-carrier photodiodes," *IEICE Trans. Electron..,* vol. E83-c, pp. 938-949, 2000..

[11] K. Kato, A. Kozen, Y. Muramoto, Y. Itaya, T. Nagatsuma, and M. Yaita, "110-GHz, 50% efficiency mushroom-mesa waveguide p-i-n photodiode for a 1.55 μm wavelength," *IEEE Photon. Technol. Lett.*, vol. 6, pp. 719–721, 1994.

[12] A. Beling, H. G. Bach, G. G. Mekonnen, R. Kunkel and D. Schmidt, "Miniaturized waveguide-integrated p-i-n photodetector with 120-GHz bandwidth and high responsivity," *IEEE Photon. Technol. Lett.*, vol. 17, pp. 2152–2154, 2005.

[13] K. S. Giboney, M. J. W. Rodwell and J. E. Bowers, "Travelling-wave photodetector design and measurements," *IEEE J. Select. Topics Quantum Electron.*, vol. 2, pp. 622-629, 1996.

[14] K. S. Giboney, M. J. W. Rodwell and J. E. Bowers, "Travelling-wave photodetectors," *IEEE Photon. Technol. Lett.*, vol. 4, pp. 1363-1365, 1992.

[15] Y. J. Chiu, "Sub-terahertz travelling-wave low-temperature grown-GaAs P-I-N photodtector," in *EEE. Doctor of Philosophy*: The University of California, Santa Barbara, 1999.

[16] Y. J. Chiu, S. B. Fleischer and J. E. Bowers, “High speed and low-temperature grown GaAs p-i-n travelling-wave photodector,” *IEEE Photon. Technol. Lett.*, vol. 10, pp. 1012-1014, 1998.

[17] J.-W. Shi, K. G. Gan, Y. J. Chiu, Y.-H. Chen, C.-K. Sun, Y. J. Yang, and J. E. Bowers, “Metal-semiconductor-metal travelling-wave-photodetectors,” *IEEE Photon. Technol. Lett*., vol. 13, pp. 623–625, 2001.

[18] J.-W. Shi, K. G. Gan, Y.-H. Chen, C.-K. Sun, Y. J. Chiu, and J. E. Bowers, “Ultra-high power-bandwidth product and nonlinear photo-conductance performances of low-temperature-grown GaAs based metal-semiconductor-metal travelling-wave photodetectors,” *IEEE Photon. Technol. Lett.*, vol. 14, pp. 1587–1589, 2002.

[19] A. Stohr, R. Heinzelmann, C. Kaczmarek, and D. Jager, “Ultra-broadband K to W-band 1.55 _m travelling-wave photomixer,” *Electron. Lett.,* vol. 36, pp. 970–972, 2000.

[20] C. Groves, "High performance analogue and Geiger-mode avalanche photodiodes," in *EEE. Doctor of Philosophy*: The University of Sheffield, 2004.

[21] Y. L. Goh, "Impact ionisation in InGaAs, InAlAs and InGaAs/GaAsSb superlattices for near infrared avalanche photodiodes," in *EEE. Doctor of Philosophy*: The University of Sheffield, 2008.

[22] L. J. J. Tan, "Telecommunication wavelength InP based avalanche photodidoe," in *EEE. Doctor of Philosophy*: The University of Sheffield, 2008

[23] R. J. McIntyre, “Multiplication noise in avalanche photodiodes”, *IEEE Trans. Electron Devices*, vol. 13, no. 1, pp. 164–168, Jan. 1966.

[24] M. M. Hayat, B. E. A. Saleh and M. C. Teich, “Effect on dead space on gain and noise of double-carrier-multiplication avalanche photodiodes”, *IEEE Trans. Electron Devices*, vol. 39, no. 3, pp. 546-552, Mar. 1992.

[25] D. S. Ong, K. F. Li, G. J. Rees, J. P. R. David, and P. N. Robson, “A simple model to determine multiplication and noise in avalanche photodiodes”, *J. Appl. Phys.*, vol. 83, no. 6, pp. 3426-3428, Mar. 1998.

[26] T. P. Pearsall and M. A. Pollack, “Compound semiconductor photodiodes”, *Semiconductors and semimetals, Academic Press, Inc*. vol. 22, pp. 173-245, 1985.

[27] R. B. Emmons, “Avalanche photodiode frequency response,” *J. Appl. Phys*., vol. 38, no. 9, pp. 3705–3714, 1967.

[28] F. Zappa et al, “Solid-state single-photon detectors,” *Opt. Eng*., vol. 35, no. 4, pp. 938-945, 1996.

[29] X. Zheng, J. Hsu, X. Sun, J. B. Hurst, X. Li, S. Wang, A. L. Holmes, and J. C. Campbell, "A 12 x 12 In0.53Ga0.47As/In0.52Al0.48As avalanche photodiode array," *IEEE J. Quant. Elec.,* vol. 38, pp. 1536-40, 2002.

[30] C. H. Tan, J. S. Ng, S. Xie and J. P. R. David, “Potential materials for avalanche photodiodes operating above 10Gb/s*”, International conference on computers and devices for communication (CODEC’09)*, 2009.

[31] R. B. Emmons, “Avalanche photodiode frequency response,” *J. Appl. Phys*., vol. 38, no. 9, pp. 3705–3714, 1967.

[32] X. Sun, "High Performance 1300 nm Photodetectors Grown By Molecular Beam Epitaxy." in *EEE. Doctor of Philosophy*: The University of Texas at Austin, 2002.

[33] C. Lenox, H. Nie, P. Yuan, G. Kinsey, A. L. Homles, Jr., B. G. Streetman and J. C. Campbell, “Resonant-cavity InGaAs-InAlAs avalanche photodiodes with gain-bandwidth product of 290GHz,” *IEEE Photon. Technol. Let*., vol. 11, pp. 1162–11655, Sep. 1999.

[34] L. J. J. Tan, J. S. Ng, C. H. Tan and J. P. R. David, “Avalanche noise in submicron InP diodes”, *IEEE J. of Quantum Electron.*, vol.44, pp.378-382, 2008.

[35] S. Xie and C. H Tan, “AlAsSb avalanche photodiodes with a sub-mV/K temperature coefficient of breakdown voltage”, *IEEE J. of Quantum Electron.,* Nov. 2011.

[36] Y. L. Goh, D. J. Massey, A. R. J. Marshall, J. S. Ng, C. H. Tan, W.K. Ng, G. J. Rees, M. Hopkinson, J. P. R. David, and S. K. Jones, “Avalanche multiplication in InAlAs,” *IEEE Trans. Electron Devices*, vol. 54, no. 1, pp. 11–17, Jan. 2007.

[37] C. H. Tan, S. Xie and J. Xie, “Low noise avalanche photodiodes incorporating a 40nm AlAsSb avalanche region”, *IEEE J. of Quantum Electron.,* Jan. 2012.

[38] Y. L. Goh, D. J. Massey, A. R. J. Marshall, J. S. Ng, C. H. Tan, W. K. Ng, G. J. Rees, M. Hopkinson and J. P. R. David, "Excess noise in $In_{0.52}Al_{0.48}As$", *IEEE J. of Quantum Electron.*, vol.43, pp.503-507, 2007.

[39] M. Lahrichi, G. Glastre, E. Derouin, D. Carpentier, N. Lagay, J. Decobert and M. Achouche , "240-GHz gain-bandwidth-product back-side illuminated AlInAs avalanche photodiodes," *IEEE Photon. Technol. Let.*, vol. 22, pp. 1373–1375, Sep. 2010.

[40] D. S. G. Ong, M. M. Hayat, J. P. R. David and J. S. Ng, "Sensitivity of High-Speed Lightwave System Receivers Using InAlAs Avalanche Photodiodes," *IEEE Photon. Technol. Let.*, vol. 23, no. 4, pp. 233–235, Feb. 2011.

[41] Y. M. Kang, H. D. Liu, M. Morse, M. J. Paniccia, M. Zadka, S. Litski, G. Sarid, A. Pauchard, Y. H. Kuo, H. W. Chen, W. S. Zaoui, J. E. Bowers, A. Beling, D. C. McIntosh, X. G. Zheng, and J. C. Campbell, "Monolithic germanium/silicon avalanche photodiodes with 340 GHz gain-bandwidth product," *Nature Photonics*, vol. 3, pp. 59-63, 2009.

[42] K. Makita, T. Nakata, K. Shiba and T. Kakeuchi, "40Gbps waveguide photodiodes", *J. of Adv. Tech*., Summer, 2005.

[43] J. W. Shi, Y. H. Liu and C. W.Liu, "Design and analysis of separate-absorption-transport-charge-multiplication travelling-wave avalanche photodetectors," *J. Lightwave Tech.*, vol 22, 2004.

[44] S. L. Miller, "Avalanche breakdown in Germanium", *Physical Review*, vol. 99, no. 4, pp. 1234-1241, 1955.

[45] D. J. Massey, J. P. R. David, and G. J. Rees, "Temperature dependence of impact ionisation in submicrometer Silicon devices," *IEEE Trans. Electron Devices*, vol. 53, no. 9, pp. 2328–2334, Sep. 2006.

[46] C. Groves, R. Ghin, J. P. R. David, and G. J. Rees, "Temperature dependence of impact ionisation in GaAs," *IEEE Trans. Electron Devices*, vol. 50, no.10, pp. 2027–2031, Oct. 2003.

[47] F. Ma, G. Karve, X. G. Zheng, X. G. Sun, A. L. Holmes, and J. C. Campbell, "Low temperature breakdown properties of AlxGa1-x As avalanche photodiodes," *Appl. Phys. Let.,*, vol. 81, no. 10, pp. 1908–1910, Sep. 2002.

[48] C. Groves, C. N. Harrison, J. P. R. David, and G. J. Rees, “Temperature dependence of breakdown voltage in AlxGa1-x As,” *J. Appl. Phys.*, vol. 96, no. 9, pp. 5017–5019, Aug. 2004.

[49] R. Ghin, J. P. R. David, M. Hopkinson, M. A. Pate, G. J. Rees, and P. N. Robson, , “Impact ionisation coefficients in GaInP p–i–n diodes”, *Appl. Phys. Let.*, vol. 81, pp. 6916–6919, Apr. 1997.

[50] L. J. J. Tan, Y. L. Goh, S. C. Liew-Tat-Mun, D. S. G. Ong, J. S. Ng and J. P. R. David, “Temperature dependence of breakdown in InP and InAlAs”, *IEEE Trans. Electron Devices*, vol. 46, no. 8, pp. 1153 – 1157, Aug. 2010.

[51] Y. L. Goh, D. J. Massey, A. R. J. Marshall, J. S. Ng, C. H. Tan, W.K. Ng, G. J. Rees, M. Hopkinson, J. P. R. David, and S. K. Jones, “Avalanche multiplication in InAlAs,” *IEEE Trans. Electron Devices*, vol. 54, no. 1, pp. 11–17, Jan. 2007.

[52] B. K. Ng, J. P. R. David, C. H. Tan, S. A. Plimmer, G. J. Rees, R. C. Tozer and M. Hopkinson, “Avalanche multiplication noise in bulk and thin $Al_xGa_{1-x}As$ ($x = 0 – 0.8$) PIN and NIP diodes,” *Photonics West 2001* (SPIE Symposium on Integrated Optics 2001) in San Jose, California, Jan. 2001.

[53] C. H. Tan, J. P. R. David, S. A. Plimmer, G. J. Rees, R. C. Tozer and R. Grey, “Low multiplication noise thin $Al_{0.6}Ga_{0.4}As$ avalanche photodiodes,” *IEEE Trans. Electron Devices*, vol. 48, pp. 1310 – 1317, Jul. 2001.

[54] J. S. L. Ong, J. S. Ng, A. B. Krysa, and J. P. R. David, “Impact Ionisation Coefficients of AlInP”, *IEEE Electron. Devices Lett.*, vol. 32 , no. 11, pp. 1528-1530, Nov. 2011.

[55] B. K. Ng, "Impact ionisation in wide band gap semiconductors: $Al_xGa_{1-x}As$ and 4H-SiC," in *EEE. Doctor of Philosophy*: The University of Sheffield, 2002.

Chapter 2 Theory and Design of travelling wave photodetectors and characterisation techniques

Chapter 1 presented the importance of high speed photodetectors, particularly for coping with the increasing internet traffic, and the need for development of low dark current, high bandwidth, high gain-bandwidth product (GBP) and low multiplication excess noise APDs for optical networks operating at bit-rates of 40, 100 Gb/s and higher. The response of APDs in terms of low dark current and low excess noise has been considered in Chapter 1. This chapter focuses on the design of high speed APDs using travelling wave structures. By appropriate geometry design, matching of the microwave impedance of the diodes to the load can be achieved to minimise the reflected microwave power [1], leading to optimised APD speed. Experiment techniques for characterisation of APDs are also presented.

2.1 Theory of travelling wave diode

2.1.1 Transmission line

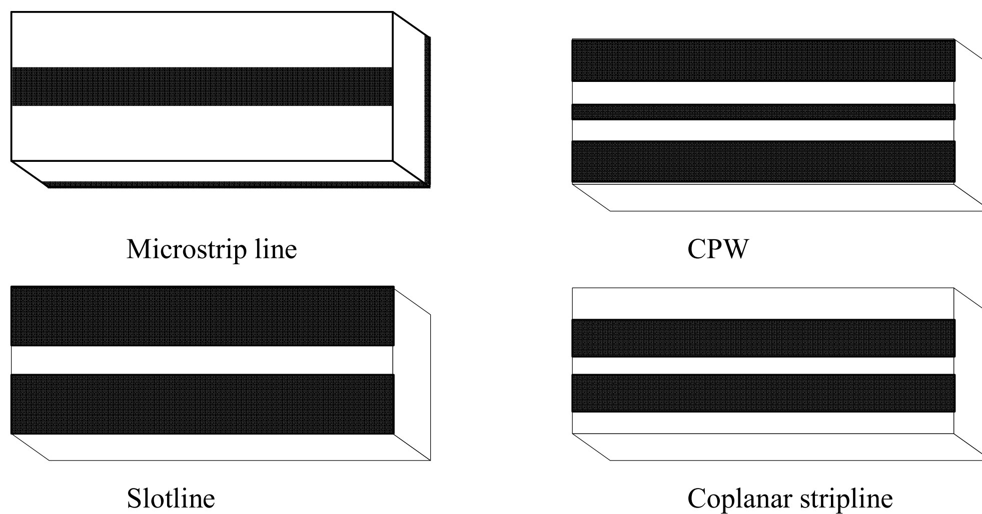

Figure 2.1.1 Schematic planar microwave transmission line.

Traditionally microstrip line, which has an upper signal track and bottom ground planes with a dielectric slab in the middle as illustrated in figure 2.1.1, is the most widely used transmission line. This structure is fabricated in a highly conducting substrate and can be characterised as transverse electromagnetic (TEM) at very low frequency (3 ~ 30 kHz) or

quasi TEM mode up to some high frequency range (3 ~ 30 MHz) [2], which shows the transverse field of microwave signal is much larger than the longitudinal field due to the boundary conditions. However for the communication system operating at higher bit-rates of 100 Mb/s, the traditional microstrip line is not appropriated. Its highly conducting substrate will introduce a large microwave loss from the substrate due to skin effect, and its characteristic impedance depends directly on the substrate thickness, causing some difficulty of repeatability from batch to batch. In addition in order to avoid high order mode propagation at high frequency, the substrate needs to be very thin and therefore the additional substrate thinning process increases the fabrication difficulty. Hence the in-plane structures such as coplanar waveguide (CPW), slotline and coplanar stripline, as shown in figure 2.1.1 are more popular for high bit-rate communication systems. They have a ground and signal contacts deposited on the same substrate so that a semi-insulating, instead of a current conducting substrate, can be used. The backside process for microstrip line structure, such as backside metallisation, substrate thinning, via hole can be bypassed. Therefore the thick semi-insulating substrate can provide advantage for hand held measurement and integration with electronic components in integrated circuits. Moreover the large microwave loss from the conducting substrate and the introduction of the inductance by via hole at high frequency, which resulted in low circuit efficiency, can be minimised. In addition the characteristic impedance for these in-plane structures is only dependent on the signal pad width and the gap between signal and ground pads, with minimal influence from the semi-insulating substrate. Therefore their characteristic impedance can be designed to match the external load impedances. Figure 2.1.2 (a) shows the schematic of a CPW. Using transmission line calculator (TXLINE) software [3] the typical gap width versus signal pad width for different characteristic impedances on InP substrate is calculated as shown in figure 2.1.2 (b).

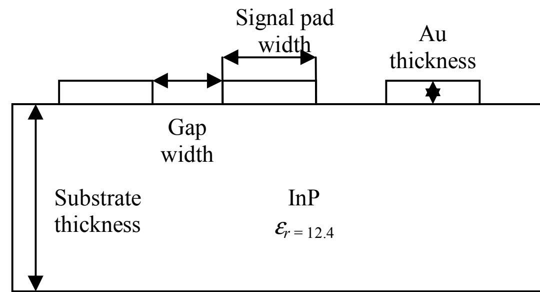

(a)

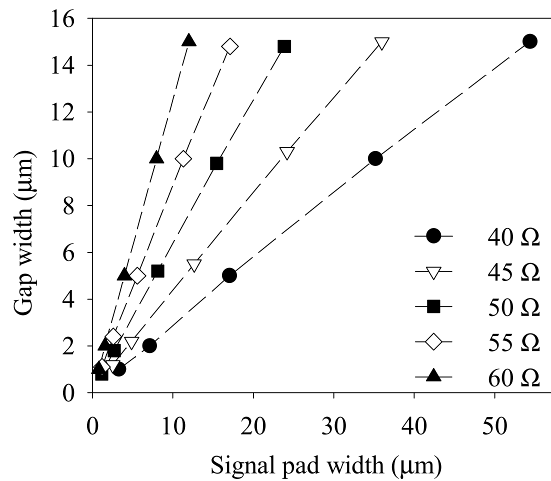

(b)

Figure 2.1.2 (a) Schematic of CPW (b) typical calculated gap width versus signal pad width for different characteristic impedances for CPWs on InP substrate at the frequency of 40 GHz, assuming substrate thickness = 100 μm and Au metallisation thickness = 0.5 μm.

However CPW cannot be directly fabricated on the active diodes. The metal plate are connected with high doping semiconductor materials (p^+ or n^+) to connect to the depletion region instead of on the substrate, as shown in figure 2.1.3 (b). An appropriate approach is to use the hybrid CPW structure that combines the microstrip and CPW structure, and has been successfully used in fabricating high speed travelling wave photodiodes (TWPDs) [4, 5]. The currents are primarily carried in the metal and nearly all of the voltage drops across the depletion region. The electric field pattern is close to microstrip. The CPW metal layers convey the microwave signal and thus the magnetic field distribution is nearly that of CPW. Figures 2.1.3(a) and (b) show the typical top view and the cross section of hybrid CPW structure. Because of the coplanar metal tracks,

CPW has the advantage of being compatible with monolithic microwave integrated circuit using simple semiconductor fabrication process. This high speed CPW design also facilitates measurement using widely available microwave probe tips.

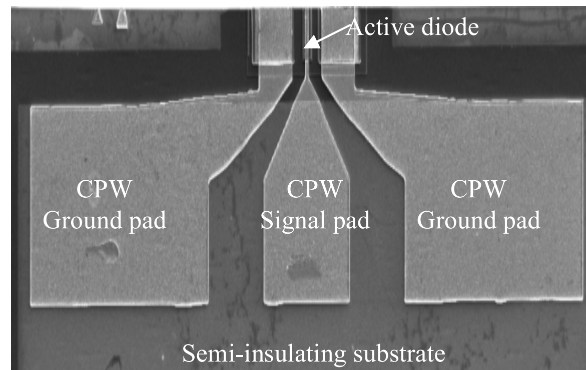

(a)

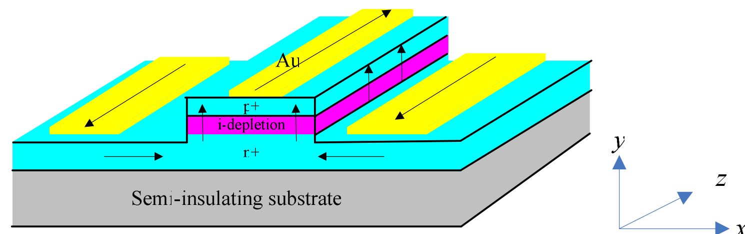

(b)

Figure 2.1.3 (a) Top view (b) cross section of hybrid CPW structure.

2.1.2 Equivalent circuit model

Since the targeted characteristic impedance of the CPW can be achieved by adjusting its signal pad width and gap width, appropriately designed hybrid CPW using an active APD to match the external circuit impedance is crucial for the large bandwidth requirement. An equivalent circuit model can be employed to accurately represent the electrical characteristics of the active diode, since it has been verified by the full-wave analysis technique by solving the Maxwell equations [5-7]. The APD dimensions and material parameters, shown in figure 2.1.4 (a), are used to calculate the transmission line propagation. By assuming that each semiconductor layer can be represented by the equivalent circuit shown in figure 2.1.4 (b) we can simplify the hybrid CPW to the equivalent circuit of figure 2.1.4 (c).

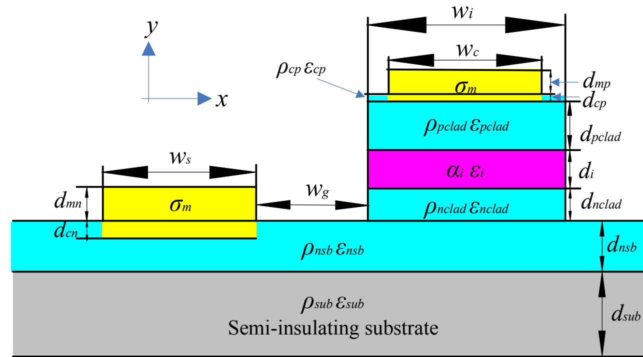

(a)

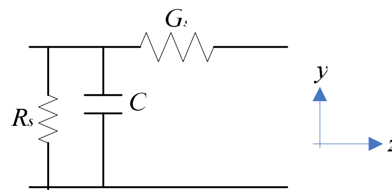

(b)

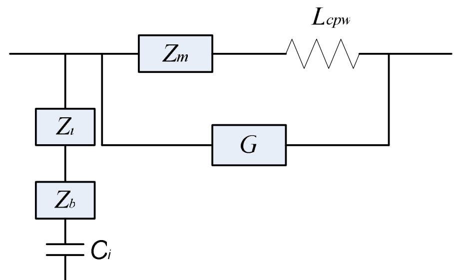

(c)

Figure 2.1.4 (a) Hybrid-coplanar active diode structure dimensions and material parameters; (b) equivalent circuit of semiconductor cladding layer; (c) the corresponding equivalent circuit of the transmission line.

The equations used to design and analyse the transmission line propagation of the diodes are listed in table 2.1[5-7] and all quantities are expressed in per unit length.

Table 2.1 Hybrid-coplanar active diodes equations for the equivalent circuit model in figure 2.1.4. ρ is resistivity and $\sigma = 1/\rho$ is conductivity; ε and μ are permittivity and permeability. η_{ym0} is the metal-air transverse wave impedance, η_m is the wave impedance in metal, and δ_{sm} is the skin

depth in metal. The coplanar waveguide inductance, L_{CPW} is calculated from numerical model. The dimensions and material characteristics are indicated in figure 2.1.4.

$$Z_m = \frac{\eta_{ym0}}{w_c} \qquad L_i = L_{CPW} \qquad C = \varepsilon \frac{w_i}{d}$$

$$\eta_{ymot} = \eta_m \coth[(1+j)\frac{d_{mp}}{\delta_{sm}}] [8, 9] \qquad \eta_m = \sqrt{j\omega\mu_0 / \sigma_m} \qquad \delta_{sm} = \sqrt{2/\omega\mu_0\sigma_m}$$

$$Z_{cp} = \frac{\rho_{cp}}{1 + j\omega\rho_{cp}\varepsilon_{cp}} \ln\frac{w_c}{w_i} \qquad Z_{pclad} = \frac{\rho_{pclad}}{1 + j\omega\rho_{pclad}\varepsilon_{pclad}} \qquad Z_{nclad} = \frac{\rho_{nclad}}{1 + j\omega\rho_{nclad}\varepsilon_{nclad}}$$

$$Z_b = \frac{\rho_{sb}}{1 + j\omega\rho_{sb}\varepsilon_{sb}} \cdot \frac{(w_i/6 + w_g + w_T)}{2d_{sb}} \qquad w_T = \sqrt{\frac{\rho_{cn}}{\rho_{sb}} \cdot \frac{1 + j\omega\rho_{sb}\varepsilon_{sb}}{1 + j\omega\rho_{sn}\varepsilon_{sn}} d_{cn} d_{sb}}$$

$$G_{cp} = \frac{(w_c + w_i)d_{cp}}{6\rho_{cp}} \qquad G_{pclad} = \frac{w_i d_{pclad}}{3\rho_{pclad}} \qquad G_{nclad} = \frac{w_i d_{nclad}}{3\rho_{nclad}}$$

$$Z_t = Z_{cp} + Z_{pclad} + Z_{nclad} \qquad G_l = G_{cp} + G_{pclad} + G_{nclad}$$

The transmission line propagation properties are determined by the capacitance, C, and the inductance L_i. The capacitance controls the electric field when the microwave travels through the transmission line, whereas the magnetic field is represented by the inductance L_i which is due to the current driven on the metal plate and the induced magnetic field surrounding the metal plate. The inductance can be approximated by $L_i = (\mu \cdot D)/w_i$ [10], where D is the distance between two plates, w_i is the width of plates and u is the permeability. However in the active diodes, the metal plates is not parallel, and InGaAs/InAlAs material system is not a magnetic material, so that the inductance L_i is considered equal to that of a CPW line of the same size (L_{CPW}) [11], which can be calculated from a commercial program such as LineCal [12] or by analytical forms [13] given in Appendix A.

Z_m arises from the finite conductivity of the metal plate. When the longitude time-varying current flows through the metal plates, it is not only inducing a magnetic field that

resulted in the inductance L_i and ohmic loss, it will also produce the alternating electric current to distribute itself within a conductor with the current density being largest near the surface of the conductor, decreasing at greater depth and cause an effective resistance of the conductor, known as skin effect [2]. As the frequency is higher, the resistance and inductance in the transmission line will increase and therefore the loss and dispersion effect will influence the electrical pulse transmitting. For instance, the skin depth is 0.34 μm in Au at a frequency of 50 GHz, and therefore thicker Au layer needs to be evaporated during the metallisation process. The bottom n-metal impedance is ignored since it is much smaller than the impedance of the top p-metal, Z_{mt}.

The impedance Z_t is composed of the impedances of the p-contact, p-cladding layer and n-cladding layer. Here the cladding layers are modelled as a resistor parallel to a capacitor in the transverse direction, and a conductance in the longitude direction, as shown in figure 2.1.4 (b). The longitude conductance is due to the conductance current flowing through the semiconductor which will generate a small amount of longitude electric field [14]. As with the bottom n-metal impedance, the conductance of the bottom semiconductor layer is neglected because it is much smaller than the p-top semiconductor layer, G_{st}. The bottom n-conducting layer, Z_b, is composed of terms accounting for the spreading resistance under the mesa, the bulk resistance of the gap, and the resistance of the ground contact. The spreading resistance includes a factor of 1/2 for the structure symmetry and a factor of 1/3 due to the current distribution. The bottom contact resistance is proportional to the transfer length, w_T. The whole impedance is multiplied with 1/2 because of the double ground lines.

Therefore the transmission line propagation characteristic can be simplified to the general transmission line equivalent circuit model and the circuit characteristics can be calculated by the current and voltage distributed through the transmission line, as shown in figure 2.1.5. The general characteristic impedance of the transmission line can be expressed as $Z_0 = \sqrt{Z/Y}$. In the mid-frequency range from about 10 GHz to several hundred gigahertz, the ideal transmission line phase velocity and characteristic impedance can be calculated as [1,2,4-9]:

$$v_m = \sqrt{1/L_iC_i} \tag{2.1.7}$$

$$Z_0 = \sqrt{L_i/C_i} \tag{2.1.8}$$

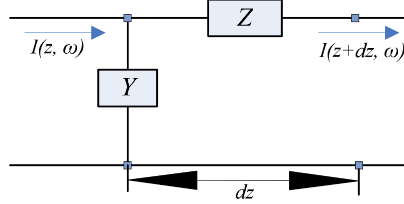

Figure 2.1.5 General transmission equivalent circuit model

2.2 Experimental characterisation techniques

2.2.1 Current-voltage (*I-V*) measurement

The forward and reverse dark *I-V* measurements can be performed using a Keithley 236/237 source measurement unit (SMU) or a Hewlett Packard(HP) 4101 pico ammeter, which can supply voltages up to 1100 V and 100 V respectively. The dark reverse *I-V* allows the leakage current and the breakdown voltage to be evaluated. The dark leakage current comprises the bulk leakage current and the surface leakage current. The bulk leakage current could be contributed by diffusion current from the cladding layers, the generation-recombination current I_{gr} in the depletion layers and the band to band tunelling current I_{tun}, which are all proportional to the cross-section area of the diode. The surface leakage current is due to the leakage path along the mesa periphery and therefore scales with the diode perimeter. *I-V* was measured from several diodes with different sizes. The contributions of the bulk leakage current and the edge leakage current were assessed by normalising the dark current to the device area J_A (A/cm^2) and perimeter J_P (A/cm).

The ideal forward current can be expressed as [15]

$$I_f(V) = I_0 \exp(qV/\eta k_B T) \tag{2.2.1}$$

where I_0 is the saturation current, q is the electron charge, k_B is Boltzmann's constant and T is the temperature. η is the ideality factor having values $1 < \eta < 2$, depending on the contributions from diffusion current and recombination current. Series resistance due to

resistance in the cladding layer and/or the metal contact, R_s, modifies the ideal forward diode current expression to

$$I_f(V) = I_0 \exp\left(\frac{(qV - I_f R_s)}{\eta k_B T} \right) \qquad (2.2.2)$$

The significant series resistance will affect the photomultiplication measurement due to voltage dropping across the resistance and therefore reducing the applied voltage across the depletion region leading to an uncertainty in the electric field profile of the device. The high series resistance resulted in a large RC-time constant in the diode and limits its speed. It is therefore important to quantify the series resistance. Heavily doped semiconductor layers in the diodes and metal optimisation by appropriate ohmic contact metal choice and thermal annealing process can be applied to minimise the series resistance.

2.2.2 Capacitance-voltage (*C-V*) measurement

C-V measurements were performed using a HP4275A LCR meter. A reverse DC bias voltage is applied to the diode with a superimposed sinusoidal test signal of 40 mV at a frequency of 1 MHz to measure the diode capacitance. The superimposed signal is considered sufficient enough for overcoming the system noise and without greatly influencing the DC bias voltage across the diode. The selected frequency is to ensure the measured impedance is dominated by the diode capacitance and the phase angle displayed on the LCR meter is close to 90 ºC.

The depletion width and the doping profile of the device can be estimated by fitting the *C-V* data. In order to minimise the error in extraction of the doping profile due to the uncertainty in the device area, the measured *C-V* of the largest diode was used in the fitting. By solving the one dimensional Poisson's equation [16], $\frac{d\xi}{dx} = \frac{qN'_k}{\varepsilon_0 \varepsilon_r}$, and considering the charge equilibrium condition in the structure with *m* regions, assuming that all regions, except the first and the *m*th region, are fully depleted and the doping level in each region is constant, the depletion width in the first region, X_1, and the *m*th region, X_m, and the total depletion width, w_t, can be calculated as (Appendix B)

$$X_1 = \frac{-b + \sqrt{b^2 - 4ac}}{2a}$$

$$X_m = -\frac{\sum_{k=1}^{m-1} N'_k X_k}{N'_m}$$

$$w_t = X_1 + \sum_{k=2}^{m-1} X_k + X_m \qquad (2.2.3)$$

where $a_1 = \frac{N'_1}{\varepsilon_1}(1 - \frac{\varepsilon_1 N'_1}{\varepsilon_m N'_m})$,

$$b_1 = \frac{2N'_1}{\varepsilon_1}(\sum_{k=2}^{m-1}(x_k - \frac{\varepsilon_1 N'_k x_k}{\varepsilon_m N'_m})),$$

and $c_1 = -\frac{\sum_{k=2}^{m-1}(N'_k x_k)^2}{N'_m \varepsilon_m} + \sum_{k=2}^{m-1}(\frac{N'_k x_k^2}{\varepsilon_k}) + \sum_{k=2}^{m-2}\frac{2N'_k x_k}{\varepsilon_k}\sum_{k=l+1}^{m-1} x_l - 2\frac{V_t}{q}$,

where q is the elementary electronic charge, N'_k is the doping concentration in the kth region, ε_k is the dielectric constant in the kth region and V_t is the given reverse bias voltage.

Under depletion width approximation, at a given reverse bias, V_t, the capacitance can be calculated as

$$C = \frac{A}{\sum_{k=1}^{m}(\frac{x_k}{\varepsilon_k})} \qquad (2.2.4)$$

2.2.3 Photomultiplication measurement

The photomultiplication measurements on the diodes were carried out by focusing the light from a laser source onto the top cladding of the diodes under reverse bias. Under sufficiently high electric field in the high field or avalanche region, the photogenerated carriers multiply via impact ionisation process. Consequently the photocurrent increases rapidly with the reverse bias voltage compared to the primary photocurrent arising from the photogenerated carriers injected into the depletion region. The total current, consists of photocurrent and dark leakage current, flowing through the diode was measured by the SMU. The photocurrent can be obtained by subtracting the dark leakage current from the

total current. This is reasonable when the dark leakage current is at least two orders of magnitude lower than the total current. However if there is insignificant difference between the dark leakage current and the total current, a phase-sensitive detection method [16] will be employed to ensure accurate measurement of the photocurrent as it allows the extraction of the photocurrent signal even when the dark current is up to 4 orders of magnitude larger than the photocurrent. Figure 2.2.1 shows the setup of the photomultiplication measurement using phase sensitive detection. Laser, modulated at a frequency of 180 Hz by the mechanical chopper, and was focused onto the top optical window of the diode. The resultant AC photocurrent represented by a voltage drop across a resistor, R, was measured using the Stanford Research SR830 lock-in amplifier (LIA) to isolate all the DC leakage dark current. The reference frequency was supplied to the LIA. Here appropriate values of R need to be considered in each measurement to ensure a sufficiently large photovoltage signal (at least 1 μV) to be measured while also ensuring that most of the applied reverse bias voltage is still dropped across the diode. The incident laser power was adjusted to eliminate heating effect in the device and ensure the multiplication characteristic was independent of incident optical power. Devices with different sizes in each wafer were measured to ensure negligible injection profile contamination due to the laser light falling on the mesa edge and to ensure the reproducibility and uniformity in the breakdown behavior. Measurements with laser focused on the edge of the diodes were also performed to verify whether premature edge breakdown occurred.

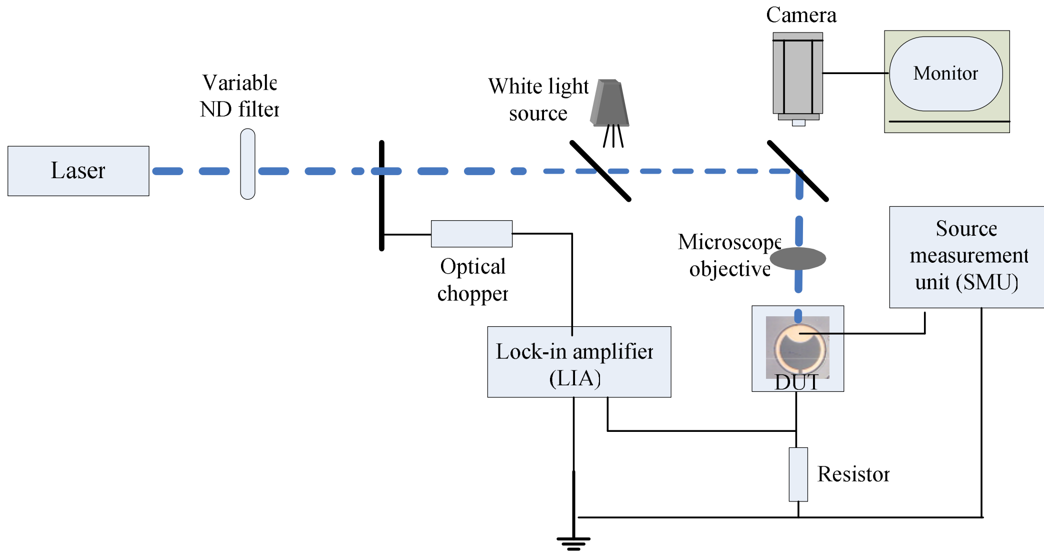

Figure 2.2.1 Schematic photomultiplication setup by phase-sensitive technique.

The multiplication factor is deduced by normalizing the photocurrent, I_{ph}, to the primary photocurrent, I_{pr}. Ideally, I_{pr} will not increase until the onset of multiplication in the diode. However as the depletion width widens with the reverse bias, the distance that photogenerated carriers have to diffuse to reach the edge of the depletion width reduces. Hence the increased the collection efficiency leads to an increase in I_{pr}. This increasing carrier collection efficiency of the photocurrent with bias was modeled by Woods *et al.* [17] by solving the current diffusion equation, and can be written as

$$I_{pr} = \frac{qG_0}{\cosh(L_0/L_{diff})} \tag{2.2.5}$$

where G_0 is the carrier generation rate at the cladding surface, L_{diff} is the minority carrier diffusion length in the undepleted cladding layer, L_0 is the distance between the illuminated surface and the edge of depletion region. If $L_{diff} >> L_0$ and the depletion width into the cladding layer is small but increases linearly with bias voltage (typically by 1% increasing between zero volts and the onset of multiplication), equation (2.2.5) can be approximately represented by a linear base line equation $I_{pr} = p_0V + q_0$ [18] where p_0 and q_0 are fitting parameters. In this thesis the cladding layers in the diodes are highly doped to ensure the depletion width did not increase significantly with bias voltage and

consequently the increase of primary current prior to onset of multiplication is small. I_{pr} can be corrected by this baseline correction, and multiplication is obtained by

$$M(V) = \frac{I_{ph}}{I_{pr}} = \frac{I(V)}{p_0 V + q_0} \qquad (2.2.5)$$

The low temperature photomultiplication measurements are similar to the room temperature measurements except the diodes are loaded into a Janis liquid continuous flow probe station, which allows temperature measurement ranging from 77 to 450 K. The Janis probe station has two DC probe arms, a multimode optical fiber with a core size of 65 μm and a probe arm with the high speed ground-signal-ground (GSG) probe. The measurements were performed under vacuum condition to avoid condensation on the diodes. The temperature of the chamber was monitored by a temperature controller which has a heater to heat the sample chamber to a desired temperature. Diodes with optical window bigger than 65 μm were selected for measurements to assure pure electron/hole injection

2.2.4 Excess noise measurement

2.2.4.1 Noise Figure Meter

When the photocurrent is significantly stronger than the dark current the excess noise measurement was performed using an Agilent (8970A) Noise Figure Analyser (NFA). Before the measurement, a system calibration was first performed to eliminate the noise from the setup. A reference noise source was connected to the NFA using a high speed cable, and the NFA measured the noise values tabulated on the reference noise source at a range of frequency, which indicates the success of the system calibration. The calibration process is illustrated in figure 2.2.2.

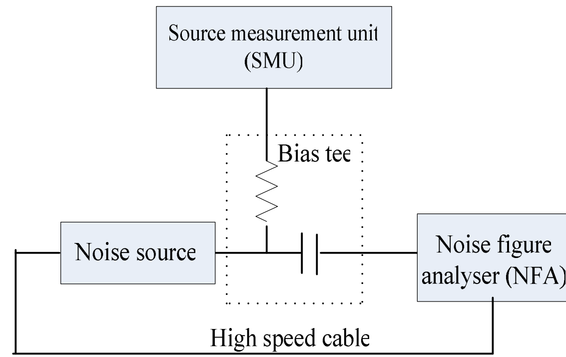

Figure 2.2.2 Schematic calibration process using noise source.

After the calibration process, the noise source was disconnected and the high speed cable was connected to the device under test (DUT) which was biased using an SMU through a bias tee. Laser was illuminated onto the device active area using an optical fiber as shown in figure 2.2.3. The device was fabricated into hybrid coplanar structure to be compatible with the microwave probe and to minimise interference from unwanted external noise sources.

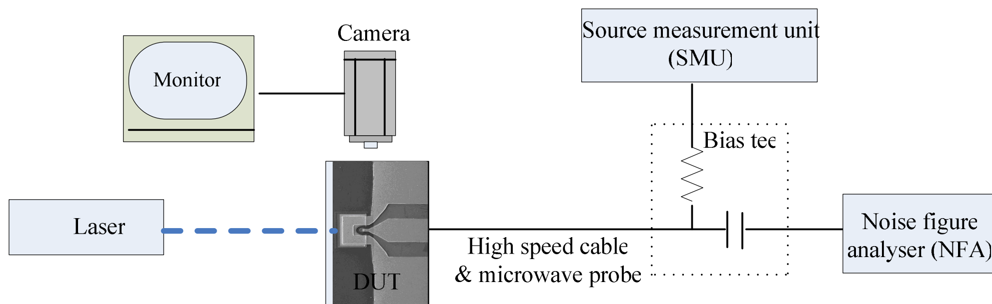

Figure 2.2.3 Schematic diagram of noise measurement system using NFA.

The noise signal in the above measurement setup includes the shot noise due to primary photocurrent of the device, the excess noise generated by impact ionisation and the system and background noise. The shot noise power due to primary photocurrent is given by $i_n^2 = 2qI_{pr}B$, where B is the system bandwidth. The associated noise power accounting for the multiplication process is given by $i_n^2 = 2qi_{pr}M^2BF$.

The NFA has a bandwidth of 4 MHz and measure the noise power across an internal 50 Ω resistor before displaying the noise power per unit bandwidth in dB relative to a reference noise power kT_0 (the Johnson noise for a matched 50 Ω input at T_0) [18]. T_0 is taken as 290 K.

$$NFM(dB) = 10\log_{10}(\frac{N}{kT_0}) \quad (2.2.6)$$

where N is the measured noise power over the bandwidth. Rearranging equation (2.2.6) gives

$$N = kT_0 10^{(\frac{NFM}{10})} \quad (2.2.7)$$

However, the system and background noise contributing to the noise floor in the NFA needs to be considered and subtracted from the total measured noise power to provide a correct noise power, N_c. The measured system and background noise, $N_{backgournd}$, can be achieved by measuring the noise at a bias just before the onset of multiplication. For a SAM APD, $N_{backgournd}$ is measured before the punch through voltage. The excess noise factor, F, therefore is given by

$$F = \frac{N_c}{2qI_{pr}M^2} \quad (2.2.8)$$

2.2.4.2 Phase sensitive detection technique

The conventional noise measurement system employing a noise figure analyser is unable to isolate the noise due to the dark current from that due to the avalanche process when the dark current is comparable to the photocurrent. Therefore to ensure accurate measurement of avalanche noise, a customised circuit developed by Li *et al.* [19, 20] using the phase sensitive detection technique was used. This allows simultaneous measurements of gain and excess noise of the devices. This setup includes two Standard Research SR830 lock-in amplifiers (LIAs). The excess noise circuit setup is shown in figure 2.2.4. Laser light was mechanically chopped and the modulated photocurrent was converted into a voltage signal and amplified by a transimpedance amplifier (TIA) with a gain of 2200 V/A. The amplified signal was measured using a LIA to determine the photocurrent and thus gain as described in the previous section. To measure the noise

power, the output from the TIA was connected to a bandpass filtered at a center frequency of 10 MHz and a bandwidth of 4.2 MHz to isolate the amplified shot-noise from the modulated signal. The noise voltage from the output of the bandpass filter was further amplified and converted to a mean square value by a power meter, which was measured using the second LIA. An attenuator placed between the amplifier and the noise power meter was used to avoid the power meter saturation by large signal.

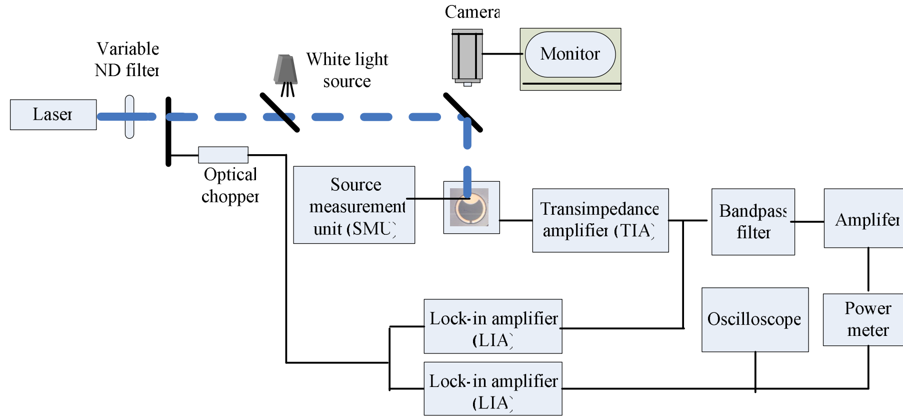

Figure 2.2.4 Schematic diagram of excess noise circuit set up.

Because the frequency response, defined by the transfer function of the TIA, of the measurement circuit is dependent on the device capacitance, the measured noise power needs to be corrected before the noise power can be deduced [20]. The variation of circuit gain with capacitance can be represented by the effective noise bandwidth [21]

$$B(C) = 4186335.43 + 81721.73C - 425.3267C^2 \tag{2.2.9}$$

where C is the device capacitance in pF.

The corrected noise power can be expressed as

$$N_c = N_m \times \frac{B(C_{Si})}{B(C)} \tag{2.2.10}$$

where N_m and N_c is the measured and corrected noise power, C_{Si} is the capacitance of the reference commercial Si p-i-n photodiode (Centronic BPX65) and $B(C_{Si})$ is the effective bandwidth of the Si photodiode.

The excess noise factor is given by

$$F = \frac{N_c}{KI_{pr}M^2} \tag{2.2.11}$$

where K is the noise per unit input photocurrent of the noise measurement system.

2.2.5 Frequency response measurement

2.2.5.1 Optical heterodyne technique

The wide band on-wafer frequency response measurements can be performed by using an optical heterodyne setup, as shown in figure 2.2.5.

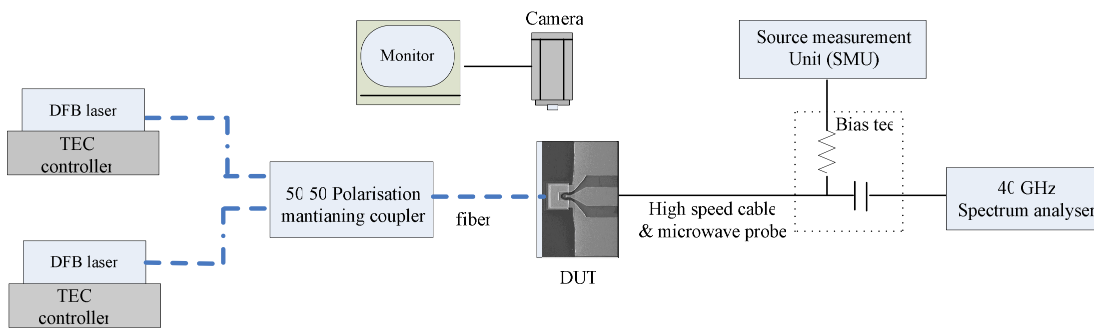

Figure 2.2.5 Schematic diagram of optical heterodyne setup.

The optical sources were provided by two Avanex A1935 TLI distributed feedback laser (DFB) laser diodes with the wavelengths of 1529.55 nm and 1570.82 nm, respectively at room temperature. One laser diode was mounted on the Melles Griot DTC301 temperature controller and the other one was mounted on Thorlabs ITC4001 to be controlled by a computer. The wavelength of the laser light is temperature dependent, and hence, the output wavelength of the laser diode can be modified by the temperature controller by using the Peltier effect. The laser diodes available have temperature wavelength tunability of 0.09 nm/ºC and the temperature tuning resolution of the ITC4001 temperature controller is about 0.001 ºC. By tuning the temperature of the laser diode mounted on the Thorlabs temperature controller and keeping the other one constant, the two lasers were mixed using a 50:50 polarisation maintaining coupler. This setup is capable of generating a signal with oscillation frequency that is close to THz. The beat frequency of the signal is expressed as

$$\omega_b = \frac{2\pi}{c \cdot (1/\lambda_1(T_1) - 1/\lambda_2(T_2))} \tag{2.2.12}$$

where $\lambda_1 (T_1)$ and $\lambda_2 (T_2)$ are the temperature dependence of wavelengths of the first and second DFB laser diodes that are fixed at temperature T_1 and T_2 respectively; ω_b is the frequency difference between the two laser diodes (beat frequency). From calculation, a temperature step of 0.001 ºC (corresponding to ~ 0.0001nm), can produce a minimum beat frequency step of ~ 12 MHz.

The combined optical intensity of the mixed light waves is given by [22, 23]

$$\Psi(t) = \zeta_1^2 + \zeta_2^2 + 2\cos\varphi \cdot \zeta_1 \cdot \zeta_2 \cdot \cos(\omega_b t) \tag{2.2.13}$$

where ζ_1 and ζ_2 is the optical field envelope of the first and second DFB laser diodes, φ is the angle between the two polarised directions of the light waves. The polarisation angle should be kept at the values of $2k\pi$ for maximum optical signal intensity; otherwise, any small variation in the polarisation angle would result in a big change in the optical signal. As the polarisation of light can be influenced by small temperature variation and pressure points on the optical fiber, a Thorlabs manual polarisation controller was inserted between one of the output fibers of the 50:50 couplers and the device to minimise φ. The device was probed using a microwave probe from GGB Industry Inc.(40 A, 8 kHz ~ 40 GHz) and then connected to a SMU and Anritsu spectrum analyser (MS2688C, 9 kHz ~ 40 GHz) through a bias tee from Picosecond Pulse Labs (5544, 50 kHz ~ 40 GHz).

Thus, the photocurrent response from the device is given by [22, 23]

$$i_c(t) = \frac{q\eta_0}{h\nu}(\zeta_1^2 + \zeta_2^2 + F(\omega_b)\cos\varphi \cdot 2\zeta_1\zeta_2\cos(\omega_b t)) \tag{2.2.14}$$

where η_0 is the quantum efficiency of the device, $h\nu$ is the photon energy and $F(\omega_b)$ is the frequency response of the diode. As the optical signal intensity was adjusted for photodiode to deliver adequate signal level to overcome system noise, and the ζ_1, ζ_2 and the polarisation angles were kept constant during measurements, the frequency response of the diode at a given beat frequency can be detected by the spectrum analyser. Figures 2.2.6 (a) and (b) show an example of the frequency response of a diode at the beat frequency of 4.2 GHz and full frequency response of InGaAs/InAlAs verticaly

illuminated APDs with different diameters measured by the heterodyne setup, respectively. The absolute power (in dBm) measured by the spectrum analyser can be easily used to define the -3 dB bandwidth of the DUT.

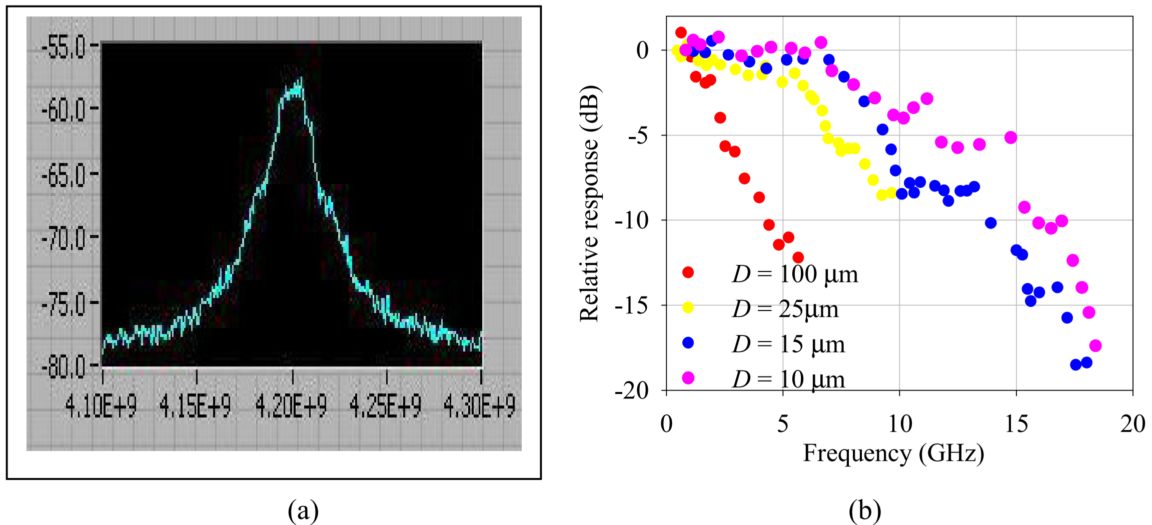

(a) (b)

Figure 2.2.6 (a) an example of the frequency response of a diode at the beat frequency of 4.2 GHz and (b) full frequency response of InGaAs/InAlAs vertically illuminated APDs with different diameters measured by heterodyne setup.

2.2.5.2 External laser modulation

Optical heterodyne measurements can provide the advantage for ultra-wide bandwidth characterisation. However it delivers the DC and AC optical signals together and this could affect the bandwidth measurement since the response of the diode can be influenced by the DC optical power level. In order to overcome the system noise and detect the beat frequency from the photodiode, high optical power illumination was used with an unwanted consequence of increased total current in the diode leading to potential saturation effect, particularly for APD operating at high gains.

Therefore the setup that can generate separate DC and AC signals is desirable. Externally modulated continuous wavelength (CW) laser diode was utilised, as illustrated in figure 2.2.7. A Thorlabs Fabry-Perot (FP) laser diode with a continuous output wavelength of 1330 nm was connected to a variable optical attenuator for controlling the power intensity before modulated by a CIP Technologies 40 GHz electron-absorption modulator (EAM).

The EAM was driven by an Agilent network analyser (E83641 10 MHz ~ 50 GHz) which has a wide RF signal power ranging from -70 ~ +13 dBm. The modulated optical signal though optical fiber was transmitted into the DUT and the optical-electron frequency response was detected by the other port of the network analyser.

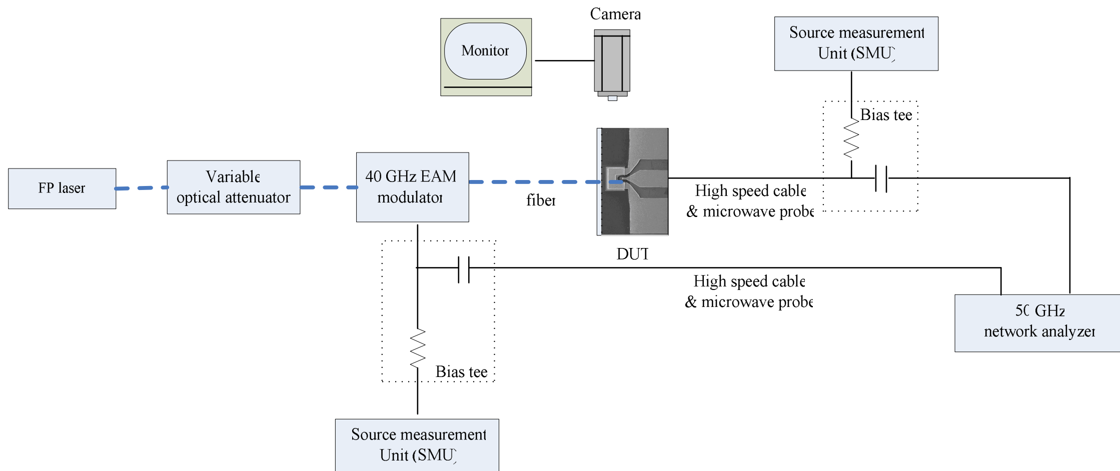

Figure 2.2.7 Schematic diagram of externally modulated laser setup.

It is worth noting that both systems described suffer system loss when signal propagates at high frequency through the RF components (the cable, probe, bias tee, modulator and adapters all have -3 dB bandwidths of 40 GHz). Hence any measured frequency response data have to be corrected for this system loss. The system loss from the RF components, excluding the 40 GHz GSG probe and the modulator, was measured by the network analyser. The loss from the probe and modulator was extracted from their data sheet and were added into the total system loss for system calibration. Figure 2.2.8 shows the total system loss with the RF modulating power ranging from -60 to +4 dBm.

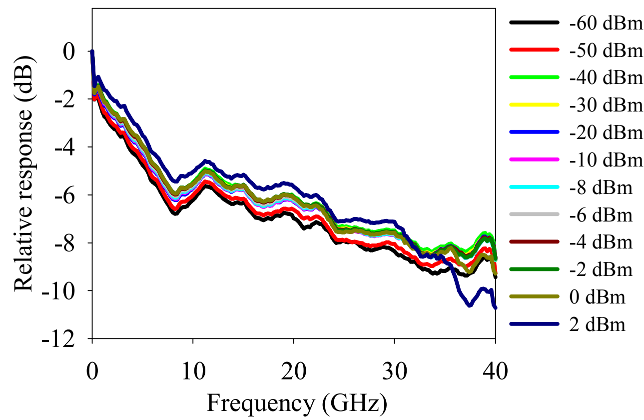

Figure 2.2.8 Total system loss from all the RF components.

In addition, in the above two measurement techniques, the measurement platform that accommodates both electrical and optical signal at high frequency requiring the satisfactory of ease of use and stability for top-illuminated and side illuminated photodiode characterisations. The standard 50 Ω GSG microwave probe is therefore installed on the custom arms attached to precision linear translation stages with micrometer adjustment. The planarisation of the probe station and probe arm can be rotated by a screw and lock, as shown in figure 2.2.9.

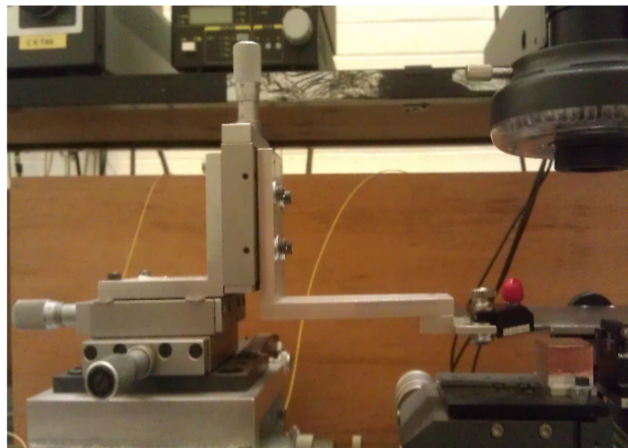

Figure 2.2.9 Probe station for the microwave measurement.

The optical fiber transmitted the laser light can be precisely positioned on the top optical window for the top-illuminated devices by micrometer adjustment stage, both of which images can be simultaneously presented by the camera and monitor through the optics.

The side illuminated device deliveries the light to in-plane surface and the facet of the waveguide is generally every small (< 10 μm), requiring a high precision control for optical coupling. The lensed fiber with small beam size waist (~ 3 μm) was used to focus the light onto the DUT. This fiber was mounted on a Melles Griot three-axis linear translation state with manual micrometer actuator. The translation stage parallel and perpendicular to the beam propagation was controlled by a mounted DC servo actuator for submicron resolution adjustment, which was necessary for the short depth of field of focusing lens. This side illumination platform was used for waveguide measurements, as shown in figure 2.2.10. The detail information of the high speed measurement by the two setups is also described in Appendix C.

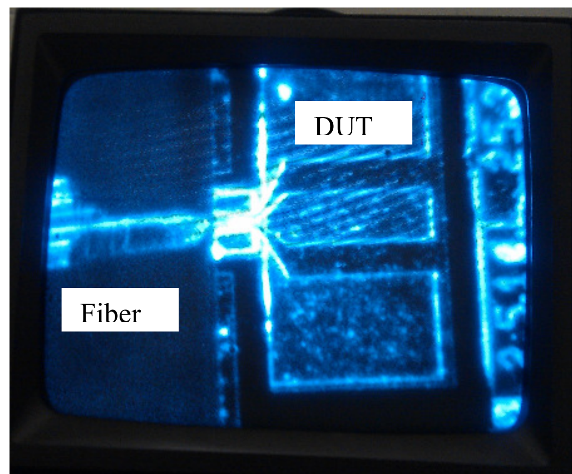

Figure 2.2.10 Side illumination measurements for the waveguide devices under test.

2.3 Reference

[1] Y. J. Chiu, "Sub-terahertz travelling-wave low temperature grown GaAs p-i-n photodetector," in *ECE. Doctor of Philosophy*: The University of California, Santa Barbara, 1999.

[2] S. Zhang, "Travelling-wave electroabsorption modulators," in *ECE. Doctor of Philosophy*: The University of California, Santa Barbara, 1999.

[3] Texline software, Microwave simulation instruments.

[4] K. S. Giboney, M. J. W. Rodwell, and J. E. Bowers, "Travelling-wave photodetector design and measurements," *IEEE J. Selected Topics in Quantum Electron.* , vol. 2, pp. 622-629, 1996.

[5] K. S. Giboney, "Travelling-wave photodetectors," University of California, Santa Barbara, CA, *Ph.D. Dissertation*, 1995.

[6] K. S. Giboney, R. L. Nagarajan, T. E. Reynolds, S. T. Allen, R. P. Mirin, M. J. W. Rodwell, and J. E. Bowers, "Travelling-wave photodetectors with 172-GHz bandwidth and 76-GHz bandwidth-efficiency product," *IEEE Photonics Technol. Lett.,* vol. 7, pp. 412-414, 1995.

[7] K. S. Giboney, J. W. Rodwell, and J. E. Bowers, "Travelling-wave photodetector theory," *IEEE Trans. Microw. Theory Tech.,* vol. 45, pp. 1310-1319, 1997.

[8] D. Jager, "Slow-wave propagation along variable Schottky-contact microstrip line (SCML)," IEEE Trans. Microw. Theory Tech. , vol. MTT-24, pp. 566-573, 1976.

[9] K. S. Giboney, "Travelling-wave photodetectors," University of California, Santa Barbara, CA, *Ph.D. Dissertation*, 1995.

[10] R. Ludwig and P. Bretchko, RF circuit design: theory and application, US.

[11] J.-W. Shi, K. G. Gan, Y. J. Chiu, Y.-H. Chen, C.-K. Sun, Y. J. Yang, and J. E. Bowers, "Metal-semiconductor-metal travelling-wave-photodetectors," *IEEE Photon. Technol. Lett.*, vol. 13, pp. 623–625, 2001.

[12] LineCalc, distributed by Hewlett Packard Company, Westlake Village, CA, 1996.

[13] R. N. Simons, *Coplanar waveguide circuits, components, and systems*. Ohio: NASA Glenn Research Centre, pp.12-18, 2001.

[14] Y. J. Chiu, S. B. Fleischer and J. E. Bowers, "High speed and low-temperature grown GaAs p-i-n travelling-wave photodector," *IEEE Photon. Technol. Lett.*, vol. 10, pp. 1012-1014, 1998.

[15] S. M. Sze, Physics of Semiconductor Devices, 2nd Ed. John Wiley and Sons, 1981.

[16] C. H. Tan, "Measurements of excess avalanche noise in sub-micron Si and Al0.8Ga0.2As avalanche photodiodes," in *EEE. Doctor of Philosophy*: The University of Sheffield, 2002.

[17] M. H. Woods, W. C. Johnson, and M. A. Lampert, “Use of a schottky barrier to measure impact ionisation coefficients in semiconductors”, *Solid State Electron.*, vol. 16, no. 3, pp381-394, Mar. 1973.

[18] L. J. J. Tan, "Telecommunication wavelength InP based avalanche photodiode," *Ph.D thesis*, The University of Sheffield, 2008

[19] K. S. Lau, C. H. Tan, B. K. Ng, K. F. Li, R. C. Tozer, J. P. R. David, and G. J. Rees, “Excess noise measurement in avalanche photodiodes using a transimpedance amplifier front-end,” *Meas. Sci. Technol.*, vol.17, pp. 1941–1946, 2006.

[20] K. F. Li, D. S. Ong, J. P. R. David, G. J. Rees, R. C. Tozer, P. N. Robson, and R. Grey,"Avalanche multiplication noise characteristics in thin GaAs p^+-i-n^+ diodes", *IEEE Trans. Electron Dev.*, vol. 45, no. 10, pp. 2102-2107, 1998.

[21] Y.L.Goh, “Impact ionisation in InGaAs, InAlAs and InGaAs/GaAsSb superlattices for near infrared avalanche photodetectors” *Ph.D thesis*, University of Sheffield, 2008.

[22] M. C. Teich, "Infrared heterodyne detection," *Proceedings of the IEEE,* vol. 56, pp. 37-46, 1968.

[23] S. Kawanishi, A. Takada, and M. Saruwatari, "Wide-band Frequency- Response Measurement of Optical Receiver Using Optical Heterodyne Detection," *Journal of lightwave tech.,* vol. 7, January 1989.

Chapter 3 Fabrication techniques

This chapter summarises the selective chemical mesa etching and surface treatment of InGaAs/AlAsSb SAM APD for electrical characterisation and reliable performance. The fabrication process of InGaAs/InAlAs high speed diode with hybrid CPW structure for electrical and microwave characterisation is also outlined. The InGaAs/AlAsSb and InGaAs/InAlAs APDs were grown by molecular beam epitaxy (MBE) by IQE InC., US, and EPSRC National Centre for III-V Technologies, U.K respectively. All the devices were fabricated at the clean room at the EPSRC National Centre for III-V Technologies, U.K.

3. 1 Molecular beam epitaxy (MBE)

Molecular beam epitaxy (MBE) is a evaporation technique developed by A.Y.Cho in the 1970's [1-3] that take place in ultra-high vacuum ($\sim 10^{-8}$ Torr) and can precisely controls the beam fluxes and allows the films to grow eptitaxially. The slow deposition rate (≤ 1 μm/hr) and the shuttered sources allow the accurate control of material composition at the atom level and doping in the sharp hetero-junction interface. The system overview is shown in figure 3.1.1. Wafers are loaded in the high-vacuum growth chamber and placed on the continual azimuthal rotation (CAR) on which the wafer are heated and rotated during the cystal growth. The beam equivalent pressure (BEP) is positioned facing the sourcing. The reflection high energy electron diffraction (RHEED) is often used for monitoring the growth of the crystal layers. A thermocouple on the CAR heater along with the optical pyrometry is used to control the growth temperature. The shutters are controlled by the computer which control the fluxes from the sources during the growth [4]. Cryopumps and cryopanels is used to cool and maintain the growth chamber temperature.

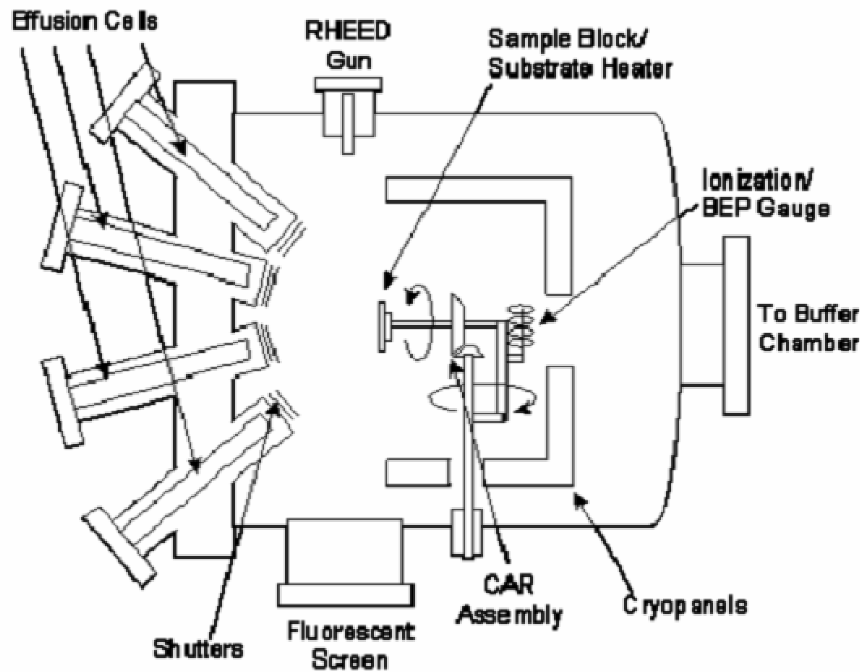

Figure 3.1.1 Schematic of MBE chamber (copied from Ref.3)

3.2 Simple mesa diode

Simple mesa diodes were fabricated into microstrip structure to test wafer quality and used for electrical characterisations such as I-V, C-V, photomultiplication and excess noise measurements. First, the samples were cleaned by boiling in the n-butyl acetate, acetone and isopropyl alcohol (IPA) for 30 seconds. Following this the mesa pattern was defined by the standard photolithography process and chemically etched to isolate the p- and n-type contact layers as well as providing isolation between adjacent devices. The chemical etch should be carefully chosen to achieve a high selective etch so that the semiconductor is etched at a significantly faster rate than the photoresist as well as ensuring minimum undercut and damage to the sample surface. A 1: 8: 80 mixture of sulphuric acid: hydrogen peroxide: deionised water (H_2SO_4: H_2O_2: DIW) has been reported to etch InGaAs and InAlAs at room temperature with a stable etch rate of ~ 0.5 μm/min [5], and hence was used for etching InGaAs/InAlAs material system in this work. A 1:1:1 mixture of hydrobromic acid: acetic acid: potassium dichromate solution (HBr:

CH_3COOH: $K_2Cr_2O_3$) was found to yield good I-V characteristics at room temperature for AlAsSb p-i-n photodiodes [6]. However the 1:1:1 mixture of HBr: CH_3COOH: $K_2Cr_2O_3$ etchant will generate a significant trench at the bottom floor of the mesa and produce sharp edges due to the change of mesa slopes at the heterojunctions. This can cause high electric field in the devices leading to potential premature breakdown. The deep trench penetrating into the substrate can also cause an open-circuit if the structure is grown on semi-insulating substrate. Hence a more reliable chemical etchant recipe is required for InGaAs/AlAsSb SAM APD as it is grown on the semi-insulating substrate. The etching of InGaAs /AlAsSb structure was evaluated using the following recipes:

a) 1:1:1:10 HBr: CH_3COOH: $K_2Cr_2O_3$: DIW – etches all the layers in the InGaAs/AlAsSb APD

This diluted etchant was aimed at minimising the trench. However the reduced trenches were achieved with a slow etching rate (~ 20 nm/min) which produces a rough surface with visible black spots, as shown in figure 3.2.1 (a).

b) 1:8:80 H_2SO_4: H_2O_2: DIW – etches all the layers in the InGaAs/AlAsSb APD

This etchant produced poor I-V performance and a matt surface as reported for AlAsSb p-i-n photodiodes [2]. After etching rough and dark spots were produced in the surface although the trenches were insignificant, as shown in figure 3.2.1 (b).

c) 1:8:80 H_2SO_4: H_2O_2: DIW – etches InGaAs absorption layer and InAlAs charge sheet layer, followed by

1: 1: 9 – HCL: H_2O2: DIW – selective etching for AlAsSb

1:1:9 HCL: H_2O_2: DIW has been reported provide a selective etching for AlAsSb without attacking InGaAs [7]. Therefore a 1:8:80 H_2SO_4: H_2O_2: DIW was first used to remove the InGaAs absorption layer and InAlAs charge sheet layer, and followed by 1:1:9 HCL: H_2O_2: DIW to etch away the AlAsSb layers. Unfortunately after etching dark surface and visible cracks were produced. These could not be removed when the sample was exposed to the air. Insignificant trench was observed after completing the etching process. The results are shown in figure 3.2.1 (c).

d) 1:8:80 H_2SO_4 : H_2O_2: DIW – etches the InGaAs absorption layer and InAlAs charge sheet layer, followed by

1: 1: 5 - HCL: H_2O_2: DIW – selective etching for AlAsSb

In order to increase the etch rate for AlAsSb layer and reduce the possibility of Al and Sb oxidation, the concentration of HCL: H_2O_2: DIW etchant was increased to a ratio of 1:1:5. The etched sample showed an even and clean surface, suggesting minimal Al and Sb oxidation, as shown in figure 3.2.1 (d). No significant trench was observed after the etching process, improving the device reliability for subsequent electrical characterisation. The sample was finally dipped into 1:1:1 HBr: CH_3COOH: $K_2Cr_2O_3$ etchant to produce good I-V characteristic for AlAsSb as reported.

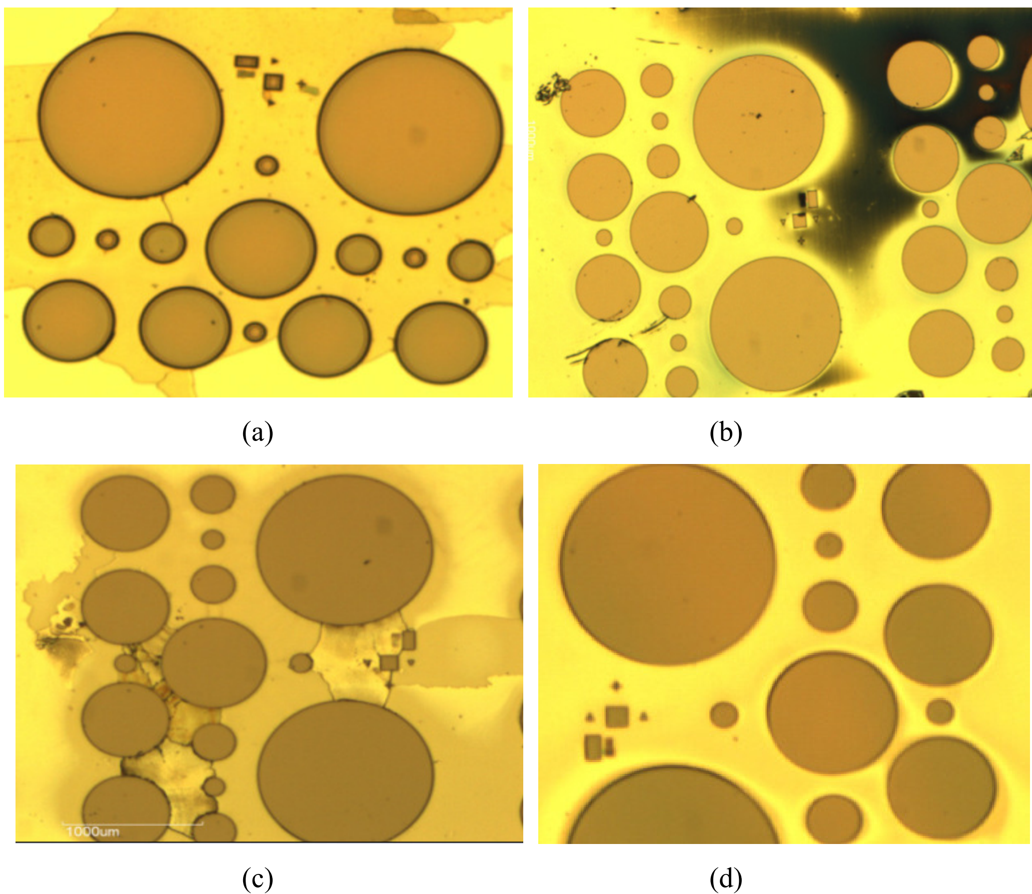

Figure 3.2.1 Microscope view of sample surface after different recipes: (a) 1:1:1:10 HBr: CH_3COOH: $K_2Cr_2O_3$: DIW; (b) 1:8:80 H_2SO_4: H_2O_2: DIW; (c) 1:8:80 H_2SO_4: H_2O_2: DIW + 1: 1: 9 – HCL: H_2O_2: DIW and (d) 1:8:80 H_2SO_4: H_2O_2: DIW +1:1:5 - HCL: H_2O_2: DIW.

Since the wafer was grown on semi-insulating substrate, the metal grid contacts are evaporated on the bottom n-layer after the mesa etching; the n-backside metal contacts can be evaporated for wafers grown on conducting substrates. It is worth noting that both

choices of p-type and n-type metallisation are crucial for achieving thermally stable and low contact resistance contacts. The annealing of the metal alloy to encourage metal diffusion into the semiconductor can improve the ohmic contacts.

Dielectric films are sometimes deposited for planarisation and for surface passivation to protect the device from ambient gases and moisture so that good electrical characteristics can be maintained. In this work, different dielectric films such as SiN_x, SiO_2, BCB and an alternative negative photoresist SU-8 have been deposited on InGaAs/AlAsSb SAM APDs. The best I-V characteristics were achieved using SU-8 as shown in figure 3.2.2, which is probably due to the absence of high temperature or plasma induced damages compared to the plasma enhanced chemical vapor deposition (PECVD at 300 °C) for Si_xN and SiO_2. Baking for BCB at high temperature to dehydrate (100 °C) and curing (250 ~ 300°C) may be the reason for the degradation observed.

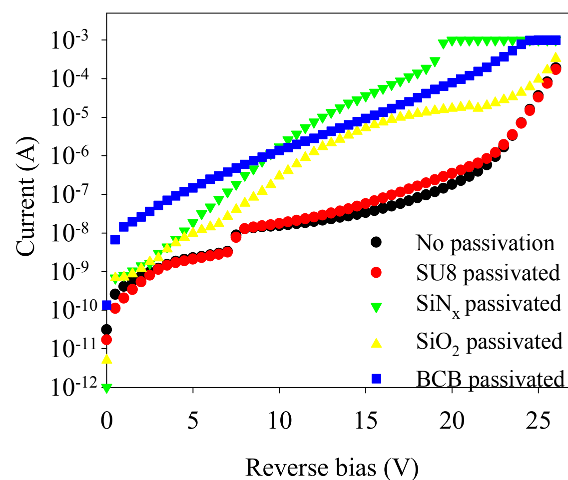

Figure 3.2.2 I-V characteristics for unpassivated and passivated InGaAs/AlAsSb SAM APDs with different dielectric films.

Finally, diodes were fabricated with the radius, r of 200, 100, 50 and 25 μm. The top view and cross-section of the fully fabricated devices are shown in figure 3.2.3 (a) and (b) respectively.

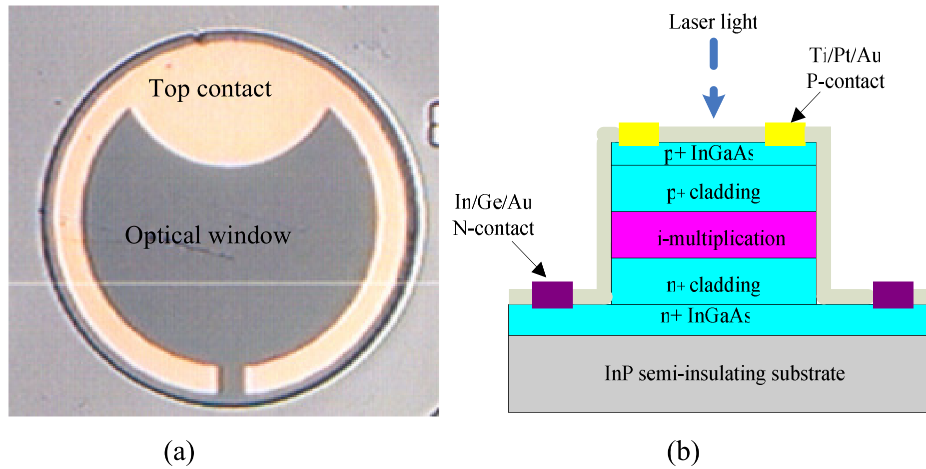

(a) (b)

Figure 3.2.3 (a) Top and (b) cross-section view of fabricated simple mesa diode.

3.3 High speed InGaAs/InAlAs APDs

The high speed InGaAs/InAlAs APD was fabricated using the hybrid coplanar structure and the processing was carried out using a self-alignment technique [8] on the semi-insulating substrate. Detail information of the process is described in Appendix D.

1) P-type top metallisation and annealing

It is well known that RC time limit is normally the main limit for the high speed device. Since the photodiode's capacitance is dominated by the diode's area, the material's permittivity and the depletion region, (these are fixed by the APD design) it is critical to achieve a p-type ohmic contact with low series resistance. In addition to a highly doped p-type InGaAs cap layer (generally $>10^{19}/cm^3$), the work function (φ_m) of the metal should be greater than InGaAs to form a narrow accumulation layer at the interface. The valence band edge of InGaAs lies 0.25 eV below the vacuum level (electron affinity energy) and 5.5 eV for GaAs, most metal work functions are below 5 eV, so it is difficult to find a good p-contact metal. Furthermore the surface state density in the p^+ InGaAs layer is reported high, resulting in the surface energy pinning effect [9] and hence it is challenging to obtain good ohmic contact on the p^+ InGaAs layer. A number of metallisation schemes were evaluated and a low contact resistance was obtained by thermal evaporation of Ti/Pt/Au with the thickness of 10 /30/200 nm followed by a rapid thermal annealing at 420 °C for 30 seconds [10]. Here Ti (φ_m = 4.33 eV) was used to form a good adhesion to the semiconductor, Pt used since it has a high work (φ_m = 5.65

eV) [11] and Au deposited to package and overcome the skin effect at high frequency. The metal contacts were annealed to allow Pt to migrate to the semiconductor interface to form alloys of metal-semiconductor. The top annual contact was formed on top-illuminated device to allow optical access while the top contact along the mesa ridge was evaporated for side illumination device to minimise the series resistance.

2) Mesa etch

Mesa patterns were defined using a standard photolithography, and the pre-deposited p-metal contacts were used as self-aligned metallisation with respect to the mesa regions. During the mesa etching, the etch profile produced by the dry etching is normally vertical, which could cause either a discontinuity of metal tracks for bond pads or high electric field at the corner mesa edge, so that a gradual slope etch profile is preferred at the sidewall. Since some wet chemicals etch anisotropically due to preferential etching along certain crystal planes, the etch profile produced using H_2SO_4: H_2O_2: DIW (1:8:80) was investigated for InGaAs/InAlAs APDs. Since the preferential etching is not prominent in the circular diodes, square pixels shown in figure 3.3.1 (a) were used to investigate the etching profile for InGaAs/InAlAs APDs. The straight edge of square pixel was oriented in parallel to the $[01\vec{1}]$ and to the $[011]$ direction of the grown wafer, which were indicated by the major flat and secondary flat on the grown wafer. The gradual slope which enables a smooth transition from the top metal contact to the bottom n^+ layer was achieved in the $[01\vec{1}]$ direction, as shown in figure 3.3.1 (b). The undercut widths, in the two directions were different, which was commonly observed in the wet chemical etching. In order to avoid the metal contacts from overhanging (due to undercut) over the edge of the mesa and causing potential short circuit, it was particularly important that the mask set was designed to account for this undercutting effect. Examples of devices with small areas are the waveguide devices [8] with dimensions of less than 10 ×10 μm^2, and the thin ridges mandatory for travelling wave APDs. The square pixel with side length of 15 μm oriented parallel to the $[011]$ and to the $[01\vec{1}]$ direction was again patterned and etched using H_2SO_4: H_2O_2: DIW (1:8:80) with an etch depth of 1.7 μm. The side lengths of the square pixel on the top p^+ layer were found to be ~ 3.7 and ~ 3.9 μm in the $[011]$

and $[01\bar{1}]$ direction respectively. There was no significant undercut at the bottom n^+ layer in the $[011]$ direction but ~ 2 μm undercut, or lateral etch, was produced in the $[01\bar{1}]$ direction. The etched profiles in the two directions were shown in figures 3.2.2 (a) and (b) respectively. Figure 3.3.3 shows the fabricated metal tracks along the mesa sidewall in the $[011]$ and $[01\bar{1}]$ directions of the wafer. An acceptable bevel sidewall and high yield continuous metal track was formed parallel to the $[01\bar{1}]$ direction.

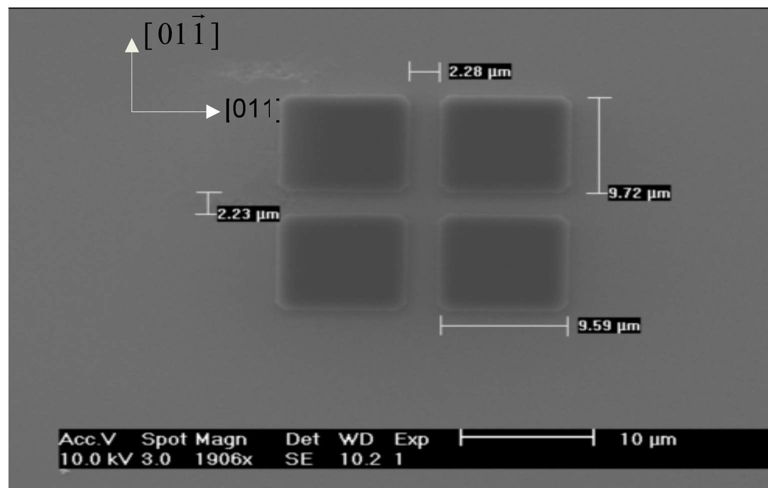

(a)

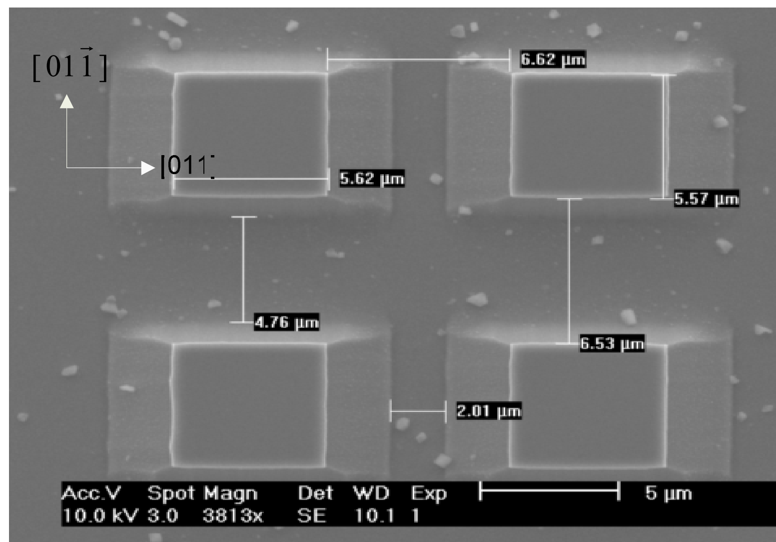

(b)

Figure 3.3.1 SEM of (a) square pixel and (b) etch profiles of 4 x 4 square pixels on InGaAs/InAlAs APD. The pixel edges were oriented in parallel to the $[011]$ and to the $[01\bar{1}]$ directions of the grown wafer.

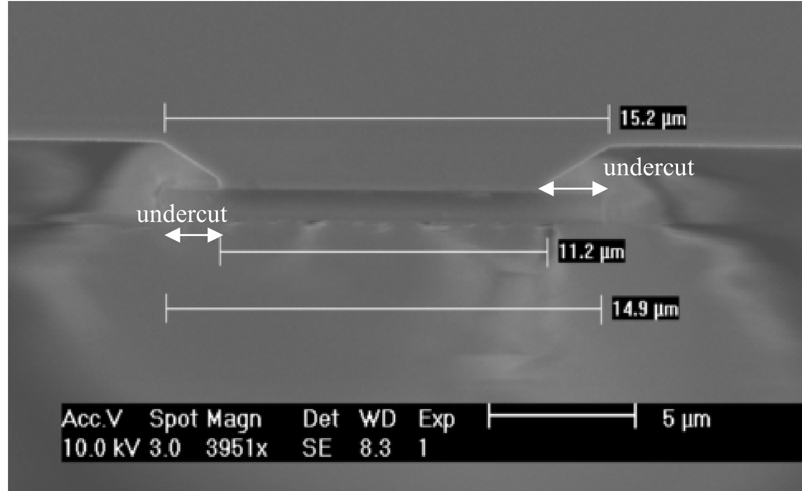

(a)

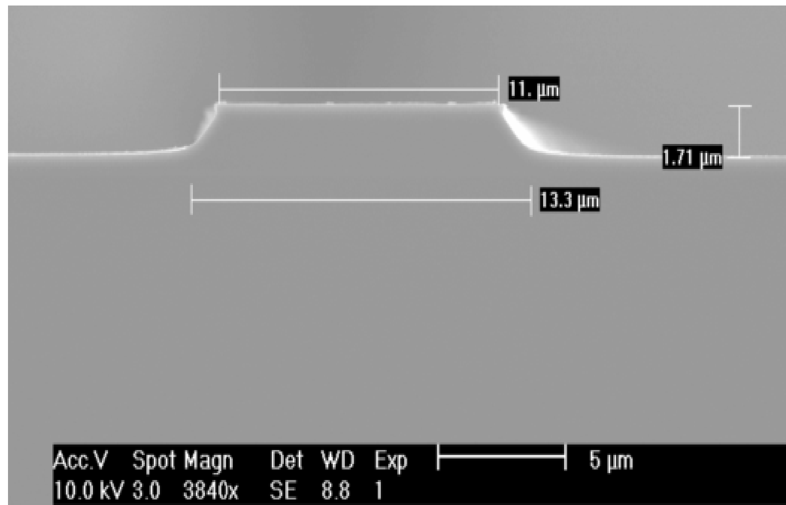

(b)

Figure 3.3.2 SEM of InGaAs/InAlAs APD etch profiles in directions of (a) $[011]$ and (b) $[01\vec{1}]$ directions of the grown wafer with the etch depth of 1.7 μm. An undercut was observed in (a).

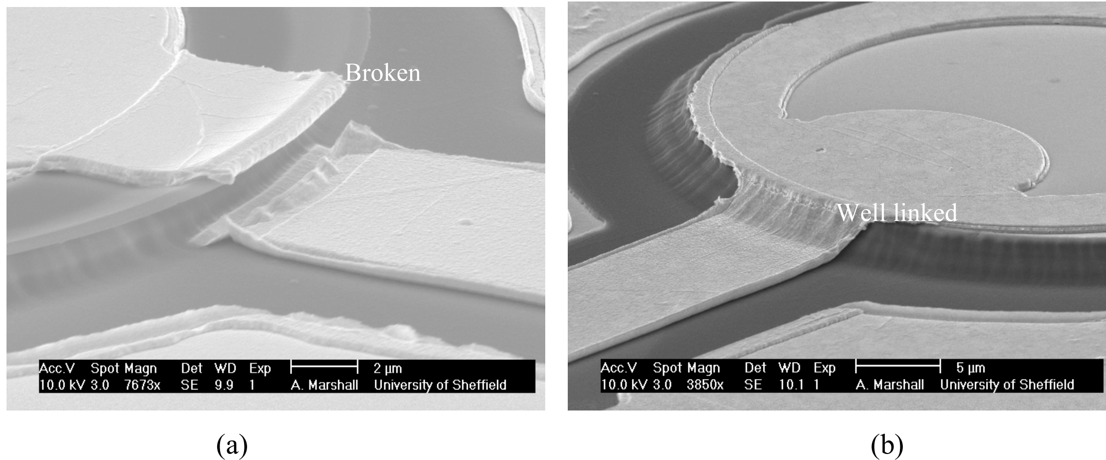

(a) (b)

Figure 3.3.3 SEM of the metal track transition from the top p^+ of the mesa to the n^+ bottom layer in directions of (a) $[011]$ and (b) $[01\vec{1}]$ of the grown InGaAs/InAlAs wafer.

The top-illuminated devices were fabricated into circular with different diameters and rectangle for side illuminated devices with different ridge widths and lengths.

3) N-type metallisation

InGe/Au with the thickness of 20/200 nm was thermal evaporated to form the lower n-type ohmic contact. Though the metal contact rapid thermal annealing at 420 °C for 3 s can improve the contact resistance [12], the high temperature exposure of mesa sidewall may degrade the device surface leakage characteristic. The subsequent process by PECVD (300 °C) for dielectric layer deposition requiring further heating can help the metal diffusion into the n^+ InGaAs cladding layer, so that the metal alloying process was suspended and carried out together with the dielectric layer deposition process.

4) Second mesa etch

The second mesa etch was carried out to etch the structure to the semi-insulating substrate for microwave probing and minimising the parasitic capacitance between bond pads. A mixture of H_2SO_4: H_2O_2: DIW (1:8:80) was used to remove the bottom n^+ InGaAs contact layer. Diluted HCL solution [11] can selective etch InP without InGaAs/InAlAs but it has a fast etch rate of 12 µm/min. Therefore, Orthophosphoric acid, H_3PO_4, and DIW was added to HCL with a mixture ratio of 3:1:2 for better control of the etch rate, which is 3 µm/min. There should be negligible surface leakage current flowing

through the ideal semi-insulating substrate, however, the un-optimised substrate by defects or the dopants from the n^+ InGaAs contact layer diffusing into the substrate will result in substrate leakage current, as illustrated in figure 3.3.4(a). Therefore the etching thickness (d_1) to the substrate with different acid and etching time was investigated, shown in figure 3.2.4(b). The combination etchants of H_2SO_4: H_2O_2: DIW (with ratio of 1:8:80) and H_3PO_4: HCL: DIW (with ratio of 3:1:2) which etched the substrate for 10 s with the thickness of 0.5 µm, produced the worst surface leakage, indicating there is a possibility of dopants diffusing into substrate. Less surface leakage current is flowing through the substrate with the etching depth d_1 = 1 ~ 2 µm, however, the leakage current level of tens of nA requires further optimisation of the substrate. Figure 3.3.5 shows a successful metal link from the n^+ bottom contact layer to the substrate.

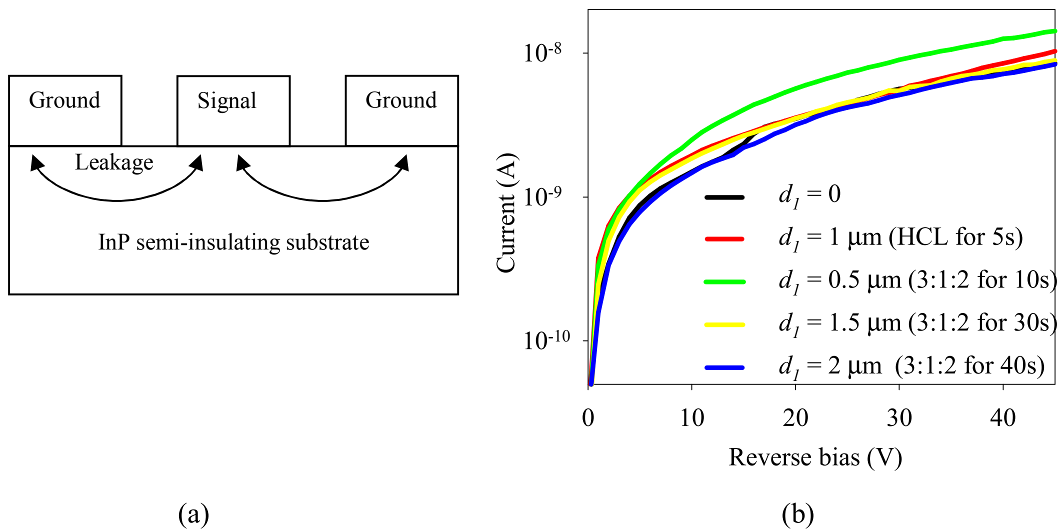

(a) (b)

Figure 3.3.4 (a) Schematic illustration the surface leakage current flowing through the bond pads; (b) measured surface leakage current with different etching depth for different acid and etching time.

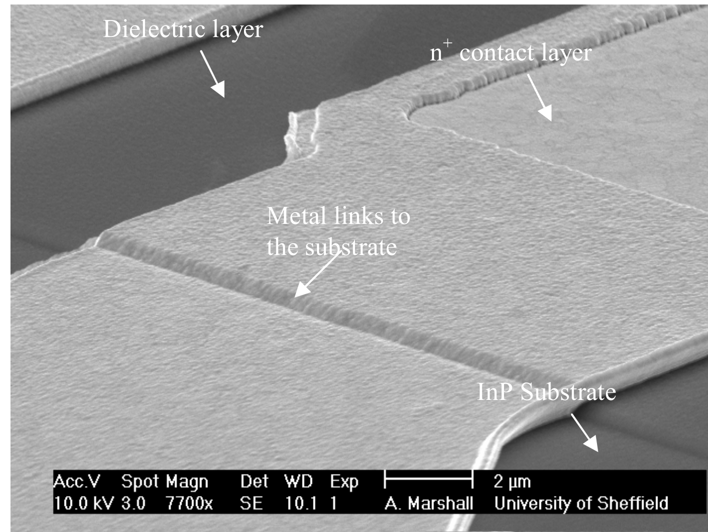

Figure 3.3.5 SEM of the bond pad links the bottom n^+ InGaAs contact layer to the InP semi-insulating substrate.

5) Dielectric layer deposition

Normally one of the difficulties associated with the fabrication of the high speed device is the optimised low leakage bond pads on the semi-insulating substrate. The dielectric isolation or the air-bridge techniques are possible ways to fabricate the bond pads [11]. In our fabrication procedure, 200 nm SiN_x dielectric film was deposited by PECVD process (300 °C), which was used as passivation and dielectric isolation layer. Then the contact windows of the p-top, n-bottom and bond pads were opened by reactive ion etching (RIE). The RIE etching time was calculated approximately from its etching rate (50 ~ 55 nm/min). It is worth noting that the reactive ion beam will attack the photoresist during the window opening process, the thickness of the photoresist needs to be adjusted accordingly, particularly spinning sufficient photoresist thickness at the sharp corner of device edges, where it is thinnest.

6) CPW contact pads

The CPW contact pads of connecting the top p-contact, low n-contact to the substrate was thermal evaporated using Ti/Au interconnect metal with the thickness of 10/600 nm. Ti was used as adhesion layer of Au to the semiconductor and the thickness Au layer was calculated to be sufficiently thick to overcome the skin effect depth at high frequency up

to 50 GHz. The fabrication of high speed top-illuminated device was completed after this process.

7) Scribe and cleave substrate

In order to allow lateral light injection for side illuminated waveguide device, the substrate thickness needs to be reduced to about 150 μm by chemical mechanical polishing process. The following scribing and cleaving process at the center of the ridge was to achieve a smooth facet for light coupling, as shown in figure 3.3.6. Here, the pairs of pre-deposited triangle metal with the gap width of 10 μm were used as cleaving alignment marks and their separation width shows the maximum cleaving tolerance if the breaking line was not straight.

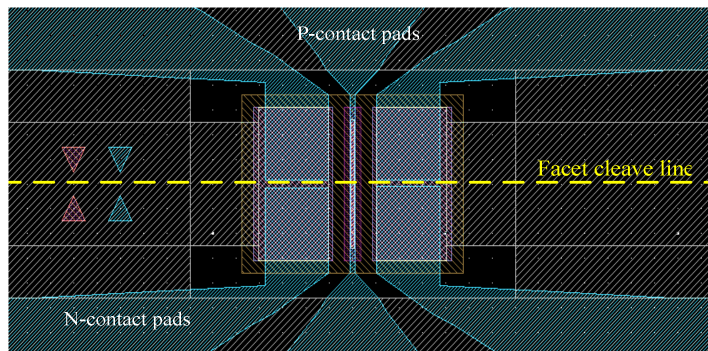

Figure 3.3.6 Scribe and cleave along the center of the ridge device, the dashed line is facet cleaving.

The top views of the fabricated high speed vertically illuminated and side illuminated device are shown in figure 3.3.7.

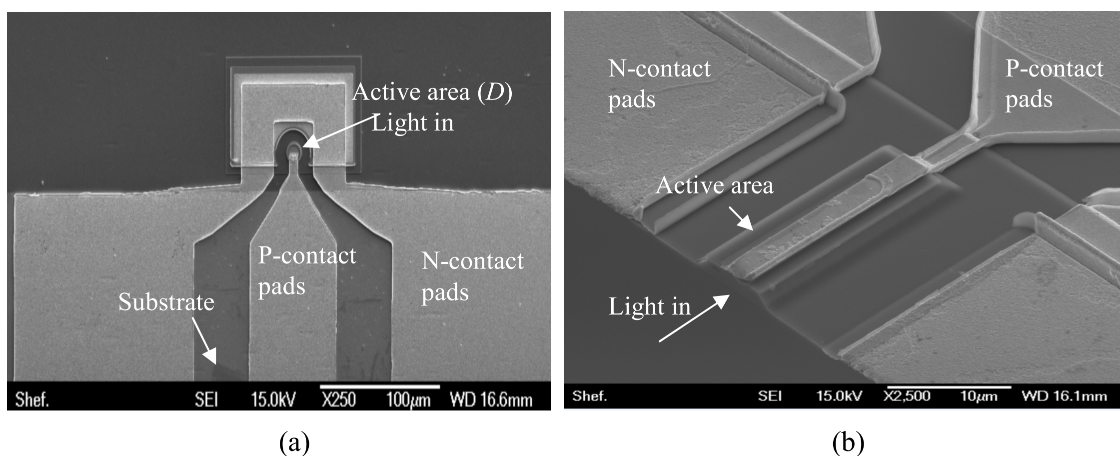

Figure 3.3.7 SEM of top view of (a) top illuminated and (b) side illuminated devices.

3.4 Reference

[1] Cho A. Y., “Epitaxy by periodic annealing,” Surf. Sci, vol 17, pp. 494,1969.

[2] Cho A. Y., “Morphology of Epitaxial growth by a Molecular Beam Method: The observation of surface structures,” J. App. Phy. Vol 41, pp. 2780, 1970.

[3] K. A. Anselm, “High-Performace Resonant-Cavity enhanced photodiodes grown by Molecular Beam Epitaxy,” Ph.D dissertation, Univeristy of Texas at Austin, 1997.

[4] Jeffrey B. Hurst, “Molecular-beam epitaxial growth of low-dark-current avalanche photodiodes,” PhD dissertation, University of Texas at Austin, 2007.

[5] W. K. Ng, "High performance of InP/InGaAs HBTs and Evanescently Coupled Waveguide Phototransistors," in EEE. Doctor of Philosophy: The University of Sheffield, 2004.

[6] I. C. Sandal, P. J. Kerr, S. Xie, J. Xie, A. S. Idris and C.H. Tan, “Temperature dependent multiplication in AlAsSb”, UK semiconductors conference, 2011.

[7] A. R. J. Marshall, “The InAs electron avalanche photodiode and the influence of thin avalanche photodiodes on receiver sensitivity”, in EEE. Doctor of Philosophy: The University of Sheffield, 2009.

[8] K. S. Giboney, “Travelling-wave photodetectors,” University of California, Santa Barbara, CA, Ph.D. Dissertation, 1995.

[9] X. Zheng, "Long wavelength high speed Photodiodes and APD Arrays," in EEE. Doctor of Philosophy: The University of Texas at Austin, 2004.

[10] S. Xie, "High speed InGaAs/InAlAs SACM APDs," in EEE. Transfer report: The University of Sheffield, 2010.

[11] G. S. Kinsey, "Waveguide avalanche photodectors," in EEE. Doctor of Philosophy: The University of Texas at Austin, 2001.

[12] Sheffield clean room fabrication instructions.

Chapter 4 High speed InGaAs p-i-n photodiode operating at 1.55 μm

This chapter describes characterisation of high speed InGaAs p-i-n photodiodes fabricated into vertically illuminated and side illuminated waveguide devices for operation at 1.55 μm. Improved bandwidth-efficiency product was achieved in the waveguide InGaAs photodiodes.

4.1 Device structure

An InGaAs p-i-n wafer was grown by molecular beam epitaxy on semi-insulating InP substrate. It comprises a p-i-n InGaAs, sandwiched between InAlGaAs and InAlAs highly doped layers, as summarised in table 4.1. The InAlGaAs layers provide bandgap grading as well as confining the optical wave in InGaAs. The diodes were fabricated into hybrid coplanar waveguide design. Detailed fabrication steps have been described in chapter 3. Vertically illuminated photodiodes (VPDs) with diameters of, D, of 10, 20, 50 and 100 μm were also fabricated on the wafer to verify RC-limited bandwidth. The side illuminated waveguide devices (hereafter WG-PDs) are fabricated with ridge width w_{ridge} = 5 μm and the waveguide length, L, of 15, 30 and 55 μm. The top p-type contact width on the WG-PDs is 2 μm. The bond pad length of all the diodes is 300 μm.

Table 4.1 Epitaxial layer structure of InGaAs p-i-n photodiodes.

Layer	Material	Doping (cm^{-3})	Type	Nominal thickness (nm)
Cap	$In_{0.53}Ga_{0.47}As$	5×10^{18}	p^+	20
Cladding	$In_{0.52}Al_{0.48}As$	5×10^{18}	p^+	300
Cladding	InGaAlAs (E_g=1.1eV)	2×10^{18}	p^+	600
Core	$In_{0.53}Ga_{0.47}As$	2×10^{18}	p^+	50
Core	$In_{0.53}Ga_{0.47}As$	undoped	i	300
Core	$In_{0.53}Ga_{0.47}As$	2×10^{18}	n^+	50
Cladding	InGaAlAs (E_g=1.1eV)	2×10^{18}	n^+	600
Cladding	$In_{0.52}Al_{0.48}As$	5×10^{18}	n^+	100
Buffer	$In_{0.53}Ga_{0.47}As$	5×10^{18}	n^+	300
InP semi-insulating substrate				

4.2 Experimental details

4.2.1 *C-V* measurement

C-V measurement was performed on VPDs with diameters of 100 µm as shown in figure 4.2.1. Parasitic capacitance between the bond pads on the semi-insulating substrate of ~ 48 fF was measured. The *C-V* was modeled to estimate the intrinsic layer thickness in the structure. Dielectric constant of 13.5 [1] was used for InGaAs. The rapid drop of the capacitance in the modeled *C-V* was due to the simplified assumption of the abrupt junction in the model but dopant diffusion is likely to occur in the real structure. The modeled *C-V* data suggests the intrinsic layer thickness is equivalent 0.31 µm, close to the nominal value.

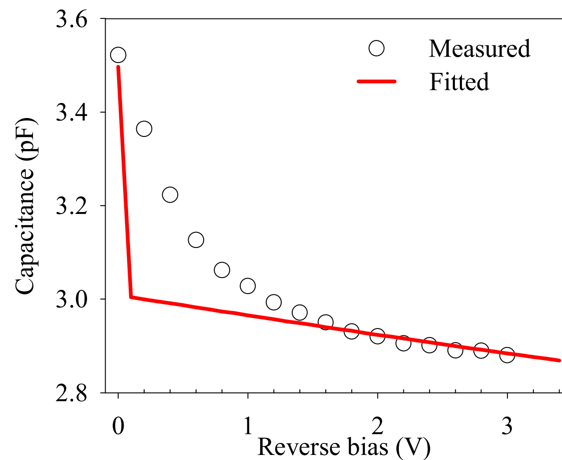

Fig 4.2.1 Measured and modeled capacitance for InGaAs p-i-n diode with a diameter of 100 µm.

4.2.2 Dark *I-V* measurement

Room temperature dark *I-V* characteristics of all the diodes are shown in figure 4.2.2. Dark current measurements show incomplete suppression of the surface leakage current since the measured current does not scale with the diode area nor the surface perimeter.

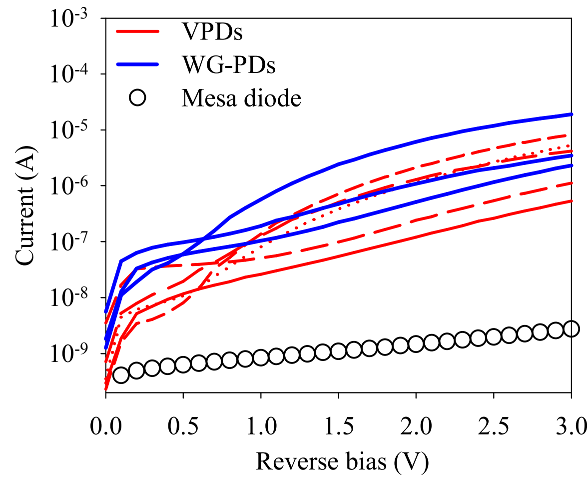

Figure 4.2.2 Dark current measurements for all the devices. The mesa diode with 100 μm diameter was shown for comparison.

4.2.3 Responsivity measurement

A 1.55 μm laser coupled into a hemispherical-ended single mode fibre was focused onto the top of the VPDs and side cleaved facet of the WG-PDs. The input optical power was measured using a commercial Perkin Elmer C30665 InGaAs p-i-n photodiode and a standard power meter for consistency check. The photocurrent at a reverse bias of 2 V was measured using a source measure unit. All the diodes do not have an antireflection (AR) coating. Responsivity values of 0.38, and 0.48 A/W were measured for VPDs and WG-PDs, corresponding to external quantum efficiencies of 30.4 and 38.4%. It is worth noting that although the waveguide devices have different waveguide lengths, their responsivities were indistinguishable.

4.2.4 Frequency response measurement

The on-wafer frequency response measurements were performed using the optical heterodyne setup [2, 3], as detailed in chapter 2. All the devices were reverse biased at 2 V so that the structure was been fully depleted. The measured frequency response results are shown in figure 4.2.3 (a) for VPDS and (b) for WG-PDs. The -3 dB bandwidths of the VPDs are 23.5, 13.4, 6.0 and 1.28 GHz for the diodes diameters of 10, 25, 50 and 100 μm, respectively. Clearly the bandwidth reduces with device area. However WG-PDs show

similar -3 dB bandwidths, with values of 26.5, 24.8 and 25.2 GHz for WG-PDs with L = 15, 25 and 50 μm respectively, which seems to be independent of diode area within the experimental error.

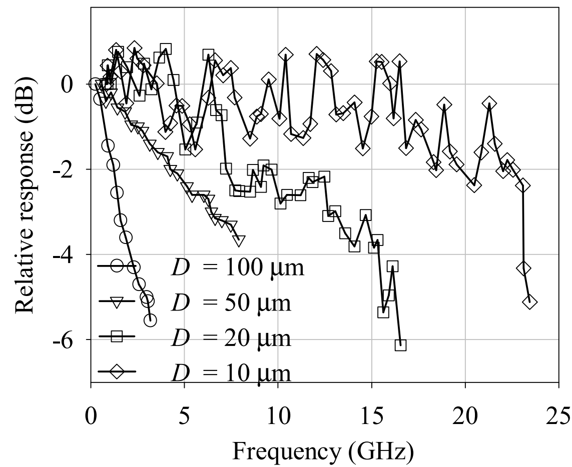

(a)

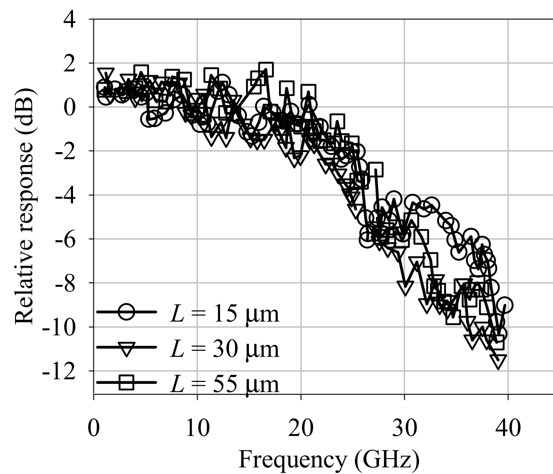

(b)

Fig 4.2.3 Relative frequency response measurement by using heterodyne for different type of diodes: (a) VPDs with different diameters (b) WG-PDs with different waveguide lengths.

4.3 Discussions

All the diodes showed dominant surface leakage currents. A mesa diode without passivation and bond pad with a diameter of 100 μm was fabricated to investigate the

origin of the surface current, as shown in Fig 4.2.1. Surface leakage current in this unpassivated mesa diode and without bond pad is at least 2 orders of magnitude lower compared to the other diodes, suggesting the surface leakage current is predominantly originating from the surface degradation caused by the PECVD process used for SiN_x dielectric layer deposition at a temperature of 300 °C and the un-optimised bond pads on the semi-insulating substrate. Lowering the SiN_x deposition temperature or replacing SiN_x with SU-8 which is processed at room temperature may reduce the dark current in the diodes. Etching deeper into the substrate or growing an undoped buffer layer to avoid possible reduced resistivity due to n-type dopant diffusion from the bottom n^+ InGaAs layer may also improve the leakage current.

The capacitance per unit area of the structure is 2.02×10^{-4} pF/μm^2. The parasitic capacitance of ~ 48 fF, originating from the un-optimised semi-insulating substrate between the bond pads, was measured. The contact resistivity value of 4×10^{-6} Ω.cm^2 was extracted from the TLM model [4]. Hence the total capacitance and resistance, including the contact resistance from the metal and the load resistance of 50 Ω, can be estimated to predict the conventional -3 dB RC limited bandwidth from equation (1.1.5) as shown in table 4.2.

The calculated -3 dB RC-limited bandwidths are in reasonable agreement with our measured bandwidths for VPDs, confirming that bandwidth decreases with increasing diode area due to the RC lumped effect. However the measured values are significantly lower than the predicted values in all the WG-PDs. We attribute this to un-optimised bond pads leading high microwave loss. Therefore the bond pads were modified in the mask set for fabricating the travelling-wave APDs in chapter 5.

Table 4.2 Calculated capacitances, series resistances, -3 dB RC-limited bandwidth and measured -3 dB bandwidth for VPDs and WG-PDs.

Diodes	Dimensions	Total capacitance (pF)	Resistance (Ω)	Calculated RC -3 dB bandwidth	Measured -3 dB bandwidth
VPDs	D =10 μm	0.08	72	27.6	23.5
	D = 20 μm	0.175	55	16.5	13.4
	D = 50 μm	0.84	51	3.72	6.0
	D = 100 μm	3.22	50	0.99	1.28
WG-PDs (w_{ridge} = 5 μm)	L = 15 μm	0.063	56	45.1	26.5
	L = 30 μm	0.078	52	39.2	24.8
	L = 55 μm	0.103	50	30.9	25.2

Higher responsivity results measured in the WG-PDs compared to VPDs are attributed to the longer waveguide absorption lengths. However the same responsivity results in WG-PDs with different waveguide lengths also showed that the waveguides are longer than the required length for fully absorption laser light (99.9%) is 5.8 μm assuming an absorption coefficient of 0.8 /μm for InGaAs [5] at the wavelength of 1.55 μm. Therefore no advantage was gained by increasing the length of WG-PDs beyond 5.8 μm.

The highest bandwidth-efficiency values obtained for the VPDs and WG-PDs are 7.14 and 10.2 GHz respectively, which were calculated by selecting the highest -3 dB bandwidth for each type of diode and multiplying the corresponding external quantum efficiency. The results therefore show that WG-PDs can improve the bandwidth-efficiency product for high speed applications.

4.4 Conclusions

InGaAs p-i-n vertically illuminated and side illuminated waveguide photodiodes were fabricated and characterised. The measured -3 dB bandwidth for the VPDs reduces with increasing device area and is consistent with the calculated RC bandwidth. The measured -3 dB values for WG-PDs with different waveguide lengths show lower values than the calculated RC-bandwidths. This is attributed to the un-optimised bond pad and thus limiting the device bandwidth. However higher bandwidth-efficiency product is still achieved using the WG-PDs, providing advantage in high speed communication systems.

4.5 Reference

[1] J. E. Bowers, and C.A. Burrrus, “Ultrawide-band long-wavelength p-i-n photodetectors’, *IEEE, J. Lightwave Technol.*,vol. 5, pp. 1339-1350, 1987.

[2] S. Kawanishi, A. Takada, and M. Saruwatari, "Wide-band Frequency- Response Measurement of Optical Receiver Using Optical Heterodyne Detection," *J. Lightwave Tech.*, vol. 7, 1989.

[3] M. C. Teich, "Infrared heterodyne detection," *Proceedings of the IEEE*, vol. 56, pp. 37-46, 1968.

[4] W. K. Ng, "High performance of InP/InGaAs HBTs and Evanescently Coupled Waveguide Phototransistors," in *EEE*. *Doctor of Philosophy*: The University of Sheffield, 2004.

[5] S. Adachi, Physical Properties of III-Y Semiconductor compounds. *John Wiley and Sons*.1992.

Chapter 5 High speed InGaAs/InAlAs SAM APD

With the great increase in internet data traffic comes a high demand for high performance photodiodes to convert optical signals to electrical currents. Hence this chapter aims to develop low dark current, high bandwidth and low excess noise APDs for high bit-rate 40 Gb/s optical communication systems. This chapter describes the characteristics of high speed, low noise InGaAs/InAlAs SAM APDs achieved by successful incorporating a "travelling wave" design to remove the RC effects of the APDs.

5.1 Device structure

Two separate absorption and multiplication (SAM) APD structures were grown by molecular beam epitaxy on InP semi-insulating (S.I) substrate. Both structures have two nominal 50 nm InGaAlAs (with a bandgap, E_g, of 1.1 eV) grading layer on either sides of an InGaAs absorption layer, a 200 nm InAlAs field control layer and a 200 nm InAlAs multiplication layer. The InGaAs absorption layer is 600 nm for M3698 and 1200 nm for M3587. The layer structure details are summarised in table 5.1 and 5.2.

Table 5.1 Structural details of the SAM APD (M3698) showing nominal values compared to those deduced from *C-V* fitting.

Layer	Material	Doping concentration (cm^{-3})		Thickness (nm)	
		Nominal	Fitted	Nominal	Fitted
p^+ cap	InGaAs	5×10^{18}	5×10^{18}	10	10
p^+ cladding	InAlAs	$> 5 \times 10^{18}$	5×10^{18}	300	300
Grading	InAlGaAs (E_g = 1.1 eV)	undoped	1×10^{18}	50	50
i-absorber	InGaAs	undoped	6×10^{15}	600	440
Grading	InAlGaAs (E_g = 1.1 eV)	undoped	7×10^{15}	50	50
p charge sheet	InAlAs	2×10^{17}	1.7×10^{17}	200	200
i multiplication	InAlAs	undoped	1×10^{16}	200	200
n^+ cladding	InAlAs	$> 5 \times 10^{18}$	2×10^{18}	100	100

n$^+$ etch stop	InGaAs	1×10^{19}	1×10^{19}	300	300
InP semi-insulating substrate					

Table 5.2 Structural details of the SAM APD (M3587)

Layer	Material	Doping concentration (cm^{-3})		Thickness (nm)	
		Nominal	Fitted	Nominal	Fitted
p$^+$ cap	InGaAs	5×10^{18}	5×10^{18}	10	10
p$^+$ cladding	InAlAs	$> 5 \times 10^{18}$	5×10^{18}	300	300
Grading	InAlGaAs (E_g = 1.1 eV)	Undoped	2×10^{15}	50	50
i-absorber	InGaAs	Undoped	2×10^{15}	1200	1200
Grading	InAlGaAs (E_g = 1.1 eV)	Undoped	2×10^{15}	50	50
p charge sheet	InAlAs	1.8×10^{17}	1.88×10^{17}	200	200
i multiplication	InAlAs	Undoped	$4 \text{ x } 10^{15}$	200	165
n$^+$ cladding	InAlAs	$> 5 \times 10^{18}$	2×10^{18}	100	100
n$^+$ etch stop	InGaAs	1×10^{19}	1×10^{19}	300	300
InP semi-insulating substrate					

5.2 Theoretical characteristic impedance

The hybrid coplanar transmission line model [1], described in detail in chapter 2.1.2, was employed to predict the frequency dependence of the impedance of the two SAM APDs configured in a long thin waveguide configuration. The simulated impedances for a range of waveguide devices with different values of ridge metal width, w_p, and ridge mesa width, w_{ridge}, are shown in figures 5.2.1 (a) and (b).

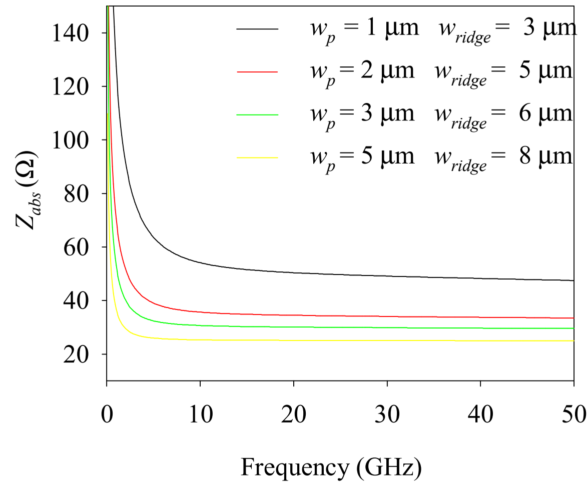

(a)

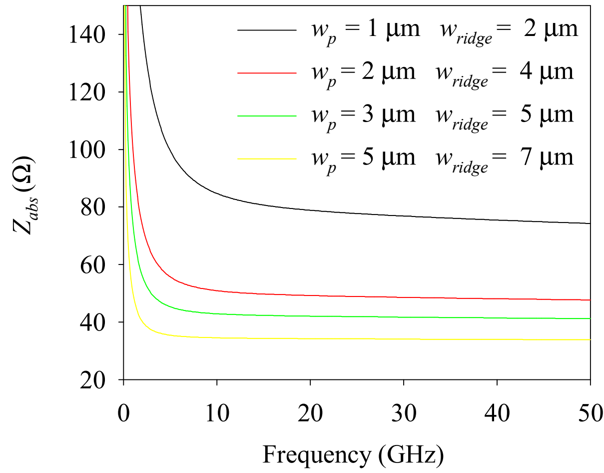

(b)

Figure 5.2.1 Simulated absolute characteristic impedance for InGaAs/InAlAs SAM APD: (a) M3698 and (b) M3587 using a hybrid coplanar transmission line model.

The simulation suggests that the side illuminated waveguide APD (WG-APD) designs incorporating w_p = 2 μm, w_{ridge} = 4~5 μm with a gap between the signal and ground contact of w_{gap} = 7 μm will produce absolute characteristics impedance, Z_{abs} close to 50 Ω independent of waveguide length L. Therefore waveguide APDs in which the electrical and optical waves interacted over a sufficiently long length (usually > 10s of μm) can be called travelling-wave APDs (TWAPDs).

The lateral injection WG-APDs were therefore fabricated from M3587 and M3698 using the process described in Chapter 3. Both set of devices have lengths of 15 to 55 µm, w_p = 2 µm, w_{ridge} = 5 µm (M3698) and 4 µm (M3587) and w_{gap} = 7 µm. The coplanar waveguide bond pads for microwave probing are 125 µm long as shown in figure 5.2.2.

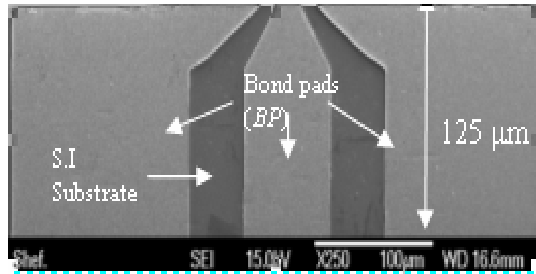

Figure 5.2.2 Schematic of waveguide bond pads in the diodes.

5.3 Experimental details

5.3.1 *C-V* measurement

Room temperature *C-V* measurements performed on test mesa diodes with diameters of 50 µm are shown in figures 5.3.1 (a) for M3698 and (b) for M3587, respectively.

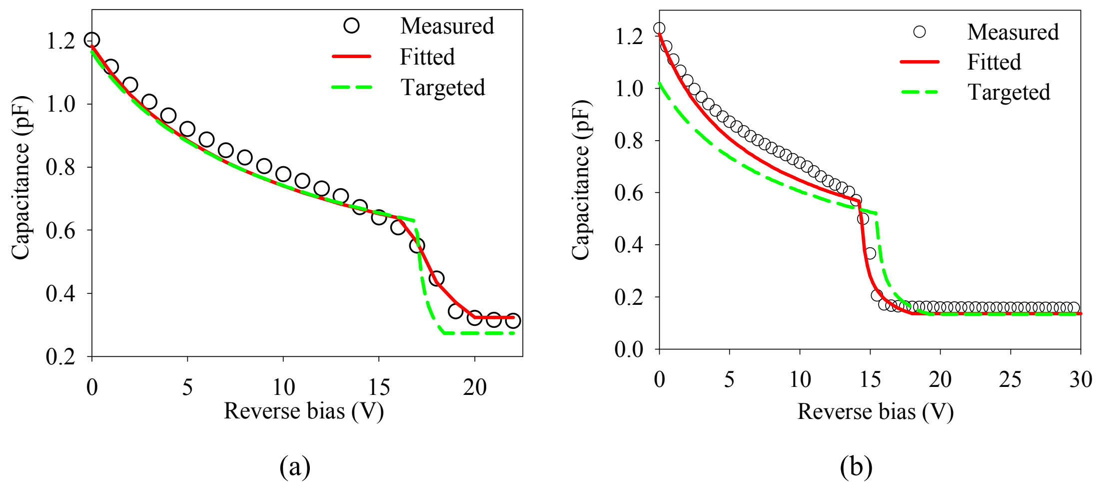

Figure 5.3.1: Comparisons between measured, fitted and targeted *C-V* for a diode with diameter of 50 µm for (a) M3698 and (b) M3587.

A rapid drop in the capacitance, corresponding to the increase in the depletion region was measured between 14.5 to 17.4 V for M3698 and 14 to 16 V for M3587. Relatively

constant capacitance was obtained at voltages above 17.4 and 16 V when the diodes are fully depleted.

Modelling of *C-V* was performed to estimate the doping and electric field profile of the SAM-APD. Dielectric constants of 12.5 [2], 13 [2, 3] and 13.5 [3] were assumed for InAlAs, InAlGaAs and InGaAs respectively. Good fit to measured *C-V* for both structures, as shown in figures 5.3.1 (a) for M3698 and (b) for M3587, and a comparison of parameters used in the *C-V* fitting and nominal targeted values for M3698 and M3587 are provided in Table 5.1 and 5.2 respectively. The modeled doping concentration value of the charge sheet is reasonably close to the targeted values in both structures. However the background doping concentration in the InGaAs absorption layer appears to be higher while the absorption layer is thinner than the intended values for M3698. In M3587 the fitting suggests that the modeled multiplication layer is thinner than intended thickness.

5.3.2 Dark *I-V* measurement

The dark *I-V* characteristics of both structures, together with those from the bond pads only, are shown in figure 5.3.2 (a) for M3698 and (b) for M3587. Breakdown voltage defined as the voltage corresponding to a dark current of 100 μA are 26.5 and 34 V for M3698 and M3587 respectively. Low dark current was achieved in all the devices, which exhibits a reasonably low value of 50 nA at 90% of the breakdown voltage. The dark current prior to the breakdown voltage is independent of device geometry suggesting that it is not related to a bulk mechanism. A comparison with the leakage current measured on reference bond pads only structure yields a good agreement, particularly at low voltages, indicating that the dark current originates from non-optimised surface preparation prior to the bond pad deposition.

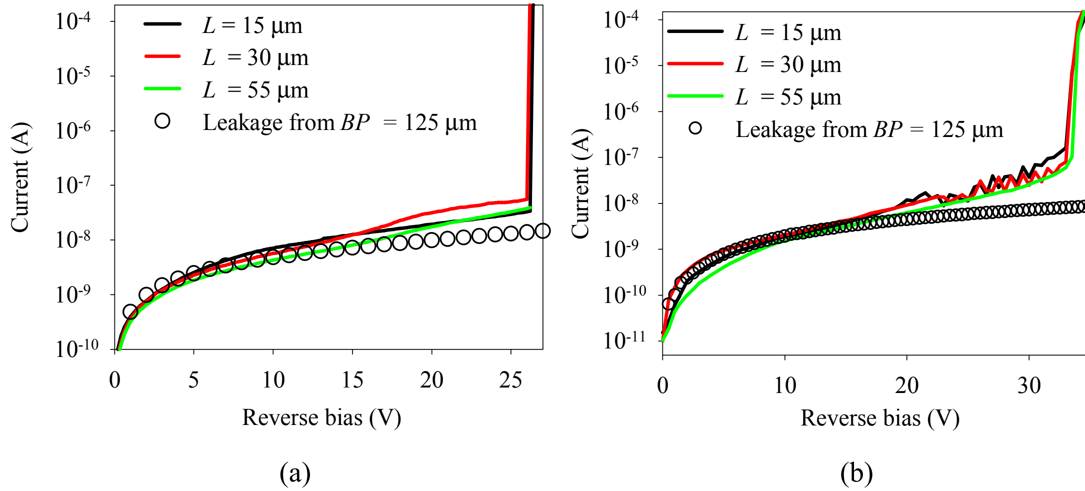

Figure 5.3.2: Dark current measurements for the devices (a) M3698 and (b) M3587 with waveguide lengths of 15, 30 and 55 µm. The leakage current originating from the bond pad, *BP*, with length of 125 µm, deposited on the semi-insulating substrate was measured (○) for comparison.

5.3.3 Excess noise measurement

A phase sensitive detection noise measurement circuit [4, 5], described in Chapter 2, was used for the mean avalanche gain, M, and the associated excess noise, F, measurements. In order to deduce the avalanche gain in the two SAM-APDs, it is necessary to measure the responsivity value at the punch-through voltage to provide a reference for the photocurrent value at unity gain. Vertically illuminated SAM-APDs were used for these measurements. A responsivity value of ~ 0.35 A/W for M3698 at – 17.6 V and ~1.1 A/W at -17 V for M3587 was measured under optical powers ranging from 50-250 µW, assuming a semiconductor reflectivity of 0.3 [6]. This responsivity value is higher than the theoretical maximum value of 0.33 and 0.54 A/W, calculated using an absorption coefficient of 8.0 x 10^3 /cm [7], expected from an InGaAs absorption layer thickness of 600 nm in M3698 and 1200 nm in M3587, suggesting an avalanche gain of at least M ~ 1.06 for M3698 and M ~ 2.04 for M3587 at their respective punch-through voltages. Typical avalanche gain and the associated excess noise factors measured using a 1.52 µm laser for both structures are shown in figures 5.3.3 (a) and (b) for M3698 and (c) and (d) for M3587. Low excess noise factor corresponding to $k \approx 0.25$ for M3698 and $k \approx 0.2$ for M3587 was measured at $M > 5$. The measured noise is in good agreement to those

measured from InAlAs pin diodes with avalanche regions of 100 and 200 nm [9]. Measurements on side illuminated waveguide APDs produced consistent results.

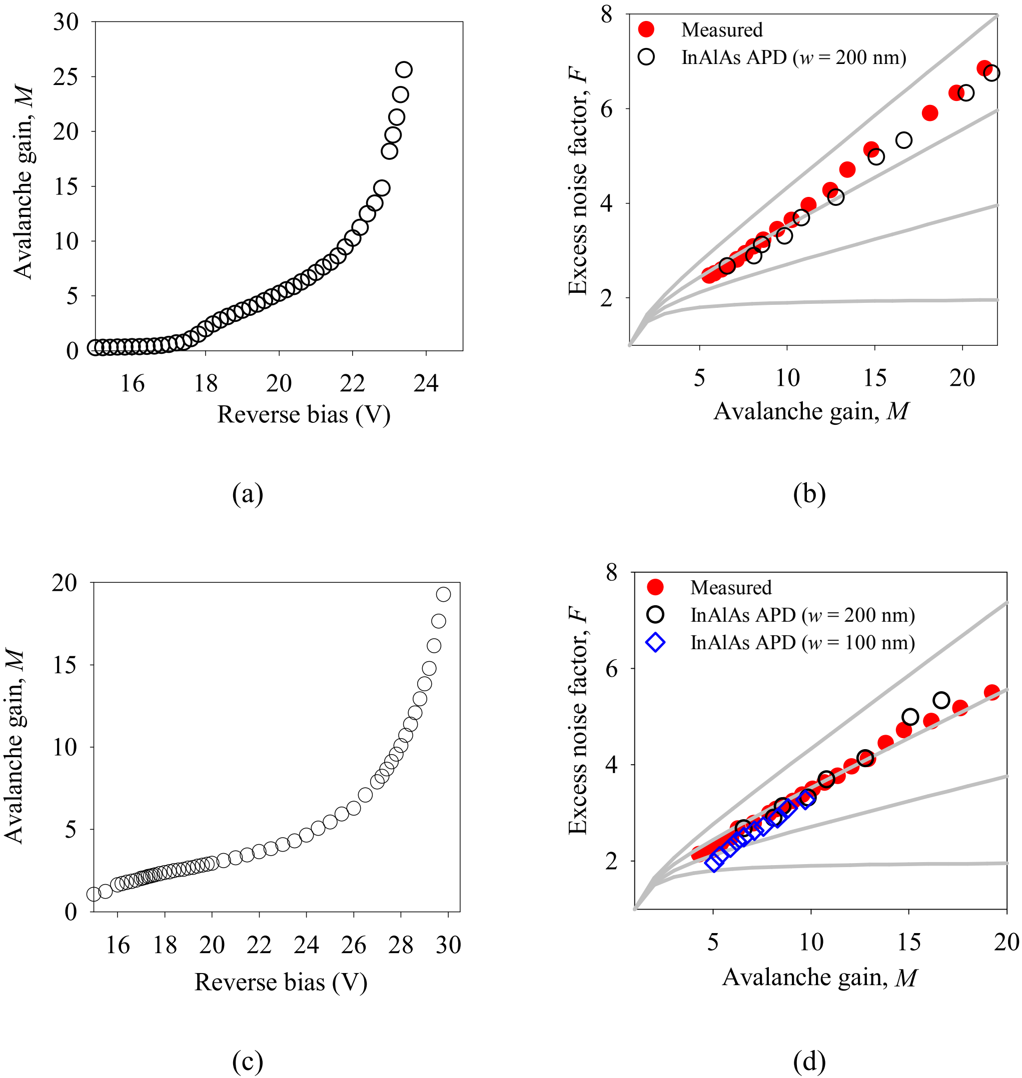

Figure 5.3.3: Measured avalanche gain and excess noise factor for M3698: (a) and (b) and for M3587: (c) and (d). The lines corresponding to $k = 0$ to 0.20 (with an increment of 0.1), in the local noise theory [8]. Excess noise measured on InAlAs p-i-n diodes with avalanche regions of 200 and 100 nm are included for comparison [9].

5.3.4 Frequency response measurement

The on-wafer frequency response measurements between 10 MHz and 40 GHz were performed using the laser with a 40 GHz optical modulator, as described in chapter 2. The modulator was driven by a 50 GHz Agilent network analyser with the modulating RF

power of -2 dBm. Modulated laser was illuminated to the active area of the devices. The photocurrent measurements were shown in figures 5.3.4 (a) for M3698 (5 × 15 μm^2) and (b) for M3587 (4 × 15 μm^2). The two diodes show punch-through voltages of ~ 17.6 and ~ 17.0 V. A wide-bandwidth of 50 GHz p-i-n photodetector from u2t Photonics, German (XPDV) was measured as a reference diode for comparison. Figures 5.3.5 (a) and (b) show the frequency response at a range of biasing for the fabricated devices with L = 15 μm. Taking the response at punchthrough voltage as a reference and ensuring that the response was at least 10 dB higher than the system noise level, the response in both APDs was found to be amplified with the increased bias voltage due to their internal gain, providing advantages over p-i-n photodetectors. The values of the response increment at some selected frequencies for each device are shown in table 5.3. APDs fabricated from M3587 show higher response increment than M3698, particularly at frequencies above 20 GHz.

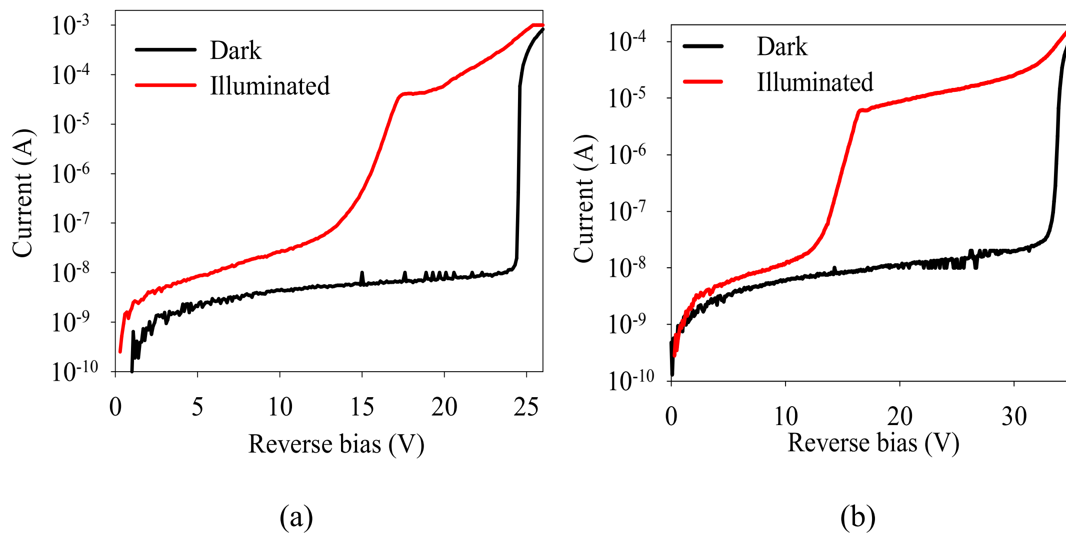

Figure 5.3.4 Photocurrent measurement at the wavelength of 1.3 μm for (a) M3698 and (b) M3587.

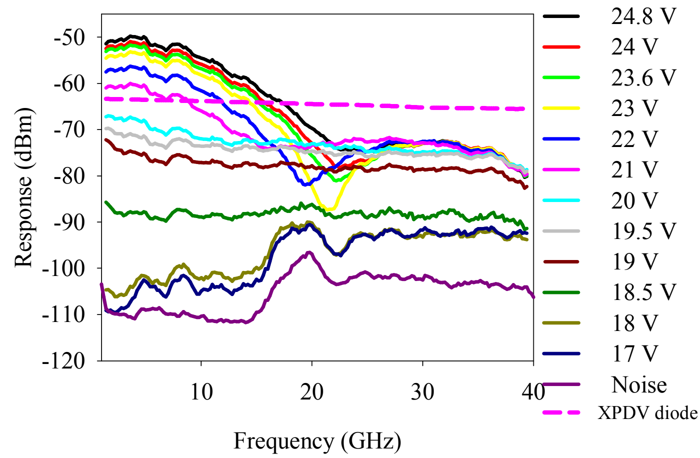

(a)

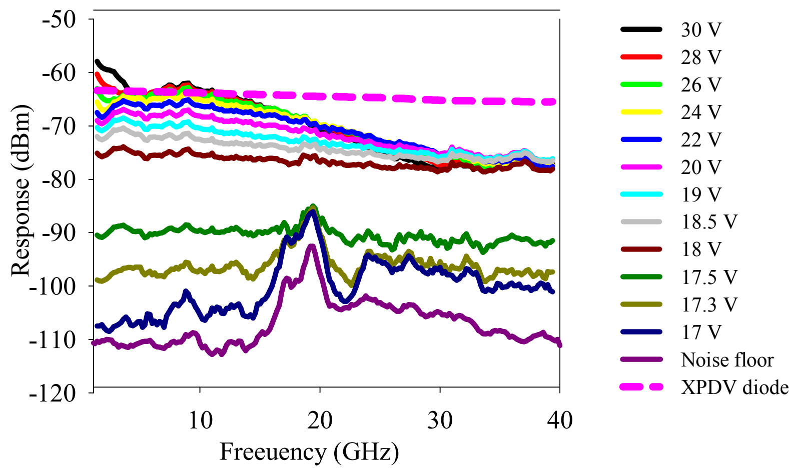

(b)

Figure 5.3.5 Frequency response measurements on (a) M3698 and (b) M3587 under different reverse bias voltages.

Table 5.3 Enhanced response with reverse bias voltage at selected frequencies

Frequency	Maximum response increment (dB) with respect to response at 17.6 V M3698	Maximum response increment (dB) with respect to response at 17 V M3587
10 GHz	44.0 (23 V M = 18)	42.0 (-30 V M = 21.45)
20 GHz	18.4 (-20.5 V M = 6.0)	28.0 (-25 V M = 5.4)
30 GHz	17.0 (-20 V M = 5.2)	21.0 (-21 V M = 3.3)
35 GHz	12.0 (-20 V M = 5.2)	24.0 (-20 V M = 3.0)

The frequency responses of APDs with different waveguide lengths were measured and their relative frequency response normalised to their values at 1.09 GHz at low gains was calculated for bandwidth comparison. The normalisation point was selected due to the high noise level in the setup below 1 GHz. The results are shown in figures 5.3.6 (a) for M3698 at ~ 18 V and (b) for M3587 at 17 ~ 17.5 V. Bandwidth measurement for the reference XPDV diode was also performed for comparison. Wide bandwidth at low gains, at voltages < 19 V under reverse biasing, was obtained for both APDs, as their similar relative frequency responses at low gains exhibited similar trend to the commercial XPDV diode, after an initial 10 dB drop before 10 GHz in APD M3698. In addition, both APDs with different waveguide lengths show a similar relative frequency response from the frequencies ranging 1.09 to 40 GHz. The upper frequency is limited by the optical modulation used in the current setup.

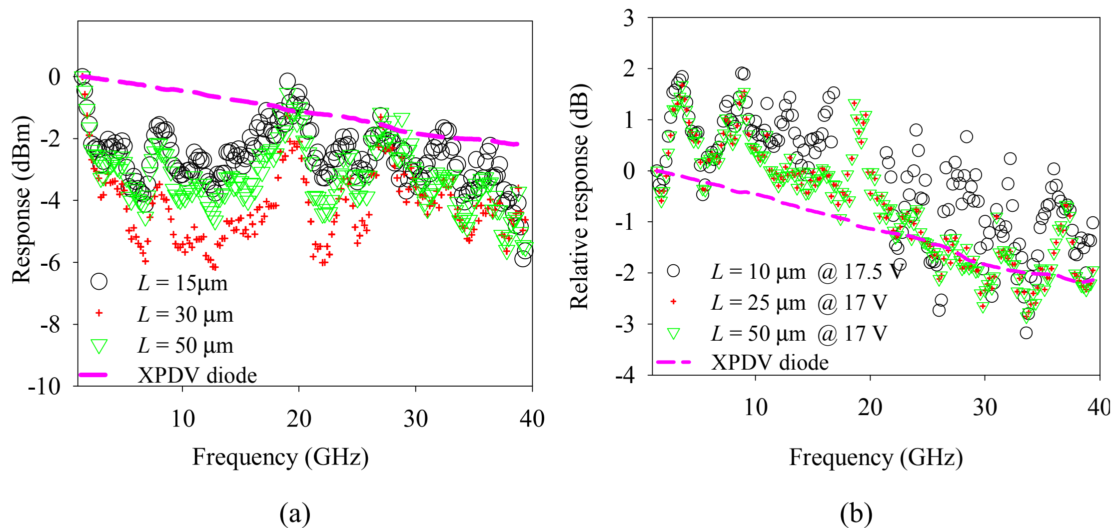

Figure 5.3.6 Relative frequency responses of the devices with different waveguide lengths for (a) M3698 at 18 V and (b) M3587 at 17 ~ 17.5 V. Commercial 50 GHz XPDV diode is included for bandwidth comparison.

5.3.5 Power dependence measurement

The devices response varied with reverse biases and was measured at frequencies of 1, 10, 20, 30 and 35 GHz as a function of the modulating power at a range that varied the optical RF. power. This allows us to investigate the linearity of our APDs. The RF power

from the network analyser was varied from -27 to 0 dBm. Higher RF power was not used as the ratio of APD output power to the modulating RF power was lower than the minimum ratio expected by the network analyser. The results are shown in figures 5.3.7 (a) for M3698 and (b) for M3587. Power dependence measurements for the reference XPDV diode with the same RF power range were also performed for linearity comparison.

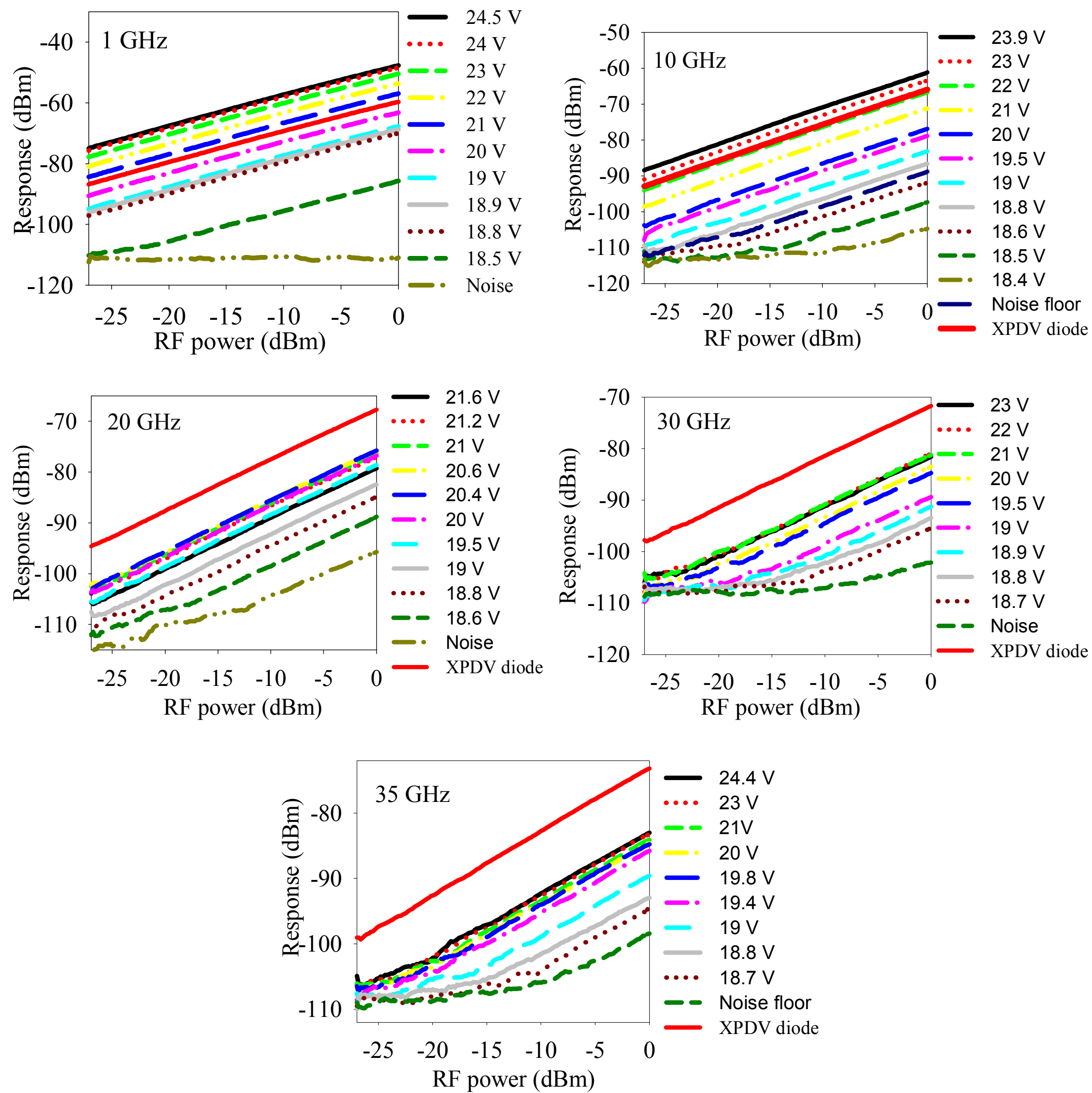

(a)

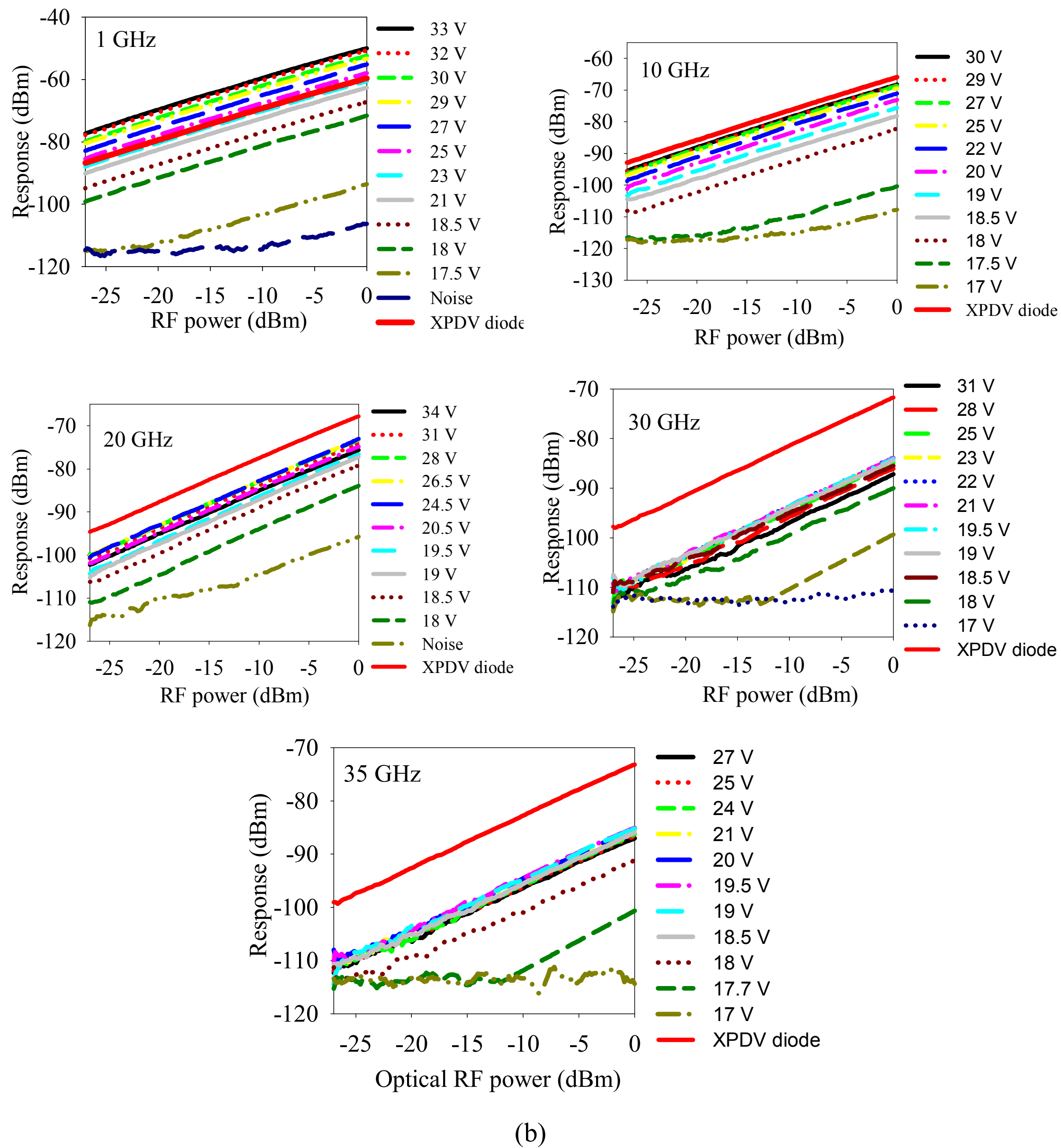

(b)

Figure 5.3.7 Power sweep at fixed frequency in (a) M3698 and (b) M3587. Commercial 50 GHz XPDV diode is included for linearity comparison.

5.4 Discussions

Dark current measurements showed both structures with different waveguide lengths have similar leakage currents, suggesting the dominant dark current is not bulk current. Measurements of leakage current between the bond pads show good agreement to those

from the diodes indicating the un-optimised bond pads as the source of leakage. Hence mesa diodes without bond pads for both structures were also fabricated. The bulk current density was 9.4×10^{-5} and 1.67×10^{-3} A/cm^2 at 90% of the breakdown voltage for M3698 and for M3587 respectively, corresponding to the bulk dark current below 0.26 and 3.7 nA at 90% of the breakdown for both WG-APDs, which is lower than the reported planar InGaAs/InAlAs APD [11] with the current density value of 1.0×10^{-2} A/cm^2 and the high speed resonant-cavity InGaAs/InAlAs APDs [12] with the value of 1.2×10^{-2} A/cm^2 at 90% of breakdown voltage. Further improvement of bond pad via effective etching etchant and etching depth to the semi-insulating substrate, effective passivation, and improving the resistivity of the substrate may help reduce the leakage dark current. Although the bond pads are not optimised, the dark current remains below 50 nA in M3698 with the biggest diode area of 5 × 55 µm^2 and in M3587 with the biggest diode area of 4 × 55 µm^2 at a bias of 90% of the breakdown voltage. There are approximately 20 times lower than the 40 Gb/s waveguide APD reported by Makita *et al.* [10] with the diode area of 6 × 20 µm^2, as shown in Fig 5.4.1. To our best knowledge, the APD reported by Makita *et al*, is the best reported for 40 Gb/s communication system.

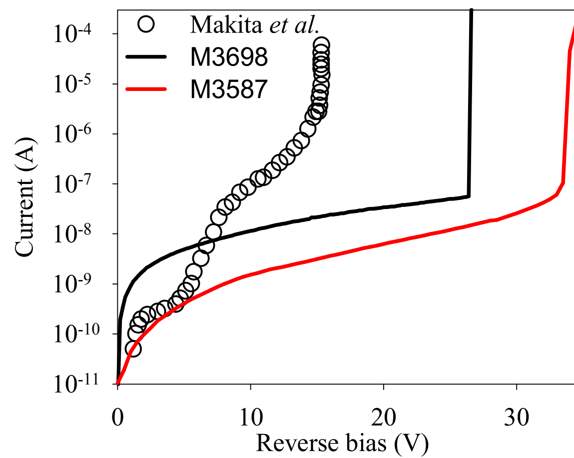

Figure 5.4.1 Dark current comparisons for M3698 with the diode area of 5 × 55 µm^2, M3587 with the diode area of 4× 55 µm^{2}and the 40 Gb/s InGaAs/InAlAs waveguide by Makita *et al.* [10] with the diode area of 6 × 20 µm^2.

Since the APD fabricated from M3698 have a 200 nm InAlAs multiplication layer as deduced from the *C-V* modelling, its measured excess noise show the similar results as

those from InAlAs p-i-n diodes with a 200 nm avalanche region, suggesting the method used to deduce the gain at punchthrough voltage from the responsivity measurements was reasonable. Similarly the APDs fabricated from M3587 have a 165 nm InAlAs multiplication layer, and its excess noise falls between InAlAs p-i-n diodes with avalanche regions of 200 and 100 nm, demonstrating the consistence of excess noise for our APD with the InAlAs p-i-n diodes with the same avalanche region thickness. Our results suggest negligible excess noise contribution from the charge sheet and the absorption layer and hence verifying the epilayer design shown in tables 5.1 and 5.2.

To predict the RC time constants of our APDs we characterised the APD capacitance and the contact resistance. The capacitance per unit area of M3698 and M3587 are 1.33×10^{-4} pF/μm^2 8.0582×10^{-5} pF/μm^2, respectively. The parasitic capacitance originating from the bond pads was found to be value of ~ 21 fF. The contact resistivity value of 1.2×10^{-4} Ω.cm^2 was extracted from the Transmission Line Model (TLM) [13]. Hence the capacitance per unit area was scaled to the approximate APD area of the vertically illuminated diode with diameter of 100 μm while the resistance including the contact resistance was estimated from the metallisation area and the load resistance of 50 Ω, to estimate -3 dB RC limited bandwidth using equation (1.1.4). The calculated values are shown in table 5.4 and 5.5 for 3698 and for M3587 respectively.

Table 5.4 Calculated capacitance, series resistance, RC limited bandwidth for M3698 with different waveguide lengths

M3698			
Dimensions (w_{ridge} = 5 μm)	Capacitance (pF)	Resistance (Ω)	Calculated -3dB RC limited bandwidth (GHz)
L = 15 μm	0.031	450	11.4
L = 30 μm	0.041	250	15.5
L = 55 μm	0.058	159	17.2

Table 5.5 Calculated capacitance, series resistance, RC limited bandwidth for M3587 with different waveguide lengths

M3587			
Dimensions (w_{ridge} = 4 μm)	Capacitance (pF)	Resistance (Ω)	Calculated -3dB RC limited bandwidth (GHz)
L = 15 μm	0.026	450	13.6
L = 30 μm	0.031	250	20.5
L = 55 μm	0.039	159	25.7

The capacitance in both diodes are 30 ~ 50 fF for M3698 and 26 ~ 40 fF for M3587, and these values are comparable to that from the 40 Gb/s waveguide APD reported by Makita *et al.* [10] with junction capacitance of 20 ~ 30 fF. However the un-optimised contact resistance in both waveguide diodes show a much higher value compared to the one reported by Makita *et al.* [10] with a series resistance of 10 Ω and total resistance of 60 Ω. Hence the bandwidth in both diodes should be lower compared to the 40 Gb/s APD reported by Makita *et al.* [10] from the RC limited bandwidth consideration. In addition, from the calculation of the RC limited bandwidth for both APDs with different waveguide lengths which is shown in table 5.4 and 5.5, the frequency response of each APD with different waveguide lengths should be different. However both sets of devices show a similar relative frequency response as shown in figure 5.3.6(a) and (b), indicating their frequency response are independent of area. In addition of the similar relative response in both APDs compared to the commercial XPDV diode suggests that our APDs have a wide bandwidth up to 40 GHz, which are higher compared to the calculated RC-limited bandwidth. Therefore our APDs seem to have overcome the conventional RC lump circuit effect. While our APDs are only up to 55 μm long, we believe the RC independent bandwidth represents a strong indication that “travelling-wave APDs” have been successfully achieved. It is worth noting that both APDs as well as the commercial XPDV diode show an initial frequency response drop before 10 GHz, which is probably due to the optical output variation from the optical modulator and some impedance mismatch effect at lower frequency, which causes a difficulty in defining the -3 dB bandwidth and thus the uncertainty of GBP value. Nevertheless, the amplification

amplitude at different frequency as shown in table 5.3 shows a significant signal enhancement 24 dB of at 35 GHz demonstrating the potential of our travelling-wave APD for 40 Gb/s applications. We believe the large enhancement due to a reasonably large gain represent a significant improvement over the 40 Gb/s InGaAs/InAlAs APD reported by Makita *et al*. [10], who have demonstrated their APD with GBP value of 140 GHz and at 35 GHz with M = 2 or 3, corresponding to maximum AC signal amplification of 9.5 dB at 35 GHz. The higher amplification amplitude in M3587 than M3698 shown in table 5.3 is probably due to its thinner multiplication layer and thus a higher GBP.

Though the high bandwidth was obtained in both diodes, reducing the parasitic bond pad capacitance and lowering the contact resistance by increasing the doping in the cladding layer (> 10^{19} /cm^3) and optimisation of the metallisation process can improve the RC limited bandwidth and reduce the difficulty in designing an active diode to be impedance match to the external circuit.

There is no saturation effect observed within the RF power range in both two diodes as shown in figure 5.3.7. Both sets of diodes were edge-cleaved and thinned without any cleave facet engineering, and thus the cleaving process could induce facet geometry variation and damages, which may result the lower optical coupling efficiency and higher optical return loss in our diodes compared to the commercial 50 GHz XPDV diode. Therefore both diodes showed a lower response at punchthrough voltage compared to the commercial diode at all the frequency. However strong response amplification with bias was observed in both diodes. Particularly higher response with gain can be obtained in both diodes before 20 GHz compared to the commercial 50 GHz XPDV diode. The response amplification drops after 20.4, 20 and 19.8 V for M3698 and 25, 21 and 19.5 V for M3587 at the frequency of 20, 30 and 35 GHz respectively. Therefore lower response compared to the commercial XPDV diode is also probably due to the GBP effect.

5.5 Conclusion

Two high speed InGaAs/InAlAs SAM APDs utilising travelling wave design were grown and characterised. Responsivity values of 0.35 and 1.1 A/W were measured at punch-through voltages of M3698 and M3587 respectively. Low excess noise factor corresponding to $k \approx 0.25$ and $k \approx 0.2$ were obtained for multiplication layer thicknesses of 200 nm for M3698 and 165 nm for M3587, which are comparable with InAlAs p-i-n diodes with similar avalanche region thickness. Both APDs show a wide bandwidth up to 40 GHz at low gains and higher values compared to the RC calculated bandwidth. And a similar relative response at low gains for each diode with different waveguide lengths suggests the devices are not affected by RC effects and behave as “travelling wave APDs”. No signal saturation effect has been observed at the RF power ranging from -27 to 0 dBm. Both APDs show a capability of signal amplification up to 40 GHz. Particularly they have higher signal amplification at 35 GHz and lower dark current compared to the best InGaAs/InAlAs APD at 40 Gb/s reported by Makita *et al.* [10], proving their superiority and suitability in use for 40 Gb/s communication system.

5.6 Reference

[1] K. S. Giboney, M. J. W. Rodwell, and J. E. Bowers, "Travelling-wave photodetector design and measurements," *IEEE J. Selected Topics in Quantum Electron.* , vol. 2, pp. 622-629, 1996.

[2] M. A. Littlejohn, K. W. Kim and H. Tian “High-field transport in InGaAs and related heterostructures,” *Properties of lattice-matched and strained Indium Gallium Arsenide*, INSPEC, pp. 114, 1993.

[3] J. E. Bowers, and C.A. Burrrus, “Ultrawide-band long-wavelength p-i-n photodetectors’, *IEEE, J. Lightwave Technol.*,vol. 5, pp. 1339-1350, 1987.

[4] K. S. Lau, C. H. Tan, B. K. Ng, K. F. Li, R. C. Tozer, J. P. R. David, and G. J. Rees, “Excess noise measurement in avalanche photodiodes using a transimpedance amplifier front-end,” *Meas. Sci. Technol.*, vol.17, pp. 1941–1946, 2006.

[5] K. F. Li, D. S. Ong, J. P. R. David, G. J. Rees, R. C. Tozer, P. N. Robson, and R. Grey,"Avalanche multiplication noise characteristics in thin GaAs p+-i-n+ diodes", *IEEE Trans. Electron Dev.,* vol. 45, no. 10, pp. 2102-2107, 1998.

[6] S. A. Alterovitz "Dielectric functions and refractive index of $In_xGa_{1-x}As$," *Properties of lattice-matched and strained Indium Gallium Arsenide*, INSPEC, pp. 188, 1993

[7] S. Adachi, Physical Properties of III-Y Semiconductor compounds. *John Wiley and Sons*.1992.

[8] R. J. McIntyre, "Multiplication noise in uniform avalanche diodes," *IEEE Trans on Electron Dev.*, vol. 3, pp. 164-168, 1966.

[9] Y. L. Goh, D. J. Massey, A. R. J. Marshall, J. S. Ng, C. H. Tan, W. K. Ng, G. J. Rees, M. Hopkinson and J. P. R. David, "Excess noise in $In_{0.52}Al_{0.48}As$", *IEEE J. of Quantum Electron.*, vol.43, pp.503-507, 2007.

[10] K. Makita, T. Nakata, K. Shiba and T. Kakeuchi, "40Gbps waveguide photodiodes", J. of *Adv. Tech*., Summer, 2005.

[11] B. F. Levine, R. N. Sacks, J. Ko, M. Jazwiecki, J. A. Valdmanis, D. Gunther, and J. H. Meier, "A New Planar InGaAs–InAlAs Avalanche Photodiode," *IEEE Photon. Technol. Let*., vol. 18, pp. 1898–1900, Sep. 2006.

[12] C. Lenox, H. Nie, P. Yuan, G. Kinsey, A. L. Homles, Jr., B. G. Streetman, and J. C. Campbell, "Resonant-Cavity InGaAs–InAlAs Avalanche Photodiodes with Gain-Bandwidth," *IEEE Photon. Technol. Let*., vol. 11, pp. 1162–1164, Sep. 1999.

[13] W. K. Ng, "High performance of InP/InGaAs HBTs and Evanescently Coupled Waveguide Phototransistors," in *EEE*. *Doctor of Philosophy*: The University of Sheffield, 2004.

Chapter 6 Temperature dependence in AlAsSb

Chapter 5 has described the high speed InGaAs/InAlAs SAM APD with InAlAs multiplication layer thickness of 200 nm and GBPs 160 GHz [1]. Further reduced the avalanche region width in InAlAs is impeded by its onset of band to band tunneling current. The minimum value for telecom APDs at 10 Gb/s with a bit error rate of 10^{-12} are reported as 180 and 150 nm [2] for InP and InAlAs avalanche regions respectively. Therefore, new materials either with significantly superior ionization coefficient ratios or much lower tunneling currents to achieve much thinner avalanche regions will be necessary to obtain low excess noise, high GBPs and low temperature coefficients $AlAs_{56}Sb_{0.44}$ (hereafter AlAsSb), lattice matched to InP, has an indirect bandgap of 1.65 eV, which is larger than the direct bandgaps of 1.34 eV in InP and 1.45 eV in InAlAs, and its phonon assisted tunnelling process [3] can be expected to exhibit a lower band to band tunnelling current and a smaller temperature coefficient of breakdown voltage, $C_{bd} = \Delta V_{bd}/\Delta T$, where ΔV_{bd} and ΔT are the breakdown voltage and temperature differences with thinner avalanche regions. This chapter describes temperature dependence of dark current and avalanche gain on AlAsSb p-i-n diodes with avalanche region widths of 80 and 230 nm at temperatures ranging from 77 to 295 K. Band to band tunelling current is investigated in the thinner diode at electric fields up to 1.07 MV/cm.

6.1 Device structure

Two p-i-n wafers were grown by molecular beam epitaxy (MBE) on semi-insulating InP substrates using Be and Si as the p^+ and n^+ type dopants respectively. The nominal layer details are summarised in table 6.1. The first wafer PIN1 has an avalanche region of w = 100 nm while the second wafer PIN2 has a thicker w of 250 nm. Two p-i-n wafers were grown by molecular beam epitaxy (MBE) on semi-insulating InP substrates using Be and Si as the p^+ and n^+ type dopants respectively. The first wafer PIN1 has an avalanche region of w = 100 nm while the second wafer PIN2 has a thicker w of 250 nm. Circular mesa diodes with diameters, D of 50, 100, 200, 400 μm were fabricated by wet chemical etching using a 1:1:1 mixture of hydrobromic acid: acetic acid: potassium dichromate

solution. Ti/Au (20/200 nm) was deposited to form the top and bottom electrical contacts. Measurements and modelling of the voltage dependence of capacitance indicated that the depletion region widths are 80 and 230 nm, thinner than the nominal values.

Table 6.1 Epitaxial layer structure of AlAsSb based p-i-n APDs.

Layer	Material	Doping (/cm^3)	Thickness (nm)	Dopant
p^+ cap	InGaAs	5×10^{18}	50	Be
p^+ cladding	AlAsSb	2×10^{18}	400	Be
i-intrinsic (avalanche region)	AlAsSb	undoped	100 (PIN1) 250 (PIN2)	
n^+ cladding	AlAsSb	2×10^{18}	50	Si
n^+ etch stop	InGaAs	5×10^{18}	1000	Si
InP semi-insulating substrate				

6.2 Experimental details

6.2.1 *C-V* measurement

Room temperature *C-V* measurements were performed on the PIN1 and PIN2 diodes. Figure 6.2.1 (a) and (b) shows the typical *C-V* profiles of 400 μm diameter diodes in PIN1 and PIN2 respectively and the corresponding modelled results. Dielectric constant of 10.95 was assumed for AlAsSb [4] and built-in voltage, V_{bi}, was assumed to be 0.9 V. Measurements and modelling of the voltage dependence of capacitance indicated that the intrinsic region widths in PIN1 and PIN2 are 80 and 230 nm, thinner than the nominal values. The background doping well below 1×10^{16} cm^{-3} in the avalanche region and high doping concentrations of $\sim 1 \times 10^{18}$ cm^{-3} in the p^+ and n^+ layers were deduced. Deduced peak electric fields at $0.95V_{bd}$ in PIN1 and PIN2 are 1.07 and 0.8 MV/cm.

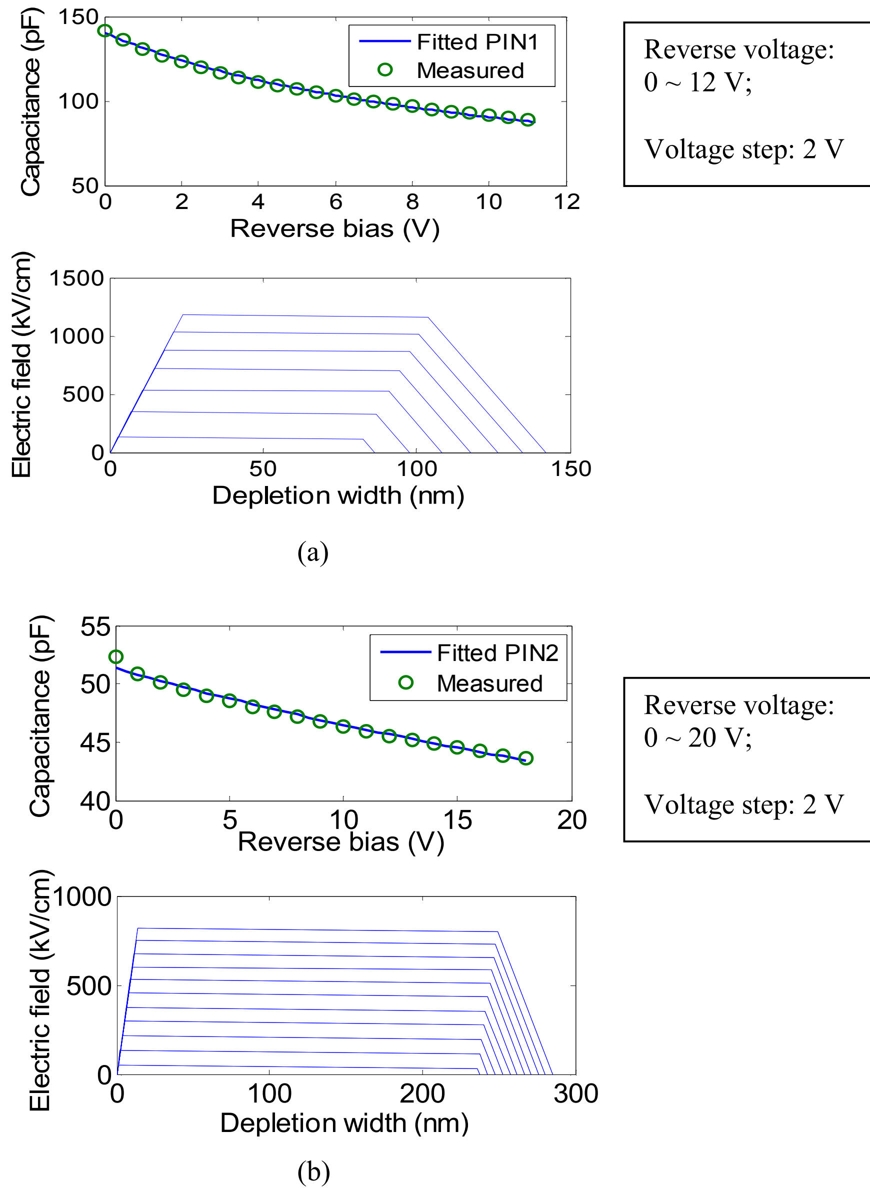

Figure 6.2.1 Measured (symbols) and fitted (lines) *C-V* characteristics and deduced electric field profile for AlAsSb diodes with D = 400 µm and w = 80 nm (a) and 230 nm (b).

6.2.2 Temperature dependence of dark current

On wafer dark *I-V* measurements at 77, 140, 200, 250 and 295 K were performed on unpassivated diodes with D = 100 to 400 µm on both p-i-n structures using a low-temperature probe station. Typical temperature dependence *I-V* results from diodes with D = 200 µm are shown in figure 6.2.2. The dark current in PIN1 is dominated by surface

leakage since the measured current scales with the diode perimeter at all temperatures. In PIN2 the dark current scales neither with the surface perimeter nor the area suggesting that both surface and bulk components are significant. The dark currents in both structures also reduce with decreasing temperatures with dark currents of < 10 nA obtained in PIN1 and < 30 nA obtained in PIN2 at $0.9V_{bd}$ when the temperatures are below 200 K.

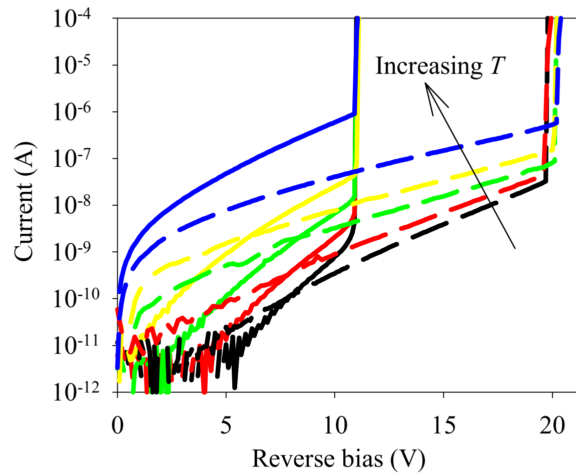

Figure 6.2.2: Measured *I-V* characteristics for AlAsSb diodes with D = 200 μm and w = 80 nm (solid lines) and 230 nm (dash lines) at temperatures, T of 77, 140, 200, 250 and 295 K.

Well defined V_{bd}, taken to be the voltage corresponding to the dark current of 100 μA was obtained for all devices at the temperatures measured. In PIN1 V_{bd} drops from 11.10 to 10.98 V, a reduction of 10%, as the temperature reduces from 295 to 77 K. A larger change in V_{bd} was observed in PIN2, with a drop from 20.4 to 19.8 V, representing a reduction of 29.4%, as the temperature was varied over the same range.

6.2.3 Temperature dependence of avalanche gain

In order to determine unambiguously the temperature dependence of avalanche breakdown voltage, to isolate the contribution of surface leakage current and to rule out premature edge breakdown in the diodes, the temperature dependence of mean avalanche gain, M, measurements were performed using phase-sensitive detection techniques. This, obtained by mechanically chopping the laser beam with a wavelength of 633 nm, allows

the photocurrent to be measured independent of the dark current and electronic noise. Despite the low absorption confident at the wavelength of 633 nm for AlAsSb [6] and there was mixed carrier injected into the intrinsic layer, the avalanche breakdown voltage should have little dependence on injected carrier type [7]. The laser was illuminated on the centre of the diodes from the top surface of the p-i-n diodes and care was taken to prevent carrier generations at the sidewalls. Since the capacitance-voltage measurements showed small increase in the depletion width with bias, the increase in the primary photocurrent due the bias dependence of the collection efficiency was estimated using the technique proposed by Woods *et al* [8]. The total photocurrent was normalised to this primary photocurrent to provide the avalanche gain. The measured gain for PIN1 and PIN2 at 77, 140, 200, 250 and 295 K is shown in figure 6.2.3 (a) and (b). The results show small variations of avalanche gain with temperature in these AlAsSb diodes. At a given bias the gain increases marginally as the temperature is reduced. Consequently the temperature dependence of V_{bd} is also weak. The values of V_{bd} were estimated by linearly extrapolating the $1/M$ curves to 0, as shown in figure 6.2.4 (a) and (b) for PIN1 and PIN2 respectively. We obtained V_{bd} = 11.27 V at 295 K dropping to V_{bd} = 11.06 V at 77 K for PIN1 and V_{bd} = 20.46 V at 295 K dropping to V_{bd} = 20.2 V at 77 K for PIN2, yielding C_{bd} values of 0.95 mV/K and 1.48 mV/K respectively.

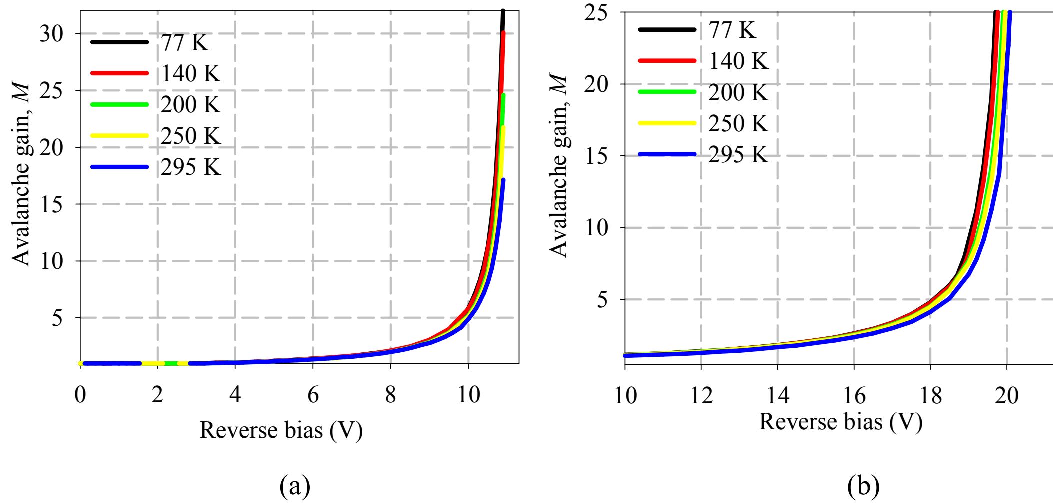

Figure 6.2.3: Avalanche gain or multiplication measured using a 633 nm laser on the diodes with (a) w = 80 nm and (b) 230 nm at temperatures of 77, 140, 200, 250 and 295 K.

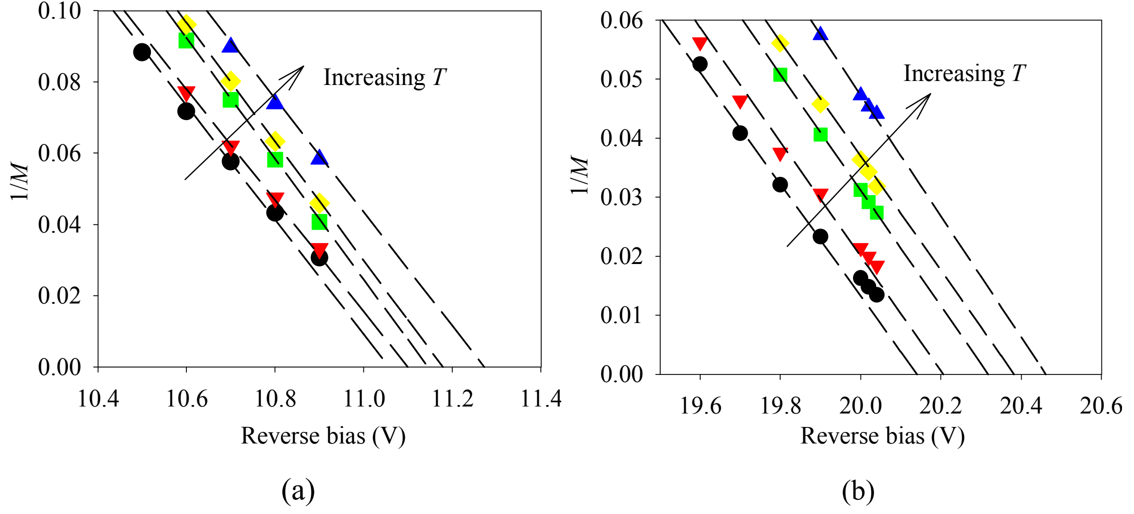

Figure 6.2.4: Extrapolation of $1/M$ to 0 for the diodes with (a) w = 80 nm and (b) w = 230 nm at temperatures of 77, 140, 200, 250 and 295 K.

6.3 Discussions

The measured dark currents in both structures are predominantly surface leakage current at room temperature. This is most probably due to the absence of surface passivation, non-optimised etching procedures and the presence of high composition of Al which is known to oxidise easily when exposed. Despite the lack of surface passivation the dark current reduces significantly at low temperatures. The temperature dependence of dark current provides valuable data to assess whether band to band tunelling current is significant in our diodes. Band to band tunelling can be described by [9]

$$I_{tunn} = \frac{(2m^*)^{0.5} q^3 \xi V_t A}{h^2 E_g^{0.5}} \exp\left[-\frac{2\pi\sigma_T (m^*)^{0.5} (E_g)^{1.5}}{qh\xi}\right] \quad , \qquad (6.3.1)$$

where m^* is the effective electron mass, q is the electron charge, V_t is applied reverse bias voltage, ξ is the electric field, A is the device area, h is the Plank's constant, E_g is the band gap and σ_T is a constant that depends on the detailed shape of the tunelling barrier. E_g is replaced by $E_g + E_p$, where E_p is the phonon energy, when modelling indirect band gap materials.

Equation. (6.3.1) shows that the band to band tunelling current increases rapidly with the electric field. To obtain a low tunelling probability, the effective mass and bandgap should be large and the electric field should be small. Figure 6.3.1 shows the calculated tunelling current using equation (6.3.1) for InP and InAlAs diodes at the temperatures of 293 and 14 K for ideal pin diodes with w = 80 nm. The values of the bandgap in InP are given by empirical equation [10] and the band gaps at 293 and 14 K for InAlAs were taken Roura *et al.* [8], while the values of σ_T for InP was used as 1.15 [12] and 1.26 for InAlAs [13]. The results show that the tunelling current depends weakly on temperature in both materials, reducing by approximately an order of magnitude when the temperature reduces from 290 to 14 K. In contrast we observed several orders of magnitude reduction in the dark currents in both PIN 1 and PIN2 diodes indicating insignificant tunelling current. The 77 K dark current density in PIN1 is as low as 10^{-5} A/cm^2 at a reverse bias of $0.95V_{bd}$, corresponding to a field of 1.07 MV/cm. This is not surprising because AlAsSb has a larger band gap of 1.65 eV and it is an indirect band gap material. The indirect tunnelling for indirect band gap materials with the change of momentum in *k*-space has to be compensated by phonon assisted scattering. The tunnelling probability is reduced by replacing E_g to be $E_g + E_p$, while E_p is the phonon energy and therefore the magnitude of the tunnelling current as described by equation (6.3.1) is reduced. In addition associated with the momentum is its vector direction relates to the direction of tunnelling. There only the energy associated with momentum in the tunnelling direction contributes to the tunnelling process and the transverse momentum which is perpendicular to the direction of tunnelling can reduce the tunnelling probability. [3] Moreover the rule of thumb in Si APDs suggests that the avalanche mechanism generally dominates if the breakdown voltage is well above $6E_g/q$ [14]. In PIN1 the breakdown voltage is 11.27 V which is greater than $6E_g$ (9.9 V). Our data confirms that tunelling current is insignificant at least up to a field of 1.07 MV/cm which is much higher than the fields where tunelling current become dominant in InP and InAlAs. Therefore AlAsSb avalanche region as thin as 80 nm has great potential to be used in conjunction with an InGaAs absorption layer to improve the bandwidth (due to reduced carrier transit time) and excess noise (due to enhanced dead space effects in sub-micron avalanche regions) for future telecom APDs.

More work will be necessary to establish the lower limit of w in AlAsSb before tunelling current becomes intolerable.

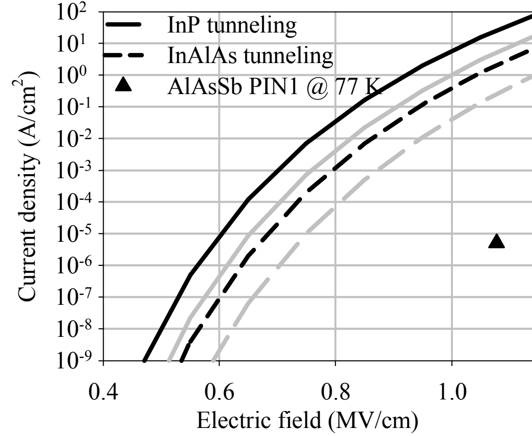

Figure 6.3.1 Calculated tunelling current density for InP and InAlAs diode with w = 80 nm at 290 and 14 K and comparing with the current density in PIN1 at 77 K.

The temperature coefficients of breakdown voltage for different semiconductor materials, such as Si [15], GaAs [16], $Al_{0.6}Ga_{0.4}As$ [17], GaInP [18], InP [19] and InAlAs [20] are compared in figure 6.3.2 and a comparison for diodes with w < 300 nm is provided in table 6.2 for. It is clear that PIN1 with w = 80 nm shows the smallest C_{bd} than all materials with a range of w except for the thinnest GaAs diode with w of 25 nm. The C_{bd} value of 0.95 mV/K in our AlAsSb diodes is lower than the values of 3.9 mV/K for InP and 2.2 mV/K for InAlAs diodes with the same w, estimated using extrapolation of data in Ref [16]. However the band to band tunelling current rapidly increases at biases close to V_{bd} in GaAs diodes with $w \leq$ 95nm [16], InP diodes with $w \leq$ 130nm and InAlAs diodes with $w \leq$ 100nm [21] making it impractical to use such thin diodes for improving the temperature stability of GaAs, InP and InAlAs APDs. While the origin of the small C_{bd} in our AlAsSb is not fully understood, we believe it can be attributed to the combined effects of very thin w of 80 nm, large phonon energy and a strong alloy scattering. In general the value of C_{bd} decreases with w due to the reduced influence of phonon scattering at high electric fields in diodes with thin w [22]. Carriers encounter less phonon at high electric fields and hence the population of hot carriers is less dependent on temperature at high fields leading to a smaller C_{bd}. The phonon scattering rate is

proportional to $N = (exp(\hbar\omega/kT)\text{-}1)^{-1}$ the phonon occupation number, where $\hbar\omega$ is the phonon energy, k is Boltzmann's constant and T is the absolute temperature. Clearly a material with a large phonon energy will exhibit a smaller temperature dependence of N leading to a weaker temperature dependence of the population of hot carriers and hence a smaller C_{bd}. Finally the alloy scattering is given by [23]

$$\frac{1}{\tau_{alloy}} = \frac{3\pi}{8\sqrt{2}}\frac{(m^*)^{3/2}}{\hbar^4} \times x(1-x)\frac{a^3}{4}(\Delta E_a)^2[\gamma(E)]^{1/2}\frac{d\gamma(E)}{dE}s^{-1} \tag{6.3.2}$$

where a is the lattice constant, and ΔE_a is the alloy scattering potential, $\gamma(E)=E*(1+\alpha E)$ is the approximation of the nonparabolicity of the conduction band and E is the carrier energy. This scattering rate is independent of temperature and we speculate that this could also contribute the small C_{bd} in our AlAsSb alloy.

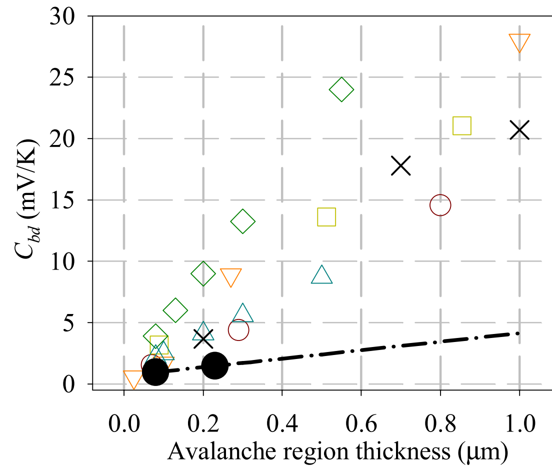

Figure 6.3.2 Comparison of C_{bd} for AlAsSb (●), Si (○) [15], GaAs (▽) [16], $Al_{0.6}Ga_{0.4}As$ (□) [17], GaInP (×) [18] InP (◇) [19] and InAlAs (△) [20] diodes with submicron avalanche regions.

Table 6.2 A comparison of C_{bd} in diodes with w < 300 nm

Material	w (nm)	C_{bd} (mV/K)	w (nm)	C_{bd} (mV/K)
AlAsSb	80	0.95	230	2.7
Si [15]	70	1.53	290	4.38
GaAs [16]	100	1.67	270	8.89
$Al_{0.6}Ga_{0.4}As$ [17]	89	3.176	--	--

GaInP [18]	--	--	200	3.68
InP [19]	80	3.9	200	6.0
InAlAs [20]	80	2.2	200	4.1

6.4 Conclusion

We have grown, fabricated and measured the temperature dependence of dark current, avalanche gain and breakdown voltage in AlAsSb diodes with *w* = 80 and 230 nm. Measurements at temperatures ranging from 77 to 295 K showed that the dark current in both diodes was significantly reduced with decreasing the temperature. No evidence of band to band tunelling current was observed in the thin AlAsSb diodes. Avalanche gain obtained using a 633 nm laser exhibit a weak dependence on temperature leading to a very low temperature coefficient of breakdown voltage C_{bd} = 0.95 mV/K in the diodes with *w* = 80 nm. The low tunelling current and a very small C_{bd} confirms that AlAsSb has a great potential for fabrication of APDs with sub-100 nm avalanche region widths to increase the gain-bandwidth-product and to reduce the excess noise.

6.5 Reference

[1] **S. Xie**, A. R .J. Marshall, S. Ong, J. P. R. David, and C. H. Tan, "$In_{0.53}Ga_{0.47}As$/ $In_{0.52}Al_{0.48}As$ Avalanche Photodiodes with a Gain-Bandwidth Product of 160GHz", *UK compound semiconductors conference*, July 2010.

[2] D. S. G. Ong, M. M. Hayat, J. P. R. David and J. S. Ng, "Sensitivity of High-Speed Lightwave System Receivers Using InAlAs Avalanche Photodiodes," *IEEE Photon. Technol. Let*., vol. 23, no. 4, pp. 233–235, Feb. 2011.

[3] S.M.Sze, "Physics of semiconductor devices," New York: John Wiley and Sons, 1981.

[4] D W Palmer, www.semiconductors.co.uk, 2006.02.

[5] F. Ma, G. Karve, X. G. Zheng, X. G. Sun, A. L. Holmes, and J. C. Campbell, "Low temperature breakdown properties of Al_xGa_{1-x} As avalanche photodiodes," Appl. Phys. Lett., vol. 81, no. 10, pp. 1908–1910, 2002.

[6] J. Xie, S.Xie and C. H. Tan, "Excess noise in AlAsSb", submitted to *IEEE Trans. Electron Devices*.

[7] C. H. Tan, J. P. R. David, S. A. Plimmer, G. J. Rees, R. C. Tozer, and R. Grey, "Low Multiplication Noise Thin $Al_{0.6}Ga_{0.4}As$ Avalanche Photodiodes", IEEE Trans. Electron Devices., vol. 48, no. 7, pp 1310-1317, Jul. 2001.

[8] M. H. Woods, W. C. Johnson and M. A. Lampert, "Use of Schottky barrier to measure impact ionisation coefficients in semiconductors", *Solid-State Electron.*, vol. 16, pp. 381– 394, 1973.

[9] S. R. Forrest, R. F. Leheny, R. E. Nahory, and M. A. Pollack, "In0.47Ga0.53As photodiodes with dark current limited by generation- recombination and tunelling," *Appl. Phys. Let.*, vol. 37, no. 3, pp.322–325, 1980.

[10] L. J. J. Tan, Y. L. Goh, S. C. Liew-Tat-Mun, D. S. G. Ong, J. S. Ng and J. P. R. David, "Temperature dependence of breakdown in InP and InAlAs", *IEEE Trans. Electron Devices,* vol. 46, no. 8, pp. 1153 – 1157, Aug. 2010.

[11] P. Roura, M. L. Miguel, A. Cornet, and J. R. Morante, "Determination of the direct bandgap energy of InAlAs matched to InP by photoluminescence excitation spectroscopy," *J. Appl. Phys*., vol. 81, no. 10, pp. 6916–6919, May. 1997.

[12] L. J. J. Tan, J. S. Ng, C. H. Tan and J. P. R. David, "Avalanche noise characteristics in sub-micron InP diodes", *IEEE J. of Quantum Electronics*, vol.44, no. 4, pp. 378 – 382, Apr. 2008.

[13] Y. L. Goh, D. J. Massey, A. R. J. Marshall, J. S. Ng, C. H. Tan, W. K. Ng, G. J. Rees, M. Hopkinson, J. P. R. David, and S. K. Jones, "Avalanche multiplication in InAlAs", *IEEE Trans. Electron Devices* vol. 54, no. 1, pp. 11-16, Jan. 2007.

[14] J. L. Moll, *Physics of Semiconductors*, McGraw-Hill, New York, 1964.

[15] D. J. Massey, J. P. R. David, and G. J. Rees, "Temperature dependence of impact ionisation in submicrometer Silicon devices," *IEEE Trans. Electron Devices*, vol. 53, no. 9, pp. 2328–2334, Sep. 2006.

[16] C. Groves, R. Ghin, J. P. R. David, and G. J. Rees, "Temperature dependence of impact ionisation in GaAs," *IEEE Trans. Electron Devices*, vol. 50, no.10, pp. 2027–2031, Oct. 2003.

[17] C. Groves, C. N. Harrison, J. P. R. David, and G. J. Rees, “Temperature dependence of breakdown voltage in Al_xGa_{1-x} As,” *J. Appl. Phys*., vol. 96, no. 9, pp. 5017–5019, Aug. 2004.

[18] R. Ghin, J. P. R. David, M. Hopkinson, M. A. Pate, G. J. Rees, and P. N. Robson, “Impact ionisation coefficients in GaInP p–i–n diodes”, *Appl. Phys. Let*., vol. 81, pp. 6916–6919, Apr. 1997.

[19] L. J. J. Tan, Y. L. Goh, S. C. Liew-Tat-Mun, D. S. G. Ong, J. S. Ng and J. P. R. David, “Temperature dependence of breakdown in InP and InAlAs”, *IEEE Trans. Electron Devices,* vol. 46, no. 8, pp. 1153 – 1157, Aug. 2010.

[20] Y. L. Goh, D. J. Massey, A. R. J. Marshall, J. S. Ng, C. H. Tan, W.K. Ng, G. J. Rees, M. Hopkinson, J. P. R. David, and S. K. Jones, “Avalanche multiplication in InAlAs,” *IEEE Trans. Electron Devices*, vol. 54, no. 1, pp. 11–17, Jan. 2007.

[21] D. S. G. Ong, M. M. Hayat, J. P. R. David and J. S. Ng, “Sensitivity of High-Speed Lightwave System Receivers Using InAlAs Avalanche Photodiodes,” *IEEE Photon. Technol. Let..*, vol. 23, no. 4, pp. 233–235, Feb. 2011.

[22] F. Ma, G. Karve, X. G. Zheng, X. G. Sun, A. L. Holmes, and J. C. Campbell, “Low temperature breakdown properties of Al_xGa_{1-x} As avalanche photodiodes,” *Appl. Phys. Let*.„ vol. 81, no. 10, pp. 1908–1910, Sep. 2002.

[23] J. R. Hauser, M. A. Littlejohn, and T. H. Glisson, “Velocity-filed relationship of InAs-InP alloys including the effects of alloy scattering”, *Appl. Phys. Let*., vol. 28, pp. 458 – 461, Feb. 1976.

Chapter 7 Low excess noise InGaAs/AlAsSb SAM APDs

This chapter reports the excess noise and temperature dependence of breakdown voltage in a novel separate absorption and multiplication (SAM) avalanche photodiode (APD) incorporating a 500 nm InGaAs absorption layer, InAlAs bandgap grading/field control layers, an AlAsSb field control layer and a 40 nm AlAsSb multiplication layer.

7.1 Device structure

A separate absorption and multiplication (SAM) APD structure comprising a 500 nm InGaAs absorption layer, 50 nm InGaAlAs (with a bandgap of 1eV) grading layer, 105 nm InAlAs bandgap grading/field control layers, a 44nm AlAsSb field control and a 50nm AlAsSb avalanche region was grown by molecular beam epitaxy on semi-insulating InP substrate. These layer thicknesses, deduced from modelling of capacitance-voltage (*C-V*) characteristics, and their corresponding nominal values are summarised in table 7.1. Circular mesa diodes with diameters, *D*, of 50, 100, 200 and 400 μm were fabricated by wet etching using 1: 8: 80 mixture of Sulphuric acid: Hydrogen peroxide: deionised water, followed by a finishing etch using 1:1:5 mixture of Hydrochloric acid: Hydrogen peroxide: deionised water. Ti/Au (20 nm/200 nm) was deposited to form the top and bottom electrical contacts without annealing.

7.2 Experimental details

7.2.1 *C-V* measurement

Room temperature *C-V* measurements were performed on a number of diodes and are shown in figure 7.2.1(a). The capacitance is proportional to the diode area as expected. A rapid drop in the capacitance, corresponding to the increase in the depletion region was measured between 6.0 and 8.2 V. A full depletion was achieved at ~ 8.2 V corroborating the punch-through voltage deduced from the current-voltage measurements in figure 7.2.2. Relatively constant capacitance was obtained at voltages above 8.2 V since the diode is fully depleted.

Table 7.1 Structural details of the SAM-APD

Layer	Material	Dopant	Doping concentration (cm^{-3})		Thickness (nm)	
			Nominal	Fitted	Nominal	Fitted
p^+ cap	InGaAs	Be	1×10^{19}	1×10^{19}	10	10
p^+ cladding	InAlAs	Be	$> 5 \times 10^{18}$	5×10^{18}	300	300
Grading	InAlGaAs (E_g = 1.1 eV)	--	undoped	1×10^{18}	50	50
i-absorber	InGaAs	--	undoped	6×10^{15}	500	500
grading	InAlGaAs (E_g = 1.1 eV)	--	undoped	6×10^{15}	50	50
p charge sheet	InAlAs	Be	5×10^{17}	5×10^{17}	55	55
intrinsic	InAlAs	--	undoped	1×10^{15}	50	50
p charge sheet	AlAsSb	Be	1×10^{18}	1×10^{17}	44	44
i multiplication	AlAsSb	--	undoped	1×10^{15}	50	40
n^+ cladding	AlAsSb	Si	$> 5 \times 10^{18}$	5×10^{18}	100	100
n^+ etch stop	InGaAs	Si	1×10^{19}	1×10^{19}	300	300
InP semi-insulating substrate						

Modelling of *C-V* was performed to estimate the doping and electric field profile of the SAM-APD. Dielectric constants of 10.95 [1], 12.5 [2] and 13.5 [2, 3] were assumed for AlAsSb, InAlAs and InGaAs respectively. Good fit to measured *C-V*, as shown in figure 2(b), was achieved when the following assumptions; a doping concentration of 1×10^{17} cm^{-3} in the AlAsSb field control layer, higher doping concentrations in the InGaAs absorption and InAlGaAs grading layers and thinner AlAsSb multiplication layer were made. The last two assumptions were thought to be reasonable to account for diffusion of dopants from the highly doped p and n layers. A comparison of parameters used in the *C-V* fitting and nominal values is provided in table 7.1.

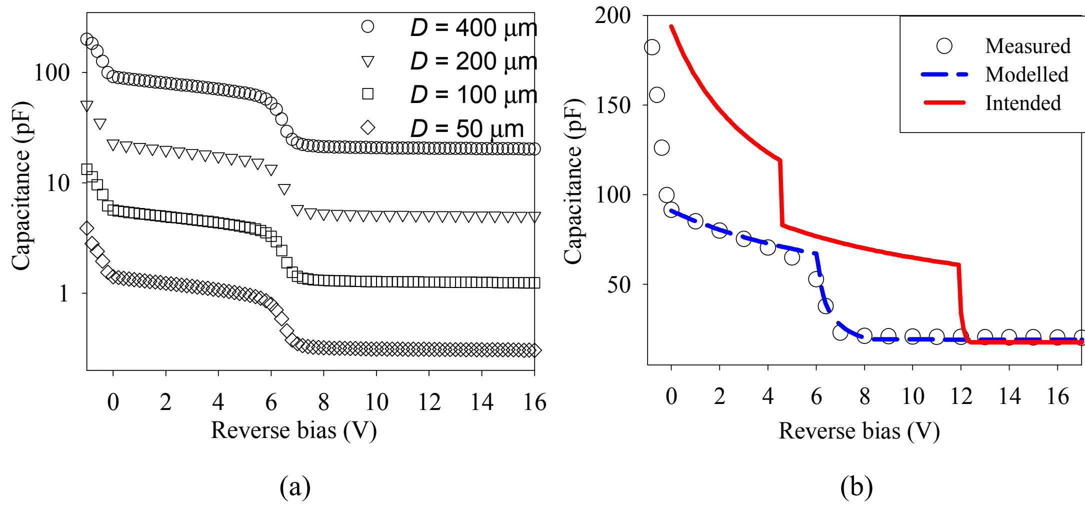

(a) (b)

Figure 7.2.1 (a) Measured capacitance for diodes with diameter of 50, 100, 200 and 400 µm. (b) Comparisons between measured, modeled and intended *C-V*.

7.2.2 Dark *I-V* measurement

The dark *I-V* characteristics of these unpassivated mesa diodes are shown in figure 7.2.2(a). Dark current measurements showed incomplete suppression of surface leakage current. The surface leakage is smaller than bulk current in diodes with $D > 50$ µm. An acceptable number of devices exhibit low dark currents which scale with the area indicating the dominance of bulk dark current. The diodes show punch-through voltage of ~ 8.2 V, corresponding to the voltage required to achieve a full depletion of the InGaAs absorption layer as shown in figure 7.2.2(b). A step increase in the dark current, associated with the higher dark current from the InGaAs layer, was measured at this punch-through voltage. The measured dark current density at this punch-through voltage is ~ 8×10^{-6} A/cm^2.

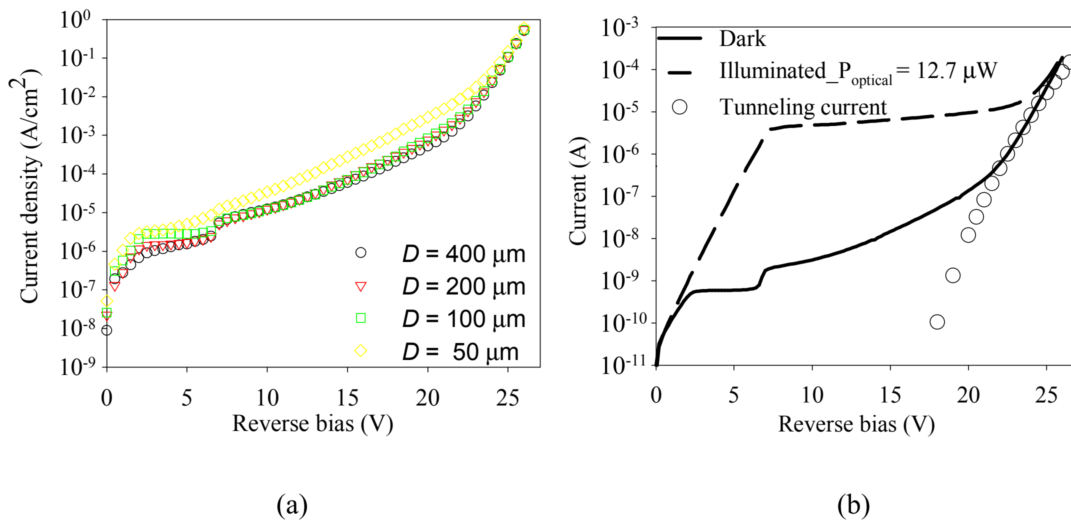

Figure 7.2.2 (a) Dark current density obtained from diodes with diameter of 50 to 400µm and (b) Comparison between dark current, photocurrent and calculated tunelling current from the InGaAs absorption layer.

7.2.3 Excess noise measurement

A customised circuit [4, 5] was used for avalanche gain, *M*, and excess noise, *F*, measurements. Using the phase sensitive detection, the gain and excess noise can be measured independent of the dark current and system noise. A 1.52 µm He-Ne laser was used to provide pure electron injection profile for the measurements. In order to deduce the avalanche gain in our SAM-APD, it is necessary to provide a reference for photocurrent value at unity gain. Hence the responsivity value at the punch-through voltage was measured to deduce the value of gain at the punch-through voltage. A responsivity value of ~ 436 mA/W was measured under optical powers ranging from 200-260 µW, assuming a semiconductor reflectivity of 0.3 [6]. This responsivity value is higher than the theoretical maximum value of 413 mA/W expected in our 500 nm InGaAs absorption layer, assuming an absorption coefficient of 8.0x10^3 /cm [7] suggesting an avalanche gain of at least *M* ~ 1.06 at the punch-through voltage. Typical avalanche gain and the associated excess noise factors measured using a 1.52 µm laser are shown in figure 7.2.3. *M* = 10 was obtained at 26.5 V. Low excess noise factors

falling between the lines $k = 0.1$ to 0.15 in the local noise theory [8] were measured at $M > 6$.

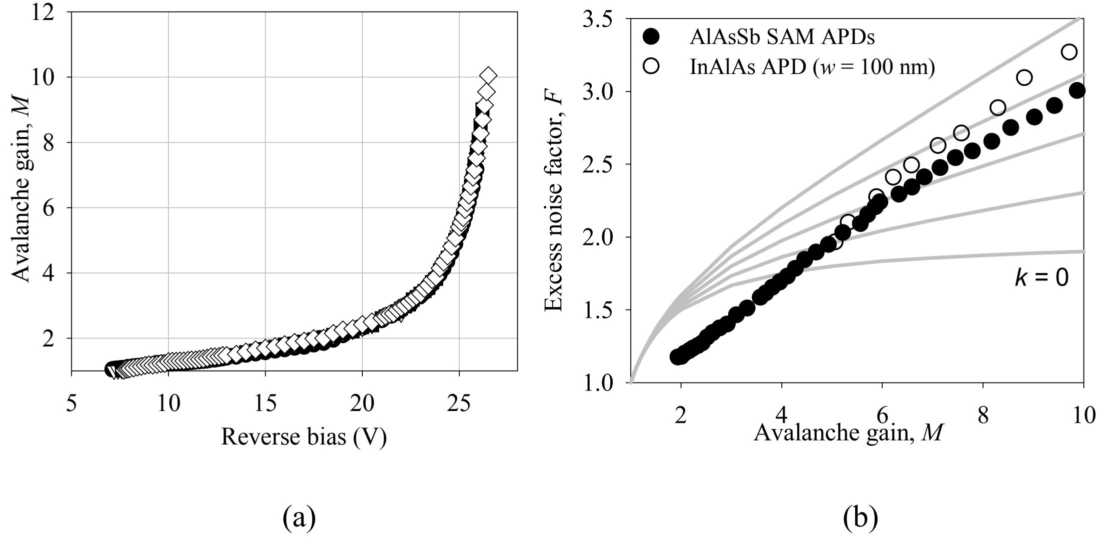

Figure 7.2.3 Measured avalanche gain (left) and excess noise factor (right). The lines corresponding to $k = 0$ to 0.20 (with an increment of 0.05), in the local noise theory [8] and excess noise measured on an InAlAs pin diode with an avalanche region of 100 nm [10] are included for comparison.

7.3 Discussions

The measured dark current is thought to be predominantly due to the generation recombination currents, at low bias voltage and band to band tunelling current from the narrow band gap InGaAs absorption layer at high bias. Although the surface leakage current in the devices is not negligible due to lack of the surface passivation, the dark current at punch-through voltage in our APDs are very competitive compared to the Ge diodes grown directly on Si, which are considered one of the leading technologies for integration with Si. The comparison is provided in table 7.2.

Table 7.2 Current density comparison between our diode and Ge based diodes.

	Current density (A/cm^2)
Our AlAsSb based diode	~8×10^{-6} A/cm^2 at punchthrough voltage ($M = 1.06$) [11]
Ge/Si APD	~0.21 A/cm^2 at -22 V (the punchthough voltage and $M = 6$) [12]
Ge/Si APD	~1.59×10^{-5} A/cm^2 at -3 V and gradually increased to 6.3694×10^{-4} A/cm^2 at -15 V ($M \sim 1$) [13]

Ge/Si photodetector	7.9618×10^{-3} A/cm^2 at -2 V (the structure fully depleted)
Ge p-i-n photodiodes on Ge substrate	2.83×10^{-5} A/cm^2 at -1 V. [14]

To estimate the tunelling current we modeled our *C-V* to extract the doping profile and calculate the electric field profile as shown in figure 7.3.1. The intended *C-V* and electric field profiles are also shown for comparison in figures 7.2.2(a) and 7.3.1 respectively.

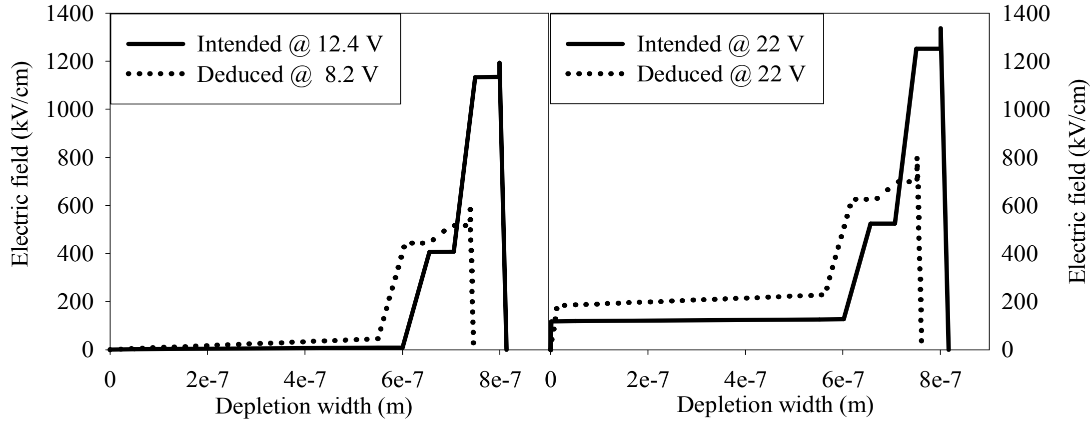

Figure 7.3.1 Deduced and intended electric field profiles at punch-through voltages (left) and at a higher bias of 22.0 V (right).

It can be seen from figure 7.2.2(b) that the full depletion should be achieved at a punch-through voltage of 12.4 V, larger than the measured voltage 8.2 V. The intended doping profile should produce two distinct drops in the capacitance at voltages of 4.4 and 11.9 V as the device depletion region extends beyond the AlAsSb and InAlAs charge sheets respectively. The deduced and intended electric field profiles are significantly different. These deviations are mainly attributed to the low Be doping concentration in the AlAsSb field control layer of ~ 1×10^{17} cm^{-3} compared to the targeted value of 1×10^{18} cm^{-3}. The secondary ion mass spectroscopy (SIMS) measurement was also performed, as shown in figure 7.3.2. The SIMS result also indicated the Be doping concentration in the charge sheet is ~ 10^{17} cm^{-3}, lower than the targeted values. This leads to high electric fields, significantly above 200 kV/cm, in the InGaAs layer resulting in high tunelling currents which can be estimated using [9]

$$I_{tunn} = \frac{(2m^*)^{0.5} q^3 \xi V A}{h^2 E_g^{0.5}} \exp[-\frac{2\pi\sigma_T (m^*)^{0.5} (E_g)^{1.5}}{qh\xi}] \qquad (1)$$

where m^* is the effective electron mass, q is the electron charge, ξ is the electric field, A is the device area, h is the Plank's constant, E_g is the direct band gap and σ_T is the constant dependent on the barrier shape. σ_T = 1.21 was found to yield good fit to the measured dark current at the voltages above 22.0 V, confirming the presence of tunelling current in the InGaAs layer, as shown in figure 7.2.1(b).

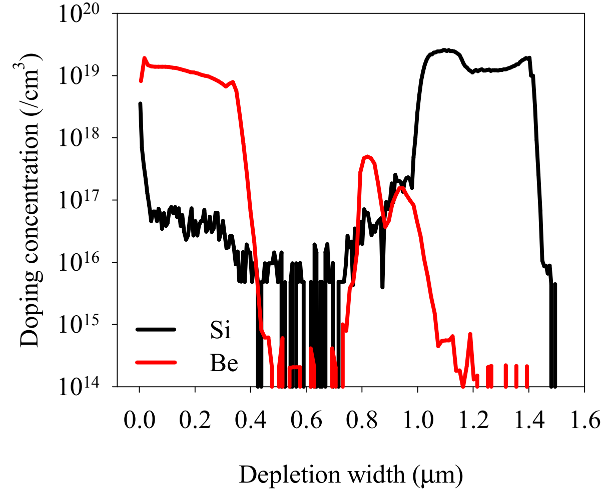

Figure 7.3.2 SIMS results of the InGaAs/AlAsSb SAM APD.

At the punch-through voltage of 8.2 V, our model suggests that the electric fields in the InAlAs and AlAsSb i-regions are 442 and 516 kV/cm respectively. The onset of avalanche gain in an InAlAs pin diode with an avalanche region of 100 nm has been measured at a field of ~ 363 kV/cm (M = 1.01) [10, 15] while our recent work on AlAsSb pin diode with an avalanche region of 80 nm suggested that avalanche gain is measurable when the field exceeds 489 kV/cm (M = 1.01) [16]. It is therefore not surprising that M ~1.06 was measured at ~ 8.2 V in our SAM-APD as small gains can be expected from both InAlAs and AlAsSb i-regions. Using a 1.52 µm laser we have also performed shot noise measurements of our SAM-APD biased at 8.2 V and compared the measured noise to that of a commercial Si pin diode. At a given photocurrent the ratio of the shot noise of our SAM-APD to that of a Si pin diode yields M~1.05 consistent with the value derived from the responsivity data.

The simulated electric field profiles in figure 7.2.3 also showed that the field in the InGaAs absorption layer exceeds 200 kV/cm at 22.0 V and is consistent with the onset of

significant tunelling current observed in figure 7.2.1(b). Increasing the charge density in both the InAlAs and AlAsSb field control layers will be necessary to suppress the tunelling current. Two field control layers were adopted in our design since the field required to achieve high gain in thin AlAsSb is > 1 MV/cm while field < 200 kV/cm in the InGaAs absorption layer is essential to control the tunelling current. Since significant tunelling current will be observed in InAlAs if the field exceeds 650 kV/cm [15] adopting a single thick InAlAs charge layer is not practical. A single thick charge layer will also compromise our attempt to confine the avalanche process in a very thin avalanche region. Moreover the InAlAs layers also act as bandgap grading layers to minimise carrier trapping at the heterojunctions. At the punch through and higher voltages, the fields in the charge layers exceed 442 kV/cm and the electrons are likely to occupy the X and L valleys. Although the band alignments between AlAsSb and InAlAs at these valleys are unknown, carrier trapping appears to be insignificant since we obtained high responsivity value at the punch through voltage.

The measured excess noise is slightly lower than those measured in an InAlAs pin diode with a 100 nm avalanche region. This is encouragingly low despite the low Be doping in the AlAsSb charge sheet that leads to higher than intended electric fields in the InAlAs and InGaAs layers, leading to impact ionisation in these layers. The wider effective avalanche region will therefore increase the excess noise. At the maximum bias, of 26.5 V we estimated the electric field in the InGaAs to be 270 kV/cm. Using ionisation parameters from [17] the pure electron and pure hole initiated gains, at 270 kV/cm in the InGaAs absorption layer, are 1.22 and 1.04 respectively. Since these are low we believe that the excess noise is dominated by ionisation in the InAlAs and AlAsSb layers. We also believe the low measured excess noise can be attributed to the dead space effects in the 50 nm InAlAs and 40 nm AlAsSb i-regions. Further reduction in the excess noise should be possible by increasing the Be doping concentration in the AlAsSb charge sheet to confine the avalanche multiplication in the AlAsSb i-region only. This should enhance the dead space effects leading to further reduction in excess noise.

For gain-bandwidth measurements low device capacitance and resistance are essential.

The capacitance per unit area of our structure is 1.57×10^{-4} pF/μm^2. For a typical high speed diode with a diameter of 25 μm a low capacitance value of 0.08 pF can be expected. However the current contact resistivity is high. A value of 4.83×10^{-4} Ω.cm^2 was extracted from the transmission line model. The contact resistivity in the typical high speed diode is ~ 10^{-6} Ω.cm^2 with the high doping level of 10^{-19} /cm^3 in the cladding layer and with an optimised metallisation process. However the doping level in our structure is not high enough and no optimisation process has been performed. Hence optimisation of the contact resistivity as well as microwave bond pads for characterisation of the gain bandwidth product of our AlAsSb based APDs is a subject of future research. Evaluation of different metallisation schemes and annealing conditions to lower the contact resistivity will be necessary.

7.4 Conclusion

A SAM APD incorporating a 40 nm AlAsSb avalanche region and a 500 nm InGaAs absorption region has been grown and characterised. A reasonably low dark current density of 8×10^{-6} A/cm^2 was measured at the punch-through voltage of 8.2 V, which is quite competitive with the Ge diodes grown on Si. A high responsivity of 436 mA/W was measured at 8.2 V using a 1.55 μm laser. This suggests no significant carrier trapping at the heterojunctions and a non-unity gain at punch-through. A gain of M ~ 1.06 was deduced by comparing the measured and theoretical responsivities and corroborated by shot noise measurements on Si pin diodes.

The lower than intended doping concentration in the AlAsSb field control layer increases the fields in the InGaAs layer above 200 kV/cm leading to significant tunelling current as well as higher than intended field in the InAlAs layers. Consequently avalanche multiplication from both the InAlAs and AlAsSb i-layers contribute to the overall mean gain. Despite this excess noise lower than that from an InAlAs pin diode with a 100 nm avalanche region was measured. The measured excess noise yields an effective k ~ 0.1 to 0.15. Use of thinner avalanche region should improve the excess noise. Therefore we

believe AlAsSb avalanche regions with thicknesses below 100 nm are highly promising for low noise APD as well as providing high thermal stability due to their small temperature coefficients of breakdown.

7.5 Reference

[1] D W Palmer, www.semiconductors.co.uk, 2006.02.

[2] M. A. Littlejohn, K. W. Kim and H. Tian "High-field transport in InGaAs and related heterostructures," *Properties of lattice-matched and strained Indium Gallium Arsenide*, INSPEC, pp. 114, 1993.

[3] J. E. Bowers, and C. A. Burrrus, "Ultrawide-band long-wavelength p-i-n photodetectors', *IEEE, J. Lightwave Technol.*,vol. 5, pp. 1339-1350, 1987.

[4] K. S. Lau, C. H. Tan, B. K. Ng, K. F. Li, R. C. Tozer, J. P. R. David, and G. J. Rees, "Excess noise measurement in avalanche photodiodes using a transimpedance amplifier front-end," *Meas. Sci. Technol.*, vol.17, pp. 1941–1946, 2006.

[5] K. F. Li, D. S. Ong, J. P. R. David, G. J. Rees, R. C. Tozer, P. N. Robson, and R. Grey,"Avalanche multiplication noise characteristics in thin GaAs p+-i-n+ diodes", *IEEE Trans. Electron Dev.,* vol. 45, no. 10, pp. 2102-2107, 1998.

[6] S. A. Alterovitz "Dielectric functions and refractive index of $In_xGa_{1-x}As$," *Properties of lattice-matched and strained Indium Gallium Arsenide*, INSPEC, pp. 188, 1993

[7] S. Adachi, Physical Properties of III-Y Semiconductor compounds. *John Wiley and Sons*.1992.

[8] R. J. McIntyre, "Multiplication noise in uniform avalanche diodes," *IEEE Trans on Electron Dev.*, vol. 3, pp. 164-168, 1966.

[9] S. R. Forrest, R. F. Leheny, R. E. Nahory, and M. A. Pollack, "$In_{0.47}Ga_{0.53}As$ photodiodes with dark current limited by generation- recombination and tunelling," *Appl. Phys. Let.*, vol. 37, no. 3, pp.322–325, 1980.

[10] Y. L. Goh, D. J. Massey, A. R. J. Marshall, J. S. Ng, C. H. Tan, W. K. Ng, G. J. Rees, M. Hopkinson and J. P. R. David, "Excess noise in $In_{0.52}Al_{0.48}As$", *IEEE J. of Quantum Electron.*, vol.43, pp.503-507, 2007.

[11] Y. M. Kang, H. D. Liu, M. Morse, M. J. Paniccia, M. Zadka, S. Litski, G. Sarid, A. Pauchard, Y. H. Kuo, H. W. Chen, W. S. Zaoui, J. E. Bowers, A. Beling, D. C. McIntosh, X. G. Zheng, and J. C. Campbell, "Monolithic germanium/silicon avalanche photodiodes with 340 GHz gain-bandwidth product," Nature Photonics, vol. 3, pp. 59-63, 2009.

[12] Malcolm S. Carroll, Darwin K. Serkland, Kent Childs, Robert Koudelka *et al.* Final Report on LDRD project: Single-Photon-Sensitive Imaging Detector Array at 1600nm (SAND2006-7420).

[13] M. Jutzi, M. Berroth, G. Wöhl, M. Oehme, and E. Kasper, "Ge-on-Si vertical incidence photodiodes with 39-GHz bandwidth," IEEE Photon. Technol. Lett., vol. 17, no. 7, pp. 1510–1512, Jul. 2005.

[14] Datasheet from thorlabs Ge commercial diodes (FDG03, 05, 1010).

[15] Y. L. Goh, D. J. Massey, A. R. J. Marshall, J. S. Ng, C. H. Tan, W. K. Ng, G. J. Rees, M. Hopkinson, J. P. R. David, and S. K. Jones, "Avalanche multiplication in InAlAs", *IEEE Trans. Electron Devices* vol. 54, no. 1, pp. 11-16, Jan. 2007.

[16] S. Xie and C. H Tan, "AlAsSb avalanche photodiodes with a sub-mV/K temperature coefficient of breakdown voltage", *IEEE J. of Quantum Electron.,* vol. 47, no. 11, pp. 1391-1395, Nov. 2011.

[17] J. S. Ng, C. H. Tan, J. P. R. David, G. Hill and G. J. Rees, "Field dependence of $In_{0.53}Ga_{0.47}As$ impact ionisation coefficients", *IEEE Trans. Electron Devices*, vol.50, pp.901-905, 2003.

[18] L. J. J. Tan, Y. L. Goh, S. C. Liew-Tat-Mun, D. S. G. Ong, J. S. Ng and J. P. R. David, "Temperature dependence of breakdown in InP and InAlAs", *IEEE Trans. Electron Devices,* vol. 46, no. 8, pp. 1153 – 1157, Aug. 2010.

Chapter 8 Conclusion

8.1 Conclusion

This work provides a systematic investigation of design, fabrication optimisation process, and characterisation of high speed InGaAs photodiode, InGaAs/InAlAs SAM APD and novel AlAsSb-based APDs for potential applications in the next generation optical communication system.

The conventional vertically illuminated and side illuminated waveguide InGaAs p-i-n photodiodes with an intrinsic layer thickness of 300 nm have been characterised. The vertically illuminated devices show a reduction of bandwidth with increasing the device area and the values are consistent with the calculated RC limited bandwidth. The bandwidths of waveguide devices with different waveguide lengths are lower than predicted RC limited values and are probably limited by the un-optimised bond pads on the semi-insulating substrate. The maximum -3 dB bandwidths of 23.5 and 26.5 GHz were measured for vertically illuminated diodes with mesa diameter of 10 μm and waveguide diodes with length of 15 μm, respectively. The external quantum efficiencies of 30.4 and 38.4% were also measured for the vertical illuminated and waveguide devices. Higher bandwidth and external quantum efficiency corresponding to a higher bandwidth-efficiency product was demonstrated in the waveguide devices compared to the vertically illuminated devices.

Characterisation of two high speed InGaAs/InAlAs APDs adopting travelling wave designs has been performed. Both set of devices show a low dark current below 50 nA at $0.9V_{bd}$. Responsivity value of ~ 0.35 A/W for M3608 (with an InGaAs absorption layer of 600 nm) at -17.6 V and ~ 1.1 A/W for M3587 (with an InGaAs absorption layer of 1200 nm) at -17 V were measured. Consequently the avalanche gain was deduced to be 1.06 and 2.04 at their respective punchthrough voltages. The corresponding excess noise factors were found to be close to curves with a k value of 0.25 and 0.2, consistent with the InAlAs p-i-n diodes with the same avalanche region thickness. Wide bandwidths at low gains up to 40 GHz were shown for both APDs with different waveguide lengths and the

values are higher than the calculated RC limited bandwidth, suggesting insignificant RC effects due to the travelling-wave design. No signal saturation effect has been observed with the RF power ranging from -27 to 0 dBm. The capability of achieving higher signal amplification at 35 GHz, together with lower dark current in both APDs, than the best InGaAs/InAlAs APD at 40 Gb/s reported by Makita *et al*. [1] was also demonstrated. Hence their suitability for use in 40 Gb/s communication systems have been shown.

The temperature dependence of the novel AlAsSb p-i-n APDs with w = 80 nm and 230 nm has also been investigated. Currently devices show surface dominated leakage current, which reduces with temperature. No measurable band to band tunelling current was observed in the thinner diodes at electric fields up to 1.07 MV/cm. Temperature coefficients of breakdown voltage of 0.95 and 1.48 mV/K were obtained from the diodes with w = 80 and 230 nm respectively, which are significantly lower than a range of semiconductor materials with similar avalanche region widths. The novel InGaAs/AlAsSb SAM APDs incorporating a 500 nm InGaAs absorption layer, and a 40 nm AlAsSb multiplication layer was first grown and characterised. A reasonably low dark current density of 8×10^{-6} A/cm^2 and a high responsivity of 436 mA/W using a 1.55 μm laser were measured at the punchthrough voltage, which is quite competitive compared to the currently reported Ge related diodes. Low excess noise factor corresponding to k of 0.1 ~ 0.15 was measured and it is lower than that from an InAlAs pin diode with a 100 nm avalanche region.

8.2 Suggestions for future work

The un-optimised bond pads and the thin absorption layer with 300 nm thickness currently limit the bandwidth and quantum efficiency in the InGaAs p-i-n diodes. Redesigning the bond pads utilizing the air-bridge techniques and growing a buffer layer upon the semi-insulating substrate in the structure may minimise the microwave loss and leakage current from the substrate. Integrating an optical matching layer which is designed to match the optical field envelope of the fiber underneath the InGaAs p-i-n diodes [2] to increase the light absorption area may improve the efficiency in the diode.

Low dark current, low excess noises, wide bandwidth and high GBP have been demonstrated on our InGaAs/InAlAs APDs. However the performance of a receiver module containing an APD with a per-amplifier has not been assessed via sensitivity measurements. Integrating the APD with pre-amplifiers, either through on wafer in-plane integration or by wire bonding two devices together could be a subject of future work. In addition of detecting the weak optical signal, the combination of APD and the pre-amplifier can be used to amplify the converted electrical signal into hundreds of mill volts for digital circuit with low fed in noise. There would be a very high excess noise generated in APD if it provides hundreds of gains alone for the following circuit signal requirement. Temperature dependence of excess noise and bandwidth can be performed to determine the ionisation coefficient ratio in InAlAs, which depends critically on the scattering environments [4].

The extremely low C_{bd} has been demonstrated in AlAsSb p-i-n diodes and InGaAs/AlAsSb SAM APDs. However the measured dark currents in all structures are predominantly surface leakage current at room temperature. Therefore surface passivation and optimised etching procedures are required. The origin of the small C_{bd} in AlAsSb also needs to be fully understood. Modelling incorporating appropriate temperature dependence of ionisation rate, phonon and alloy scattering rates will be necessary to quantify the small C_{bd} observed in our thin AlAsSb diodes.

Despite low excess noise factor yielding k factor of 0.1 ~ 0.15 was measured in the InGaAs/AlAsSb SAM APDs. The noise is thought to be contributed by both InAlAs charge sheet and multiplication layer because the low Be doping in the AlAsSb charge sheet that leads to higher intended electric field in the InAlAs and InGaAs layer and wider effected avalanche region width. Therefore optimisation of growth conditions to increase Be doping concentration in the AlAsSb charge sheet to confine the avalanche multiplication in the AlAsSb multiplication layer can further reduce its excess noise and increase the speed.

8.3 Reference

[1] K. Makita, T. Nakata, K. Shiba and T. Kakeuchi, “40Gbps waveguide photodiodes”, J. of *Adv. Tech.*, Summer, 2005.

[2] A. Beling, H. G. Bach, G. G. Mekonnen, R. Kunkel and D. Schmidt, “Miniaturized waveguide-integrated p-i-n photodetector with 120-GHz bandwidth and high responsivity,” *IEEE Photon. Technol. Lett.*, vol. 17, pp. 2152–2154, 2005.

[3] X. Zheng, "Long wavelength high speed Photodiodes and APD Arrays," in *EEE. Doctor of Philosophy*: The University of Texas at Austin, 2004.

[4] L. J. J. Tan, "Telecommunication wavelength InP based avalanche photodidoe," in *EEE. Doctor of Philosophy*: The University of Sheffield, 2008

Appendix A Analytical calculations of circuit elements in CPW

This appendix describes the analytical calculations for the transmission line circuit elements of coplanar waveguide (CPW), which includes the capacitance, C, the inductance, L_i, the dielectric constant, ε_r, the microwave effective dielectric constant, ε_{r_eff}, and the characteristic impedance, Z_0. The cross section of a CPW structure on dielectric substrate is shown in figure A.1.

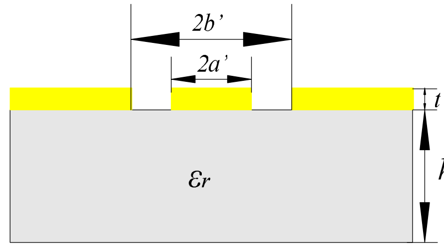

Figure A.1 Schematic of a CPW without bottom ground metal.

The circuit elements in a CPW without bottom ground plan are [1, 2],

$$\varepsilon_{r_eff} = 1 + \frac{\varepsilon_r - 1}{2} \frac{K(k_0^{'})K(k_1)}{K(k_0)K(k_1^{'})}$$

$$Z_L = \frac{30\pi}{\sqrt{\varepsilon_{r_eff}}} \frac{K(k^{'})}{K(k_w)}$$

$$C = \frac{\sqrt{\mu_0 \varepsilon_0 \varepsilon_{r_eff}}}{Z_L}$$

$$L_i = Z_L \sqrt{\mu_0 \varepsilon_0 \varepsilon_{r_eff}}$$

where ε_0 and μ_0 are the permittivity and permeability in vacuum and

$$k_0 = a^{'} / b^{'}$$

$$k_0^{'} = \sqrt{1 - k_0^{2}}$$

$$k_1 = \sinh(\pi a^{'} / 2h) / \sinh(\pi b^{'} / 2h)$$

$$k_1^{'} = \sqrt{1 - k_1^{2}}$$

$$K(k_0) = (\pi / 2) \cdot \{1 + 2(k_0^{2} / 8) + 9(k_0^{2} / 8)^2 + 50(k_0^{2} / 8)^3 + 306.25(k_0^{2} / 8)^4 + ...\}$$

for $0 \le k_0 \le 0.71$

$$K(k_0) = p + (p-1)(k_0'^2/4) + 9(p-7/6)(k_0'^4/64) + 25(p-37/30)(k_0'^4/256) + \ldots$$

$$p = \ln(4/k_0') = \ln(4/\sqrt{1-k_0^2})$$

for $0.71 \le k_0 \le 1$

[1] G. Ghione and C. Naldi, “Analytical formulas for coplanar lines in hybrid and monolithic MICs,” *Electron. Lett.,* vol. 20, pp. 179-181, 1984.

[2] R. K. Hoffmann, Handbook of Microwave Integrated Circuits. Boston: Artech House, Inc., pp. 355-356, 1987.

Appendix B Calculation of electric field profile

The electric field of diodes can be obtained by solving the Poisson equation and preserving the charge equilibrium in this appendix. This is different from the model described by Tan [1] which considers the continuous electric field profile in the depletion region. A homojunction $p^+p^-n^+$ diode is considered below and shown in figure B.1. The doping in the p^+, p^- and n^+ region are respectively N'_1, N'_2 and $-N'_3$ (negative sign denotes n-type doping) and X_1, X_2 and X_3 are the corresponding thickness of each region.

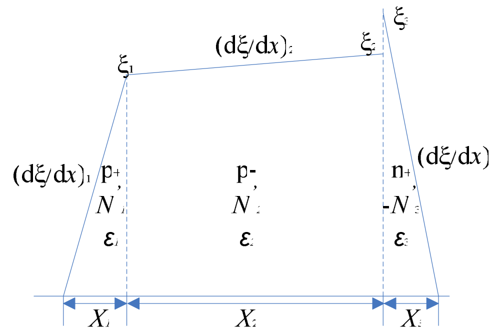

Figure B.1 Electric filed profile in the $p^+p^-n^+$ diode

From Possion's equation:

$$(\frac{d\xi}{dx})_1 = \frac{qN'_1}{\varepsilon_1}, \qquad (\frac{d\xi}{dx})_2 = \frac{qN'_2}{\varepsilon_2} \quad \text{and} \quad (\frac{d\xi}{dx})_3 = -\frac{qN'_3}{\varepsilon_3} \tag{B.1}$$

where ε is the permittivity of the material. The field junction can be written as:

$$\xi_1 = \frac{qN'_1 X_1}{\varepsilon_1}, \qquad \xi_2 = \xi_1 + \frac{qN'_2 X_2}{\varepsilon_2} \quad \text{and} \quad \xi_3 = -\frac{qN'_3 X_3}{\varepsilon_3} \tag{B.2}$$

To maintain charger neutrality in p^+p^- and n^+ region:

$$N'_1 X_1 + N'_2 X_2 = N'_3 X_3 \tag{B.3}$$

The area under the electric field is equal to the total voltage V_t. Therefore it can be written:

$$V_t = \frac{1}{2}(\xi_x X_1 + (\xi_1 + \xi_x) X_x + \xi_3 X_3) \tag{B.4}$$

Substituting equation (B.2), (B.3) and (B.4) gives

$$\frac{N'_1}{\varepsilon_1}(1-\frac{\varepsilon_1 N'_1}{\varepsilon_3 N'_3})x_1^2+\frac{2N'_1}{\varepsilon_1}(x_2-\frac{\varepsilon_1 N'_2}{\varepsilon_3 N'_3})x_1-\frac{N'_2 x_x^2}{\varepsilon_3 N'_3}+\frac{N'_x x_2^2}{\varepsilon_2}-\frac{2V_t}{q}=0$$

(B.5)

Therefore from eqnuation (B.5), X_1 can be solved

$$X_1=\frac{-b+\sqrt{b^2-4ac}}{2a}, \tag{B.6}$$

where $a_1=\frac{N_1}{\varepsilon_1}(1-\frac{\varepsilon_1 N'_1}{\varepsilon_3 N'_3})$

$$b_1=\frac{2N'_1}{\varepsilon_1}(x_2-\frac{N'_2\varepsilon_1}{\varepsilon_3 N'_3}x_2)$$

$$c_1=-\frac{N'_2 x_2^2}{\varepsilon_3 N'_3}+\frac{N'_2 x_x^2}{\varepsilon_2}-\frac{2V_t}{q} \tag{B.7}$$

Extending the analysis to a 4 region structure such as in a Separate-Absorption-Multiplication APD gives:

$$a_1=\frac{N'_1}{\varepsilon_1}(1-\frac{\varepsilon_1 N'_1}{\varepsilon_4 N'_4})$$

$$b_1=\frac{2N'_1}{\varepsilon_1}((x_2+x_3)-\frac{\varepsilon_1}{\varepsilon_4 N'_4}(N'_2 x_2+N'_3 x_3))$$

$$c_1=-\frac{(N'_x x_x+N'_3 x_3)^2}{N'_4\varepsilon_4}+\frac{qN'_2}{\varepsilon_2}x_x^2+\frac{qN'_3}{\varepsilon_3}x_3^2+\frac{2qN'_2}{\varepsilon_2}x_2x_3-\frac{2V_t}{q} \tag{B.8}$$

For a 5 region structure such as in a Separate-Absorption-Charge Sheet-Multiplication APD we have:

$$a_1=\frac{N'_1}{\varepsilon_1}(1-\frac{\varepsilon_1 N'_1}{\varepsilon_5 N'_5})$$

$$b_1=\frac{2N'_1}{\varepsilon_1}((x_2+x_3+x_4)-\frac{\varepsilon_1}{\varepsilon_5 N'_5}(N'_2 x_2+N'_3 x_3+N'_4 x_4)$$

$$c_1 = -\frac{(N'_x x_x + N'_3 x_3 + N'_4 x_4)^2}{N'_5 \varepsilon_5} + \frac{N'_2}{\varepsilon_2} x_x^2 + \frac{N'_3}{\varepsilon_3} x_3^2 + \frac{N'_4}{\varepsilon_4} x_4^2 + \frac{2N'_2}{\varepsilon_2} x_2 x_3 + \frac{2N'_3}{\varepsilon_3} x_3 x_4 - \frac{2V_t}{q}$$ (B.9)

Therefore the electric filed profile of a multi-layer structure can be calculated by inspection of eqns. (B.7, 8, 9), the expression for a_1, b_1 and c_1 for a structure with m regions is:

$$a_1 = \frac{N'_1}{\varepsilon_1}\left(1 - \frac{\varepsilon_1 N'_1}{\varepsilon_m N'_m}\right)$$

$$b_1 = \frac{2N'_1}{\varepsilon_1}\left(\sum_{k=2}^{m-1}\left(x_k - \frac{\varepsilon_1 N'_k x_k}{\varepsilon_m N'_m}\right)\right)$$

$$c_1 = -\frac{\sum_{k=2}^{m-1}(N'_k x_k)^2}{N'_m \varepsilon_m} + \sum_{k=2}^{m-1}\left(\frac{N'_k x_k^2}{\varepsilon_k}\right) + \sum_{k=2}^{m-2}\frac{2N'_k x_k}{\varepsilon_k}\sum_{k=l+1}^{m-1} x_l - 2\frac{V_t}{q} \qquad \text{(B.10)}$$

So that the depletion in the first region, X_1, and the mth region, X_m, can be expressed as:

$$X_1 = \frac{-b + \sqrt{b^2 - 4ac}}{2a}$$

$$X_m = -\frac{\sum_{k=1}^{m-1} N'_k X_k}{N'_m} \qquad \text{(B.11)}$$

All layers, except the first and the mth layer, in a structure with m regions are fully depleted and the total depletion width, d, is

$$d = X_1 + \sum_{k=2}^{m-1} X_k + X_m \qquad \text{(B.12)}$$

[1] C. H. Tan, "Measurements of excess avalanche noise in sub-micron Si and $Al_{0.8}Ga_{0.2}As$ avalanche photodiodes," in *EEE. Doctor of Philosophy*: The University of Sheffield, 2002.

Appendix C Operation instructions for high speed measurement setup

The frequency response measurement using the network analyzer (VNA) together with the 40 GHz optical EAM @ 1.3 µm and heterodyne setup @ 1.55 µm were described as follows:

1. VNA and EAM @ 1.3 µm operation:

(a) Calibrate the whole system: (if there is a good already known reference diode)

(1) Connect the systems as shown in figure C.1 and turn on the power supply of each equipment;

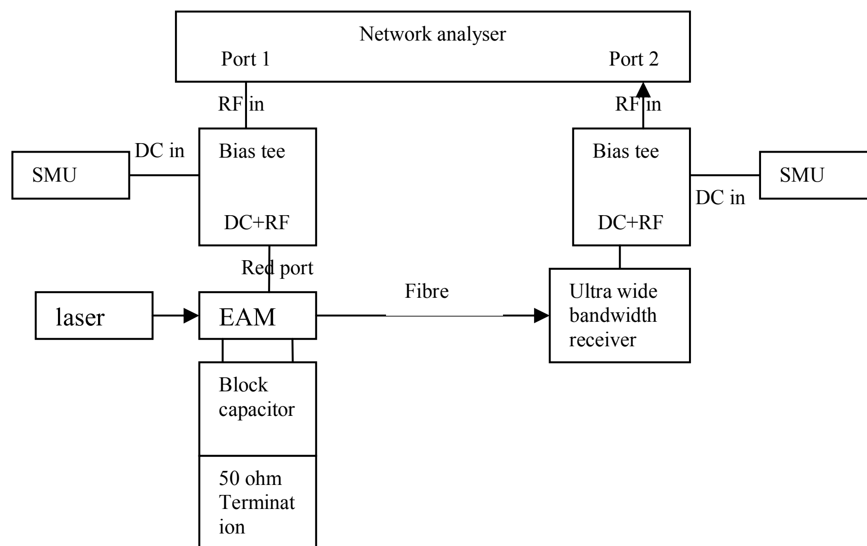

Figure C.1 Calibration process using the VNA and EAM.

(2) Reverse bias the modulator at -1 V;
(3) Set the RF power at the network analyzer with + 10 dBm;
(4) Open the laser diode;
(5) Set the average factor at the network analyzer;
(6) Set the calibration frequency range (10 MHz ~ 50GHz)
(7) Press the “Calibration wizard” at the network analyzer;
(8) If during the measurements, any setting has been changed (such as the RF power or average factor), repeating the calibration processing.

(b) Frequency response/Power sweep measurement:

(1) Connect the systems as follows: (The EAM operation instruction sheet shown besides with note "Switch on".

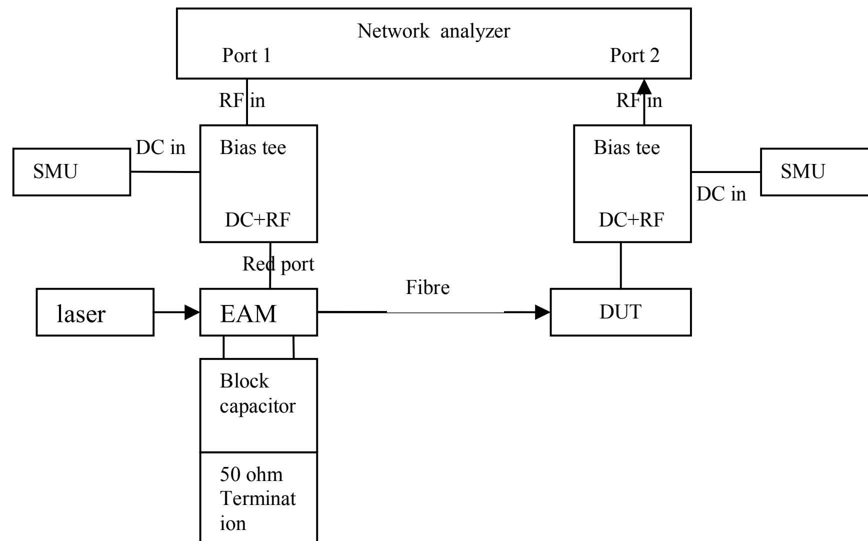

Figure C.2 Frequency response measurement using VNA and EAM

(2) Reverse bias the modulator at -1 V;
(3) Set the RF power at the network analyzer with 0 dbm;
(4) Open the laser diode;
(5) Set the frequency range (10 MHz ~ 40 GHz)
(6) Set the average factor at the network analyzer;
(7) Set the IF bandwidth to be 100 kHz to lower the noise floor
(8) For frequency response measurement, select the "sweep type" as "frequency response" and select "Power sweep" as the power sweep measurement.
(9) Set the "receiver B" from "Port 2"to directly perform the frequency response from the integrated receiver in the VNA.
(10) If the detector has a strong response, the optional frequency response measurement can be carried out using "S21" measurement.
(11) Save the results in the format of ".trace".

(c) Shut down the setup:

(1) Followed the EAM operation instruction sheet shown besides with note "Switch Off".
(2) Turn off the net work analyzer and SMU.
(3) Turn off the mains power.

(d) EAM operation limit:

(1) 40GHz modulator operation:
(2) Maximum forward DC voltage: + 0.6 V;
(3) Maximum reverse DC voltage: - 4 V;

(4) Maximum Input optical power: + 14 dBm;
(5) Maximum RF voltage (peak to peak): 3 V (V_{rms}: 1.06 V) --Maximum RF power: 13 dBm.
(6) Operation temperature: 15-50 °C

(e) Additional information of EAM

(1) HP 6GHz laser: output optical power @ 1.3um was193uW measured by Thorlabs power meter before the fibre was connected to the 40 GHz modulator (1.3 um).
(2) Connected the HP laser with the 40 GHz modulator and measured the output power from the modulator. (Here, the output laser light would be absorbed by the modulator, which was defined the operation voltage range).

Bias (V)	Output power from the modulator (μW)
+0.4	5.8
+0.2	4.985
0	3.8
-0.5	1.45
-1	0.55
-1.5	0.32
-2	0.25
-2.5	0.215
-3	0.214
-3.5	0.22
-4	0.25

(3) According to above results, the best DC voltage was operated at the reverse bias of -1V with the RF power (set from the network analyzer: 10 dBm (corresponding to Vrms: 0.71V)

2. Heterodyne setup operation:

(1) Connect the system as shown in figure C.3 and turn on the power supply of each equipment

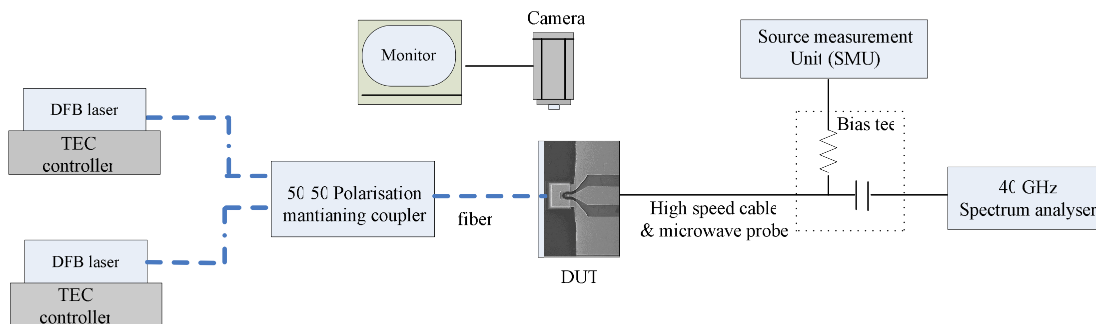

Figure C. 3 Frequency response measurement using heterodyne setup.

(2) Take 20 ~ 25 minis to warm up the thermist and spectrum analyser;
(3) Press the hard key of "shift + calibre" and select "Full calibration" to calibrate the whole system;

(4) Setting for the Melles Griot DTC301 temperature controller is as follows:

1) I_{limit}: Current flowing the Peltier Cool (@ 100 mA)
2) I_{LD}: Control current flow through the laser diode (I_{th} = 35 μA)
3) P_{LD}: Control output power from the laser diode
4) I_{PD}: Feedback loop to control power of the laser module and if the current ≥ 5 μA indicating the constant power output
5) Select the "constant P" as the constant power mode operation during the measurement.

Appendix D Fabrication Process

The travelling wave avalanche photodiode (TWAPD) wafer was processed by the following steps in detail.

1. Cleaving:
(a) Put wafer orientation marks on back side of the wafer.
(b) Backside cleave, and cotton bud press the topside, rotating the cleaver.
(c) Change the filter paper and N2 gun bowl the wafer.

2. Cleanning: (avoid superheating)
(a) boil in n-bytal 30 s
(b) boil in acetone 30 s
(c) boil in IPA
(d) Inspection the surface

3. Top contact metallisation (The pattern process needs to be known the crystal direction according to the back arrow indication)
(a) Dehydrate bake the sample around 1.5 min
(b) After removing the sample edge photoresist, TW-APD top contact mask: UV 400 light exposure 0.9 s and development: 60 s. Alignment needs to be maximum view and vertical side in the surface.
(c) Thermal evaporation Ti/Pt/Au (10/30/200 nm)
    1) Ti: 6 cm; Pt: 10 mg; Au: 2 coils--------Pay attention to the different height, get different temperature radiation to avoid heat up or damage the sample
    2) Ti and Pt always need to high temperature to evaporate, so that need to pay attention to the coil would not drop into the sample.
    3) Pt: 12 cm; Ti: 12 cm; Au: 6cm
(d) evaporation process:
    1) Weigh the metal
    2) First fit well the metal into the coils---Au two lengths
    3) Clean in the acetone
    4) Put the sample in the Al plate and above the monitor. The Al plate is used as a temperature conductor for the wafer because the evaporation temperature for Pt is quite high which can damage the photoresist during the evaporation process.
    5) Do the instructions:
        1. Turn on the both monitor power supply
        2. Make sure the switch box is on the correct evaporator selection
        3. Check “Au”, press “Data”, choose “Layer”
        4. press the “shutter” will be on, “0000” means something wrong
        5. after use, switch off
(e) Lift off in the acetone
(f) Inspection: under the microscope and use the curve trace to test the ohmic contact. If not ohmic, then rapid thermal annealing (RTA) the sample to improve the contact resistance.

(g) RTA (optional): annealing temperature (420 °C, 30 s)

4. Waveguide mesa etch
(a) 3-steps cleaning (n-butyl acetate, acetone and warm in IPA)
(b) Dehydrate bake the sample around 1.5 min
(c) After removing edge photoresist, TW-APD mesa mask: BPRS100, exposure: 0.9 s and development: 1 min
(d) Dectack measure the thickness of the photoresist and record the thickness
(d) Use H_2SO_4: H_2O_2: DIW (with the ratio of 1:8:80) etch to the InGaAs layer (etch rate: 0.5 μm/min)
   1) M3698: 1.51-1.81 μm
   2) M3699: 1.91-2.21 μm
   3) M3697: 2.02-2.32 μm
(e) Inspection under microscope and clean the photoresist in the acetone

5. Second isolation mesa etch-------etch to the semi-insulating substrate
(a) 3-steps cleaning (n-butyl acetate, acetone and warm in IPA)
(b) Dehydrate bake the sample around 1.5 min
(c) (After removing the sample edge photoresist, TW-APD second mesa mask: BPRS200, exposure time: 2 s and development: 1 min.
(d) Dectack measure the thickness of the photoresist and record the thickness
(e) H_2SO_4: H_2O_2: DIW (with ratio of 1:8:80) finish etching the bottom n^+ InGaAs layer and H_3P0_4: HCL: DIW (with ratio of 3:1:2) which etched the InP semi-insulating substrate for 10 s with the thickness of 0.5 μm.
(f) Inspection under microscope and clean the photoresist in the acetone

6. Ground contact
(a) 3-step cleaning (n-butyl acetate, acetone and warm in IPA)
(b) Dehydrate bake the sample around 1.5 min
(c) After removing the sample edge photoresist, TW-APD lower contact mask: BPRS 100, exposure time: 0.9 s and development: 1 min.
(d) Thermal evaporation: In/Ge/Au (10/20/200nm) (procedure the same as top contact)
(e) Lift off in the acetone
(f) RTA (optional): annealing metal temperature (360 °C, 3 s)
(g) Surface and resistance inspection

7. SiN_x dielectric layer passivation
(a) 3-step cleaning (n-bytal, acetone, warm IPA---after RTA)
(b) PECVD coating SiN_x (SiNx +NH3->SiNx+H2), thickness: 200 nm, deposition rate: 10~11nm/min at 293.3 °C.

8. Contact window open by reactive ion etching (RIE)
(a) 3-step cleaning (n-butyl acetate, acetone and warm in IPA)
(b) Dehydrate bake the sample around 1.5 min

(c) Use photoresist promoter hexamethydisilazane and spin 30 s @ 4000 rpm (improve the photoresist adhesion to deposited SiN_x)
(d) TW-APD contact window open mask: BPRS 200, exposure time: 2.2 s and development: 1 min. The increased exposure time was because the deposited SiN_x layer acted as an anti-reflecting coating layer. The photoresist at sample edge needs to be pre-removed.
(e) RIE process needs to get the vacuum environment
   1) Recipe: CHF_3 (35sccm) + O_2 (5sccm); Pressure: (35mTorr); RF Power (Forward power (FWDP): 70W, Reflective power (REFP): 0W; etch time: 7 minis
(f) Dectack measure the thickness of the photoresist and record the thickness
(g) Inspection under microscope and clean the photoresist in the acetone

9. CPW bond pads metallization
(a) 3-step cleaning (n-butyl acetate, acetone and warm in IPA)
(b) Dehydrate bake the sample around 1.5 min
(c) After removing the sample edge photoresist, TW-APD BP contact mask: BPRS 100, exposure time: 1.1 s and development: 1 min ((b) Exposure, developing time are tried the time above
(d) Thermal evaporation Ti/Au (10/500 nm)
(e) Lift off in the acetone
(f) Inspection under microscope.

10. Substrate thinning (by mechanical polishing using Minimet)
(a) Mount the sample onto the lapping chuck by wax on the hot plate (@100 °C)
(b) Put the lapper medium, start with 6 μm sand for roughness lapping surface, followed with 1 μm sand for better lapping surface and finally finished with ¼ μm sand for the best lapping surface. Put the lubricate liquid during lapping process
(c) Thinning the sample into ~ 150 μm

11. Waveguide scribe
(a) Carefully clean the thinned sample by 3-step cleaning (n-butyl acetate, acetone and warm in IPA)
(b) Follow the scribe machine instruction sheet in Sheffield III-V National Center
(c) For InP/InGaAs, set tool holder pressure : ~ 0.5 KPa, break pressure: 30 KPa

(d) Carefully clean the cleaved sample by 3-step cleaning (n-butyl acetate, acetone and warm in IPA)